ABSTRACT

Title of Dissertation:	IMAGING PYROMETRY OF SMOLDERING WOOD EMBERS
	Dennis Kgangyon Kim, Doctor of Philosophy, 2019
Dissertation directed by:	Professor, Peter B. Sunderland Department of Fire Protection Engineering

The wild fire problem in U.S. and across the world has caused the losses of human lives and property. Firebrands can dramatically increase the hazards of wildland fires. While embers have been extensively studied (e.g. firebrand generation, transport, ignition, size, mass, and moisture contents etc.), little is known about their temperatures. Also, all past works failed to measure firebrand temperature relying on thermocouple and IR camera, which are not accurate and have many drawbacks. Therefore, in this dissertation, to address this an imaging stationary ember and airborne firebrand pyrometer was developed using an inexpensive digital color camera. The camera response was calibrated with a blackbody furnace at 600 – 1200 °C. The embers were 6.4 mm maple rods with lengths of 2 cm. Temperatures were obtained from ratios of green/red pixel values and from grayscale pixel values. Ratio pyrometry is more accurate when ember emissivity times ash transmittance is not unity, but grayscale pyrometry has signal-to-noise ratios 18 times as high. Thus, a hybrid pyrometer was

developed that has the advantages of both, providing a spatial resolution of 17 μm, a signal-to-noise ratio of 530, and an estimated uncertainty of ±20 °C. The measured ember temperatures were between 750 – 1070 °C with a mean of 930 °C. Comparing the ratio and grayscale temperatures indicates the mean visible emissivity times transmittance was 0.73. Temperatures were also measured with fine bare-wire thermocouples, which were found to quench smolder reactions, make imperfect thermal contact, and underpredict the mean ember temperature by more than 200 °C. The pyrometry was also performed on a pendulum firebrand with different velocities imitating airborne firebrands in real fire scenario. The temperature increases as the velocity of pendulum firebrands increases. Ratio pyrometry determined mean temperatures of pendulum firebrand between 878 – 1064 °C. Grayscale pyrometry temperatures were lower. The relationship between velocities and temperatures were quantified. The pyrometry was additionally performed on smoldering fuels such as a rolled paper, incense, maple rod, ashless filter paper, and rattan sticks with different air jet velocities to explore the smoldering extinction at high air velocity.

To summarize, the main achievement of my Ph. D researches was to develop a new diagnostic of ember and firebrand temperature and emissivity and was successfully completed. The results would be a stepping stone to nearby future exploration of wildfire. The hazards of various firebrand materials and moisture contents could be better assessed in different wind velocities. Computational fire models could be improved. The firebrand size could be simultaneously measured with the same device, both key firebrand attributes could be determined in near real time.

IMAGING PYROMETRY OF SMOLDERING WOOD EMBERS

by

Dennis Kgangyon Kim

Dissertation submitted to the Faculty of the Graduate School of the
University of Maryland, College Park, in partial fulfillment
of the requirements for the degree of
Doctor of Philosophy

2019

Advisory Committee:
Professor Peter B. Sunderland (Fire Protection Engineering), Chair
Professor Christopher P. Cadou (Aerospace Engineering)
Associate Professor Michael J. Gollner (Fire Protection Engineering)
Associate Professor Stanislav I. Stoliarov (Fire Protection Engineering)
Professor Bao Yang (Mechanical Engineering)

Dedication

I would like to give special thanks to my lovely wife, Sunyoon, whom I met as I just started my Ph.D. She is only one that I've ever felt that I am indeed fortunate to meet and love during my life. I dedicate this dissertation to my beloved wife, who has always stood by me in joy or sorrow any time with unwavering support, trust, and encouragement over the years of my graduate school journey. I could never have finished my Ph.D. without her steadfast love even when we were in a long distance relationship. I promise to love you forever and ever.

I would like to thank with the deepest gratitude my mom and dad, who have been encouraging me to make my dream comes true with their eternal love on me. There is actually no need to explain further that I am always grateful to them just because they are my lovely parents. But, thanks to my mom's sacrifices, I was able to be educated in S. Korea and the United States and each environment has been a learning experience that has broadened me as person and an academic. Growing up motivated by my father, my mentor, I have held a curiosity of science and engineering with a love of learning. Thank you for your love and constant support in all I do, my mom and dad. I am so proud that I am your son.

I would like to offer many thanks to my younger sister (Heeyon), niece, brother in law, mother-in-law, father-in-law, my departed grandmother and grandfather (I know you all are watching over me and this honorable moment from the heaven), cousin and relatives, my friends in S. Korea and the United States. I am so glad that I can deliver my gratitude in this chance for all your encouragements along this journey.

I extend my thanks to professors, Dr. Hyung-Min Choi, Dr. Young-Je Kwark, Dr. Cheol-Jae Hong, Dr. Hyun-Joo Shim, and others at Organic Materials and Fiber Engineering in Soongsil University in S. Korea, who not only motivated me to learn organic chemistry, polymer, textile, physics chemistry, and engineering fields when I was in undergraduate school, but also did not hesitate to encourage me to study in the United States with their strongest support.

Lastly, thank you so much, God, who has given me love, trust, and hope in my voyage, allowed me this glorious accomplishment, and made me do everything possible through him. I wish that my journey is not just the process of receiving my Ph.D. degree but it is a stepping stone to being a good person and contributing my knowledge and experience to society in the future.

Acknowledgements

I would like to deliver the deepest eternal appreciation to my advisor, Dr. Peter B. Sunderland, who supported me throughout studies at Fire Protection Engineering at UMD. Thanks to him, I was able to have incredible research opportunities, allowing me chances to interact with researchers, become a scientist, and perform the research successfully during Ph.D. I was able to humbly learn things from his incredible and outstanding insight, ideas, passion, teaching, and kind consideration for students. Thank you so much, Dr. Sunderland. It was great pleasure and honor to have worked with you under your direction in the past three years.

I thank profusely all who supported this research project. This work was supported by National Institute of Standards and Technology (NIST) grant 70NANB17H212 with Nicolas Bouvet as technical contact. Eric Auth assisted with the image analysis. He was always there to help me with this research and proofreading of my writing.

I would like to humbly thank to all my committee members, Dr. Stanislav I. Stoliarov, Dr. Michael Gollner, Dr. Bao Yang, and Dr. Christopher Cadou for acceptance to serve pleasantly on my Ph.D. dissertation, and additionally, Dr. Jose Torero, and Dr. Michael Zacharia, who left the campus but served on my Ph.D. proposal. They all offered me precious feedback and comments regarding my research. Special thanks to Dr. Gollner, who encouraged me to keep doing research and provided us Wildfire Urban Interface (WUI) studies. Also, special thanks to Dr. Stoliarov and Dr. Marshall Andre, whom I served as a TA student for Fire Dynamics and Fire Assessment Methods and Laboratory classes, respectively, for their magnificent teaching, which broadened my fire fields knowledge and perspectives.

I would like to specially thank Dr. Sunderland's group members, Zhengyang Wang, Parham Dehghani, Hanju Lee, John Hoffman, Paul Anderson, and Akshit Markan. Special thanks to Zhengyang for very useful discussion regarding fire researches as a good associate and friend. I was very pleasure to collaborate The American Society of Heating, Refrigerating and Air-Conditioning Engineers (ASHRAE) 1717RP and Air Conditioning, Heating, and Refrigeration Institute (AHRI) 8017 projects during my Ph.D. with previous students as well, Conor Mccoy, Alexandra Klieger, Jonathan Reymann, Peter Lomax, Angela Hermann, and Markus Kokot. It would be never possible to successfully complete projects as a great team without their support and all their invaluable suggestions under the direction of my advisor. Especially, Connor helped me adapt to new environments in the group when I came to UMD for the first time as a good friend. Also, he assisted me with designing diagrams in LabView with Fernando Raffan-Montoya, who helped me with setting up a DAQ system for pendulum experiments. I would like to deliver my deep gratitude to all my friends and group members.

I would like to sincerely thank, Fire protection engineering faculty, staff, and friends. Thank you, Dr. Arnaud Trouve, who was a committee chair for my qualifying exam, Dr. James Quintiere, Dr. James Milke, Christine O'Brien, Brian Sullivan, Nicole Hollywood, Mary Holt, Sharon Hodgson, all professors, staffs and all my friends in Fire Protection Engineering. I am so proud that I worked in such wonderful department, Fire Protection Engineering. Also, I would like to heartily thank the staff, especially James Kerri as a director of graduate studies, and faculties in Department of

Mechanical Engineering. I am grateful to be life time member of the University of Maryland.

Lastly, I thank all my friends in Korea association students, ASHRAE and AHRI, who supported my previous researches and grants during my Ph.D.

Table of Contents

List of Tables

List of Figures

List of Abbreviations

B	Blue
CCD	Charged-couple device
CMOS	Complementary metal-oxide semiconductor
C_1	First radiation constant, 3.742×10^{-16} W-m^2
C_2	Second radiation constant, 0.01439 m-K
DAQ	Data acquisition system
E_{GS}	Total emissivity power of blackbody
E_{ratio}	Total emissivity power of smoldering ember
etc	And so on
e.g.	For example
E_λ	Spectral emissive power of smoldering ember
$E_{\lambda b}$	Spectral emissive power of blackbody
Eq.	Equation
f	F-number
FOV	Field of View
G	Green
g	The standard acceleration due to gravity
I	Moment of inertia
I_B	Blue pixel values
I_{DC}	Dark-current pixel values
I_G	Green pixel values

I_{GS}	Grayscale pixel values
I_R	Red pixel values
ISO	International organization for standardization
K_1	Initial potential energy
K_2	Final potential energy
k_p	Ash mass extinction coefficient
L	Ash layer thickness
l	Length of the rod
$\log_{10}$	Logarithm (base 10)
m	Mass
mm	Milimeter
nm	Nanometer
NI	Normalized pixel values
NI_B	Normalized blue pixel values
NI_G	Normalized green pixel values
NI_{GS}	Normalized grayscale pixel values
NI_R	Normalized red pixel values
pdfs	Probability distribution function
R	Red
Ref	Reference
s	Second
SiC	Silicon carbide
SNR	Signal-to-noise-ratios

$S(\lambda)$	Camera sensitivity
t	Exposure time
T	Temperature
TC	Thermocouple
T_{GS}	Grayscale Temperature
T_{hybrid}	Hybrid Temperature
Tr	Transmissivity
T_{ratio}	Ratio Temperature
U_1	Initial rotational kinetic energy
U_2	Final rotational kinetic energy
v	Firebrand velocity
Y	Mass of ash per mass of wood burned
°C	Degree Celsius
ε	Emissivity
λ	Wavelength
μm	Micrometer
τ	Transmittance
ω	Angular velocity
ρ	Virgin wood density

Chapter 1: Introduction

1.1 Overview of the literature

Wildland fires are a problem with global impact. They are responsible for increasing losses of lives and property, and increasing costs of fire prevention and suppression [1–3]. Of particular concern are fires in the wildland-urban interface (WUI) [4].

Embers are small smoldering fuels, and firebrands are airborne embers. Firebrands can have a large impact on wildland fire spread [5–6] and they often complicate firefighting. Smoldering can be associated with long burn times, concealed luminous emissions, minimal smoke, and the potential for sudden eruption into flaming [7–8]. Firebrands can be lofted several km and still ignite spot fires. An improved understanding of firebrands is crucial to protecting against wildland fires, e.g., by contributing to improved fire codes and standards, improved vegetation management, and improved computational fire models.

Extensive research has been conducted on embers and firebrands, examining firebrand mass and morphology [9–10], generation [10–14], transport [15–18], and viability to ignite spot fires [9,19–23]. Firebrand generators have been developed for laboratory studies [11–14]. Firebrand behavior has simulated using geometric scaling, analytical models, and numerical models [14–18].

A firebrand generator was developed by Manzello et al. [11–12] to emulate the firebrands produced from burning trees, characterize their size and mass, and compare varying the effect of wind velocities [11–12]. Suzuki et al. [10] imitated real-scale buildings, generated firebrands from structures of oriented strand board (OSB) and

from wood studs from a sofa, and characterized the firebrand size and mass. A firebrand generator was used to ignite wood fencing and structures exposed to firebrand showers [13].

The flight paths and life times of firebrands with forced convection were studied by Tarifa et al [15]. Oliveira et al. [16] proposed mathematical models of cylindrical wind-driven firebrands trajectories while varying wind velocities. They considered initial orientation, oscillation, rotation, mass, size, time and distance travelled. Numerical modeling of trajectories of spherical, cylindrical, and disk firebrands was performed by Anthenien et al [17]. Tse et al [18] predicted the flight distance of burning materials such as hot particles, burning sparks, and burning embers being carried with numerical model.

Firebrand physical properties such as mass, weight, surface area, and surface to volume ratio were investigated by Ganteaume et al. [9]. They also examined ignitability, sustainability, combustibility, and thermal decomposition. Kuznetsov et al [20] tested the ignition of pine wood with varying heat fluxes. Manzello et al [22] did experiments to understand how firebrands ignite various types of mulch and cut grass with different sizes, wind velocities, and states of flaming. They also studied the effects of crevice angle for plywood and OSB on ignition by firebrands [21]. Higher airflows generated higher surface temperatures of glowing firebrands, which led to increased heat flux from the firebrand and increased net heat flux to the fuel bed.

1.2 Motivation

The key attributes of a firebrand are its size and temperature. While firebrand sizes have been measured in real fires, much less is known about the temperatures of embers

as well as firebrands. This could be impeding fire safety because cool firebrands are not viable ignition sources and may be incapable of self-sustained burning, whereas hot and small firebrands have short burning durations. If the temperatures of airborne firebrands showers [10, 24] can be measured easily and accurately in laboratories and in wildland fires, this could be transformational. The hazards of various firebrand materials and moisture contents could be better assessed. Computational fire models could be improved. Also, for example, different gutters, roofs design, and shrub management would be required for houses in WUI depending on the surrounding vegetation and its firebrand characterization. If firebrand size could be simultaneously measured with the same device, both key firebrand attributes could be determined in near real time.

1.3 Technical gaps

Little previous research has been performed regarding ember or firebrand temperature measurement. Measurements have been performed with thermocouples [21,25], but these suffer from poor thermal contact, smolder quenching, and conductive losses. Ember pyrometry has been performed with infrared (IR) imagers and IR spot detectors. Temperatures of 190 – 946 °C have been reported [5,7,21,26]. Smoldering ember temperatures of 500 – 600 °C were found with an IR radiometer on a drone in daytime and at night by Cheng et al. [7]. Fateev et al. [26] measured a minimum smoldering temperature of 190 °C with an IR imager. Manzello et al. [21] and Urbas et al. [25] observed temperatures of 800 – 946 °C by assuming emissivities (ε) of 0.6 – 1 using infrared measurements validated by thermocouples [5]. Recently, Hakes et al. [27] obtained temperatures of firebrand piles only qualitatively using an IR camera.

However, these IR pyrometers have several drawbacks: surface emissivity must be known or estimated [5,21,25]; the surface emissivity generally increases as a firebrand burns [28]; ash and smoke along the line of sight can decrease the indicated temperature; and the ember image must fill at least one pixel or the spot detector. These drawbacks are compounded for IR imagers because, compared to modern color cameras, they have low pixel counts, low bit depths, low sensitivity, and high costs. For example, the IR imager used by Ref. [5] for ember pyrometry (FLIR Model A8300sc) costs US$ 100,000 but has only 0.9 megapixels.

Recently, Urban et al. [29] demonstrated the surface temperature of glowing embers with different air flows using ratio pyrometry, which is related to my Ph. D dissertation topic. Comparing infrared camera measurement, authors verified ratio pyrometry is more accurate. However, the spatial resolution was limited due to a decreased signal to noise ratio (SNR) from ratio pyrometry. Also, ember emissivity and ash and smoke transmittance were not measured.

To summarize, not only does little past work exist concerning firebrand temperatures, but all previous works failed to measure the temperatures accurately and precisely, mostly using infrared imagers or thermocouples (typically used for charring materials [23]). Thus, the main purpose of this dissertation is to develop a nonintrusive and inexpensive ember pyrometry to measure ember temperature and emissivity accurately and precisely.

1.4 Objectives

The hypothesis of this research is as follows: combined ratio and grayscale pyrometry with a color camera can accurately measure firebrand temperature and emissivity in the

visible. The ultimate long-term goal is to develop an inexpensive and accurate diagnostic of a stationary ember and airborne firebrand temperature measurement in real fire scenarios.

Ratio pyrometry can be very accurate. Compared to grayscale pyrometry, it has several advantages for fire embers. First, its temperatures are independent of firebrand size or distance from the detector. Second, it is less impacted by smoke, ash, or other attenuation along the line of sight. Third, it does not require an assumed emissivity of the fuel surface. Fourth, it allows firebrand size to be measured in addition to temperature.

On the other hand, ratio pyrometry has lower signal-to-noise ratios (SNRs) compared to grayscale pyrometry. Grayscale pyrometry generally requires: blackbody behavior of the hot surface; negligible radiative extinction from ash and smoke; and no temporal drift or ambient temperature dependence from the camera.

During my Ph. D, a major part of the effort was to develop a new diagnostic for smoldering ember temperature that combined both ratio and grayscale pyrometry with a consumer color camera. Both pyrometry methods were calibrated with a blackbody furnace at precisely controlled temperatures. To date, no study has measured with sufficient accuracy the temperatures of embers or firebrands undergoing self-sustained smoldering. Thus, a nonintrusive and inexpensive ember pyrometry was developed using a color camera. By combining ratio and grayscale pyrometry, a hybrid pyrometer was developed that incorporates the accuracy of ratio pyrometry and the low noise of grayscale pyrometry. The measurements also yield the ember emissivity in the visible range. The pendulum firebrand temperature imitating airborne firebrands in a real fire

scenario was also investigated. The relationship between the velocity of firebrands and their temperatures was quantified.

Additionally, a second major part of the effort was to fundamentally and experimentally understand the smoldering extinction behavior with varying high air velocity. Little is known about the extinction of smoldering at high air velocity. The smoldering temperature and burning rate was primarily investigated using the developed pyrometry performing on various smoldering materials.

The below are the main objectives.

(1) Acquire and assemble materials (a digital camera and a blackbody furnace).

(2) Calibrate pyrometer with the blackbody furnace.

(3) Generate reproducible embers.

(4) Perform pyrometry on stationary embers.

(5) Perform pyrometry on pendulum firebrands.

(6) Perform pyrometry on smoldering materials.

Chapter 2: Pyrometer Calibration

2.1 Introduction

An alternative temperature measurement technique, instead of using thermocouples or infrared imagers, is pyrometry in visible wavelengths such as ratio and intensity pyrometry. Ratio pyrometry requires less knowledge about the surface emissivity.

Imaging ratio pyrometry can be multi-wavelength or multi-band pyrometry [30]. Multi-wavelength pyrometry involves bandpass filters external to the camera. Consumer-grade color cameras have been used extensively to perform ratio pyrometry of soot [31–35].

More recently, this method has been used for surface pyrometry. In multi-band pyrometry, the color filter array on the CCD or CMOS chip is used to obtain the red, green, and blue emissions. Lu et al. [28] measured temperatures of embers burning inside flow reactors with wall temperatures above 1000 °C. This environment is more representative of biomass combustors than that which a firebrand encounters after being lofted tens or hundreds of meters.

Similar measurements were performed for burning coal particles [36–38]. But these are hotter than wood embers and cannot burn unaided in the air. These pyrometers are often calibrated by measuring char particles temperatures with thermocouples [39–40].

Ratio pyrometry has been applied to heated materials at 500 – 1930 °C [41–43], but the materials were not flammable. Zander [41] measured temperatures of materials that were heated resistively or with a plasma torch to above 1230 °C. In the HST3 free piston driven shock tunnel, the temperature distribution was measured in the radiating shock layer in the flow by Deep et al with DSLR camera-based two-color ratio

pyrometry [42]. Raj et al. [43] measured the temperature and emissivity of solid materials such as Inconel and stainless steel using two color pyrometry. More recently, hot metal sparks temperatures were determined by color ratio pyrometry by Liu et al [44].

To summarize, only one past study measured the temperature of embers or firebrands using ratio pyrometry undergoing self-sustained smoldering [29]. That study had limited spatial resolution and SNRs. Furthermore, no past study has exploited the accuracy of ratio pyrometry and the precision of grayscale pyrometry.

This chapter elucidates pyrometry calibration.

ISO, f number, and exposure time were all normalized. The effect of camera zooms setting, white balance, and the distance between the blackbody source were studied.

The calibration was confirmed with pyrometry performed on blackbody images.

2.2 Pyrometer components

2.2.1 Digital camera

Imaging was performed with a Sony DSC-RX10 III cyber-shot digital camera, shown in Figure 2-1. This has a 1.3 × 0.9 cm Exmor RS stacked back-illuminated complementary metal-oxide semiconductor (CMOS) sensor with 20.1 megapixels and

Figure 2-1 Digital camera, Sony DSC-RX 10 III.

a bit depth of 14 in each color plane. The stacked CMOS sensor from RX10 III provides excellent image quality and processing efficiency. Sony RX10 III images are sharp, clear and well- exposed. It has fast continuous shooting at a rate up to about 14 fps. Table 2-1 represents comparison of specifications of the digital camera with infrared devices. The lens was built in the camera and is not interchangeable. The lens was a Zeiss Vario-Sonnar T* Lens, with variable zoom (8.8 – 220 mm) and f (2.4 – 4). A Hoya 72 mm protector filter was attached to the lens to facilitate cleaning. Although BG7 colored glass filters [35,45] or interference bandpass filters [31,46] are common

in soot pyrometry, no filters were used here so the transient burning could be observed with the shortest exposure times. For example, images of the blackbody furnace at 1000 °C with a BG7 filter required a factor of 60 increase in exposure time to obtain comparable greyscale pixel values.

To avoid rolling shutter distortions only the mechanical shutter was used. The white balance was daylight, but this had no effect because the images were recorded in RAW format. The ISO (International Organization for Standardization) range was 100 – 400,

Table 2-1 Specifications of a digital camera and FLIR.

Device	Model	Bit depths	Detector Resolution	Response time	Accuracy	Precision	Cost
A digital camera	Sony RX 10 III	42	5496X3672	1.3 ms	±25 °C	+/- 0.0005 C	$1,298
Infrared Camera	FLIR E95	24	464X348	N/A	±35 °C	N/A	$9,999
	FLIR A8300sc	42	1280 x 720	500 ns	±2°C	N/A	$100,000
	FLIR X6800sc	42	640 x 512	270 ns	±2°C	N/A	$110,000

FLIR A8300sc was used for combustion in a supersonic flow [5]. FLIR X6800sc was used for a glowing firebrand [47].

which for this camera controls the electrical gain, rather than image postprocessing.

The RAW images were converted to 16-bit tiff images using dcraw [48] with default settings except –4 and –T [31]. The tiff files were opened in ImageJ. Rectangular regions were selected and for these the pixel coordinates and the red, green, and blue pixel values (I_R, I_G, and I_B) were exported. Saturation occurred at a pixel value of 65535.

2.2.2 Blackbody furnace

The camera was calibrated with a blackbody furnace (Oriel 67032), shown in Fig. 2-2. It has a maximum temperature of 1200 °C, a temperature accuracy of ±0.2 °C, an emissivity (ε) of 0.99 ± 0.01, and an aperture diameter of 25 mm. A similar blackbody

Figure 2-2 Blackbody furnace (Oriel 67032).

was found to have ε = 0.99 for wavelengths between 0.5 – 4 μm [49]. The lens was 1 cm away and was focused on the aperture. Exposure times were adjusted such that the highest pixel values (always red) were close to saturation but none was saturated.

2.3 Camera Calibration

2.3.1 Dark current

Dark current is the signal from a photodetector when there is no incident light. In Fig. 2-3, dark images were recorded at various shutter times to determine dark-current pixel values, I_{DC}. Various ISOs were considered. At ISO 200, these intensities were small

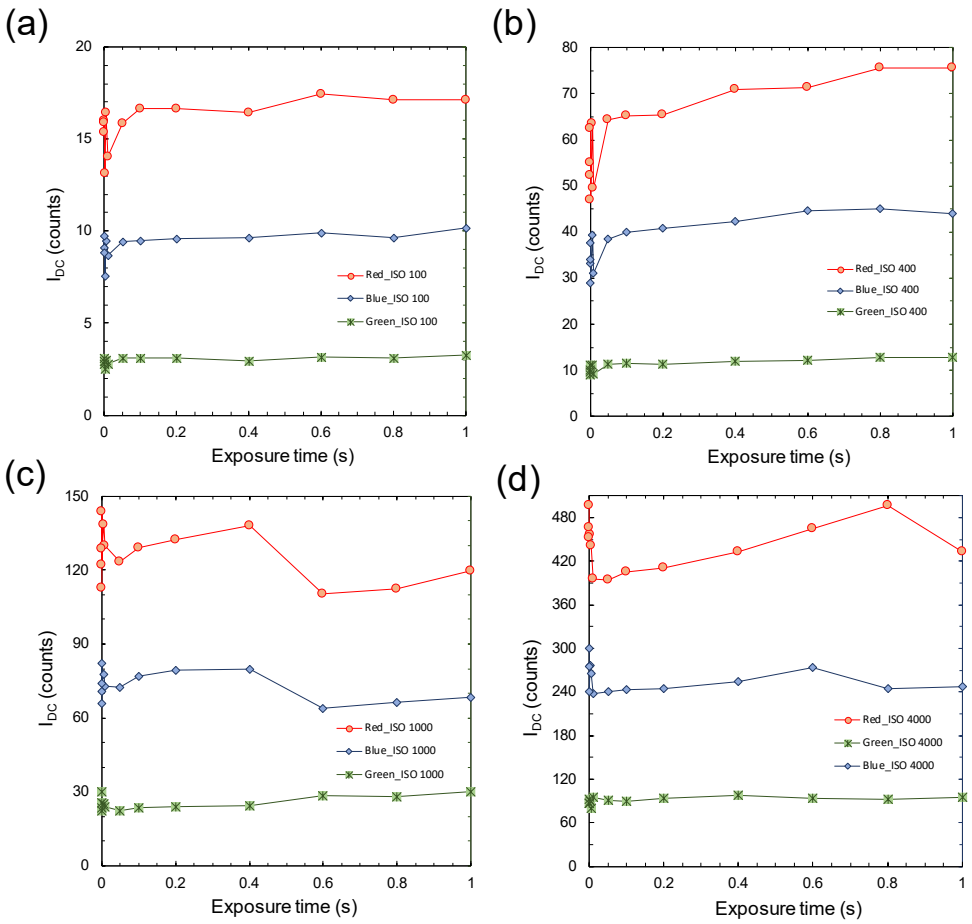

Figure 2-3 RGB counts of dark currents plotted with respect to exposure time from 0.00005 – 1 s with (a). ISO 100; (b). ISO 400; (c). ISO 1000; and (d). ISO 4000. F number was 2.4. Intensities were exported with MATLAB tool.

(below 20 counts in each color plane) and had negligible variation with shutter time. It may come from dark currents of a CMOS sensor from the SONY camera, which is pretty fixed in terms of unit sensor area. Also, dark noise from CMOS is significantly less than CCD providing higher overall contrast and a more clear image [50]. Fig. 2-4 represents dark current signal with respect to ISO for each plane. As ISO increases from 0 – 4000, intensities increase from 400 in the highest pixel values (red). These were still small relative to 65536 at saturation. For this camera ISO is an electronic gain on the chip and exposure compensation is a postprocessing operation.

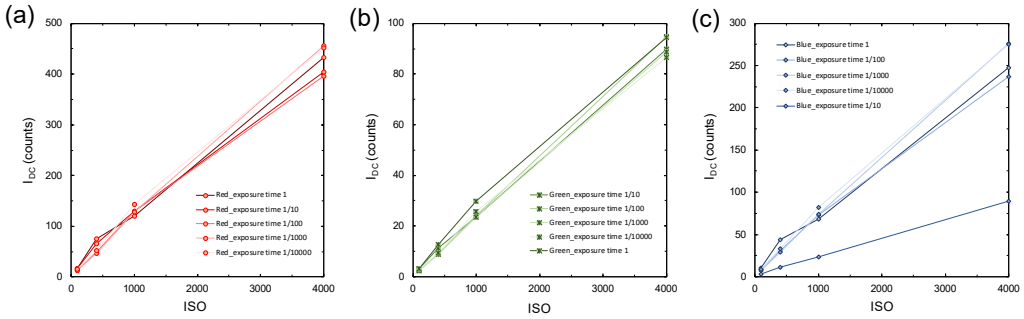

Figure 2-4 Intensities of dark currents with exposure time of 0.00001 – 1 s plotted with respect to ISO from 100 to 4000 for each color planes (a). Red; (b). Green; and (c). Blue. F number was 2.4.

2.3.2 Blackbody images

Blackbody images were recorded at 600 – 1200 °C and were used to calibrate the camera. Fig. 2-5 is a representative color image of blackbody. The brightest red pixel values were nearly 60000. For each blackbody image a 200 × 200 pixel area centered on the middle of the blackbody was selected, this corresponding to about 5% of the

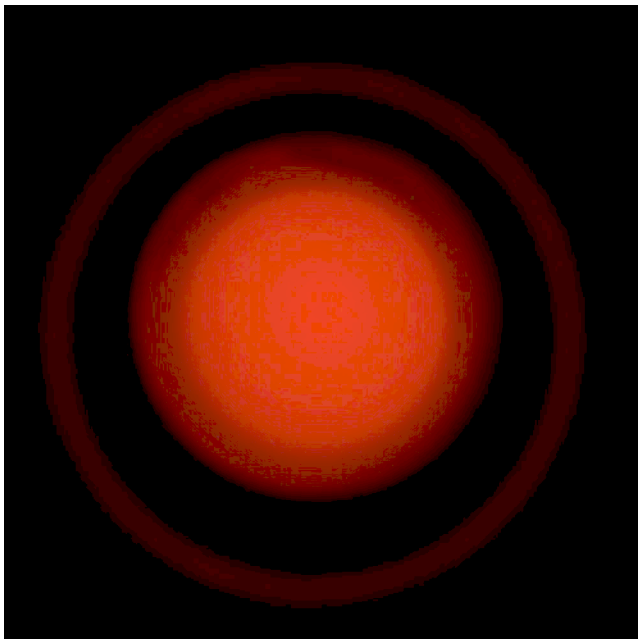

Figure 2-5 A representative color image (2400 × 2400 pixels) of blackbody images at 1000 °C. For this, *ISO* = 200, *f* = 2.4 (the camera minimum), and *t* = 2 ms.

blackbody area. For this region, the means of I_R, I_G, I_B, and I_{GS} were found with respect to blackbody temperature.

2.3.3 Linear response to exposure time

Blackbody intensities were measured by varying exposure time at fixed temperatures. Fig. 2-6 shows raw data so collected. The red pixel values were higher than those of blue and green. Schott colored optical filters were considered, but this increased the

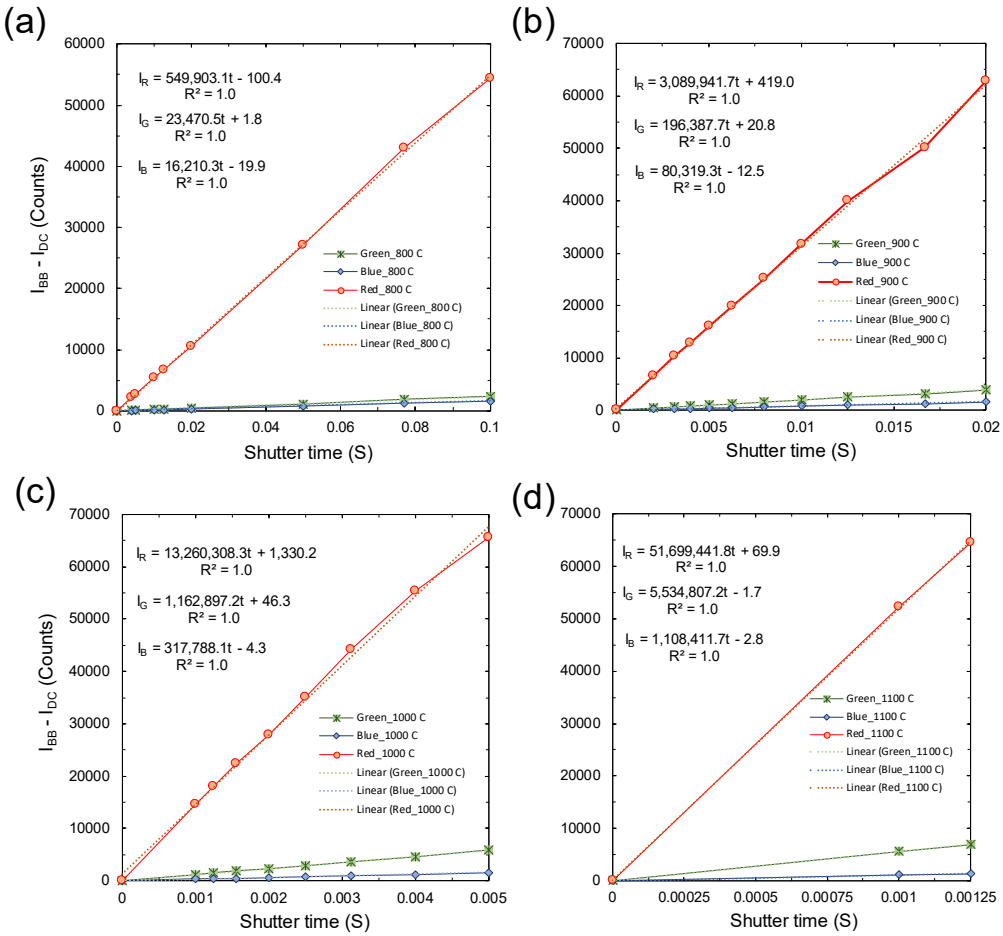

Figure 2-6 Linear response to shutter time at fixed temperatures with (a). 800 °C; (b). 900 °C; (c). 1000 °C; and (d). 1100 °C. F number and ISO were 2.4 and 100.

required shutter time by about an order of magnitude.

The camera response is linear in shutter time and inversely proportional to f-number squared.

2.3.4 Effect of white balance

White balance is a camera setting that attempts to yield realistic colors. It involves image postprocessing. Fig. 2-7 shows the effects of white balance settings. Various settings were tested, including daylight, cloudy, incandescent, warm white, flash, and auto, and there was no difference in the raw files produced.

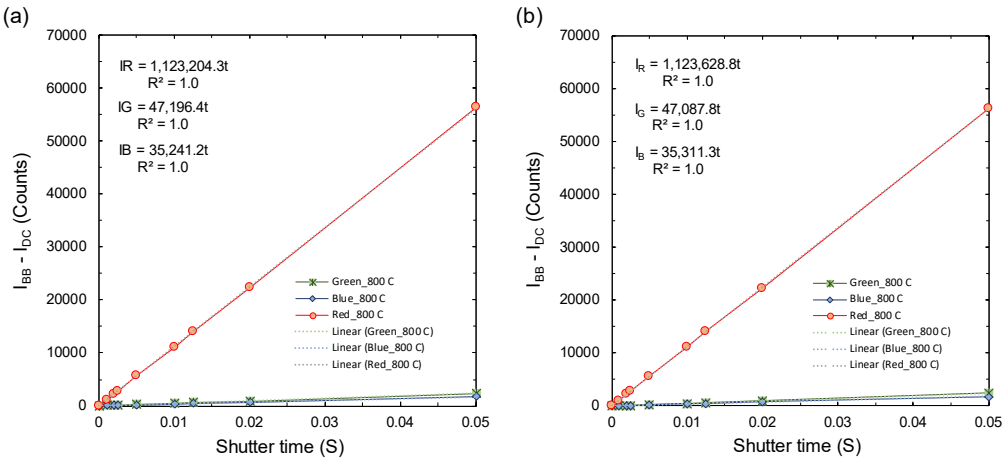

Figure 2-7 Linear response to shutter time at the fixed temperature of 800 °C with different white balance setting (a). daylight; and (b). shade. ISO and f number were 200 and 2.4. Electronic shutter setting was used.

2.3.5 Effect of focal length and distance

Blackbody intensities were measured while varying the focal length and the distance to the blackbody. Images were recorded as shown in Fig. 2-8 at 800 °C. The ISO, shutter time, and f-number were fixed at 200, 0.0667 s, and f/4, respectively. The resulting intensities are plotted in Fig. 2-9 with respect to focal length at a fixed distance and with respect to distance at a fixed focal length. The response was independent of

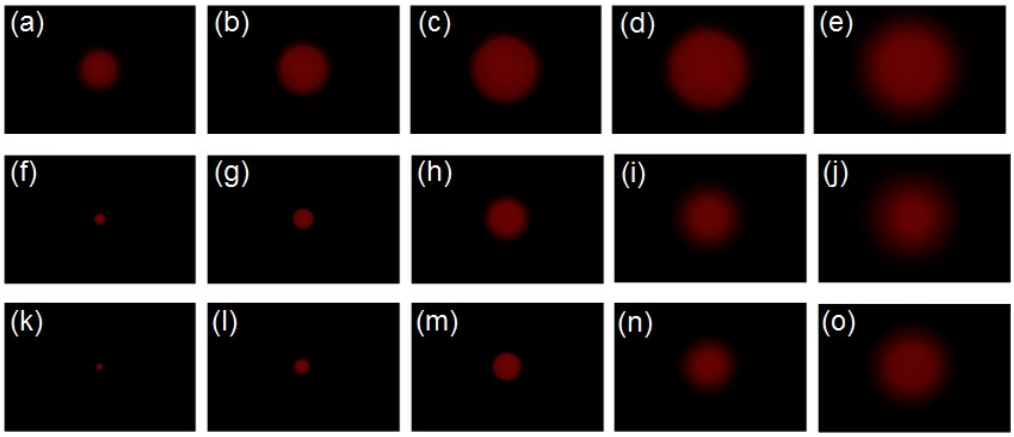

Figure 2-8 Blackbody images varying focal length and distance. Distance of 2.6 cm with focal length of (a). 24 mm; (b). 40 mm; (c). 65 mm; (d). 100 mm; and (e). 144 mm. Distance of 25.9 cm with focal length of (f). 24 mm; (g). 50 mm; (h). 131 mm; (i). 221 mm; and (j). 351 mm. Distance of 48.7 cm with focal length of (k). 24 mm; (l). 70 mm; (m). 144 mm; (n). 300 mm; and (o). 500 mm.

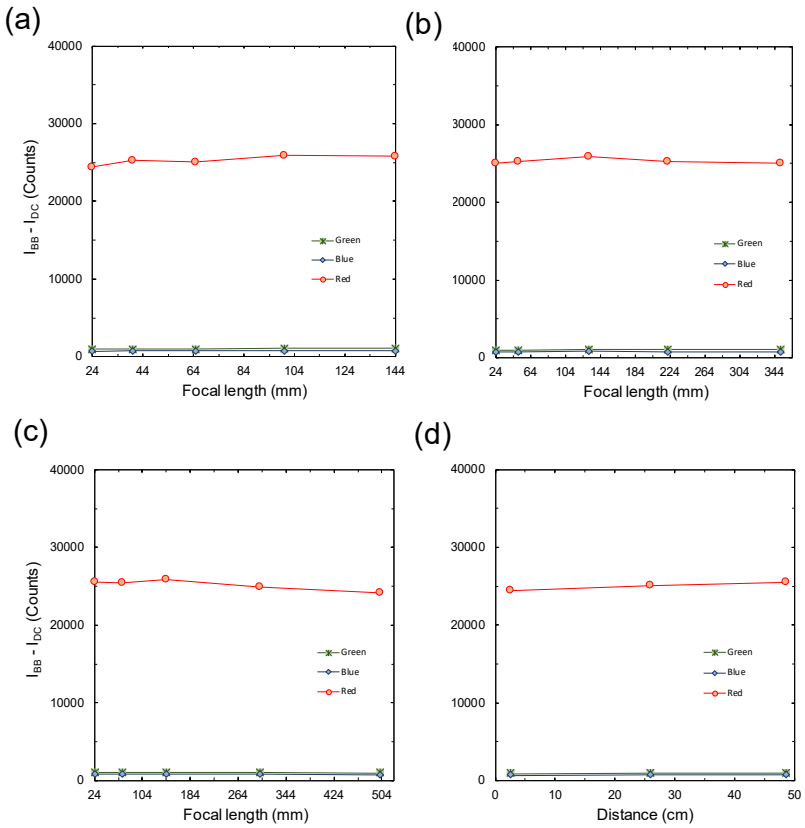

Figure 2-9 Intensities plotted with respect to focal length (24 mm – 144 mm) with distances of (a). 2.6 cm; (b). 25.9 cm; and (c). 48.7 cm and respect to distance with a focal length of (d) 24 mm.

either lens zoom or distance from the blackbody. It did not follow Newton's Inverse

Square Law that light intensity is inversely proportional to distance squared from the blackbody source until 50 cm and longer distance measurement will be needed.

2.3.6 Blackbody normalized intensities

Grayscale pixel values were defined as

$$I_{GS} = (I_R + I_G + I_B) / 3 \,, \tag{2-1}$$

and normalized pixel values were defined as

$$NI_i = (I_i - I_{i,DC}) f^2 / t\, ISO, \tag{2-2}$$

where f is f-number, i denotes R, G, B, or GS, and t is exposure time.

In each image of the blackbody a 200 × 200 pixel region was considered. The resulting mean normalized pixel values are plotted with respect to blackbody temperature in Fig. 2-10. The normalization of Eq. (2-2) collapses the measurements for various f, ISO, and t. There is a 4 – 5 order of magnitude increase in NI as blackbody temperature increases from 600 – 1200 °C. The red pixel values are the highest, and those for green are higher than for blue except at low temperatures. Additional tests (not included in Fig. 2-10) found these correlations to be independent of both lens zoom and distance from the blackbody as represented in Fig 2-9.

The spectral emissive power of an ideal blackbody is

$$E_{\lambda b} = C_1 / \lambda^5 [\exp (C_2 / \lambda T) - 1] \,, \tag{2-3}$$

where C_1, C_2, T, and λ are, respectively, first and second radiation constants (3.742×10^{-16} W-m^2 and 0.01439 m-K), temperature, and wavelength. Quantity $E_{\lambda b}$ is plotted in Fig. 2-10 at 430 and 680 nm, which are close to the peak sensitivities of similar cameras in the blue and red planes [41,45,51]. Among the six curves in Fig. 2-10, five have

similar shapes. However, the NI_B curve has a smaller slope owing to the behavior of the CMOS and/or its filter mask.

The *NI* correlations in Fig. 2-10 allow pyrometry on hot objects such as embers. This can be ratio pyrometry, based on one or more *NI* ratios, or grayscale pyrometry,

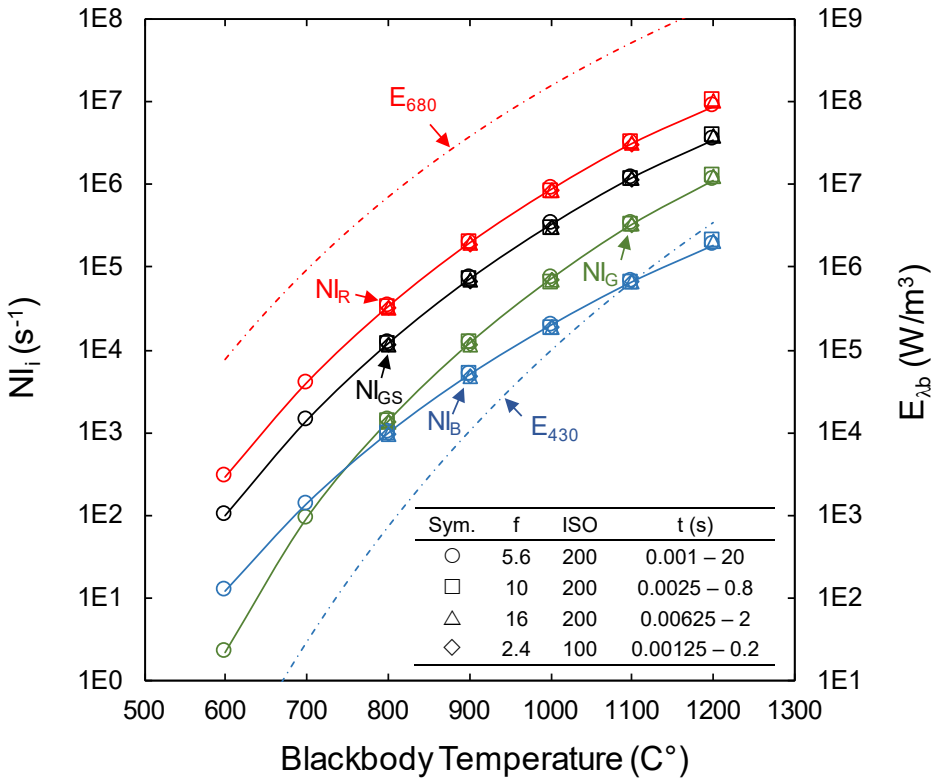

Figure 2-10 Measured normalized pixel values of the blackbody furnace images. Also shown is the spectral emissive power at 430 and 680 nm.

based on NI_{GS}. Ratio pyrometry has lower signal-to-noise ratios (SNRs). On the other hand, grayscale pyrometry generally requires: blackbody behavior of the hot surface; negligible radiative extinction from ash and smoke; and no temporal drift or ambient temperature dependence in the camera.

2.3.7 Blackbody intensity ratios

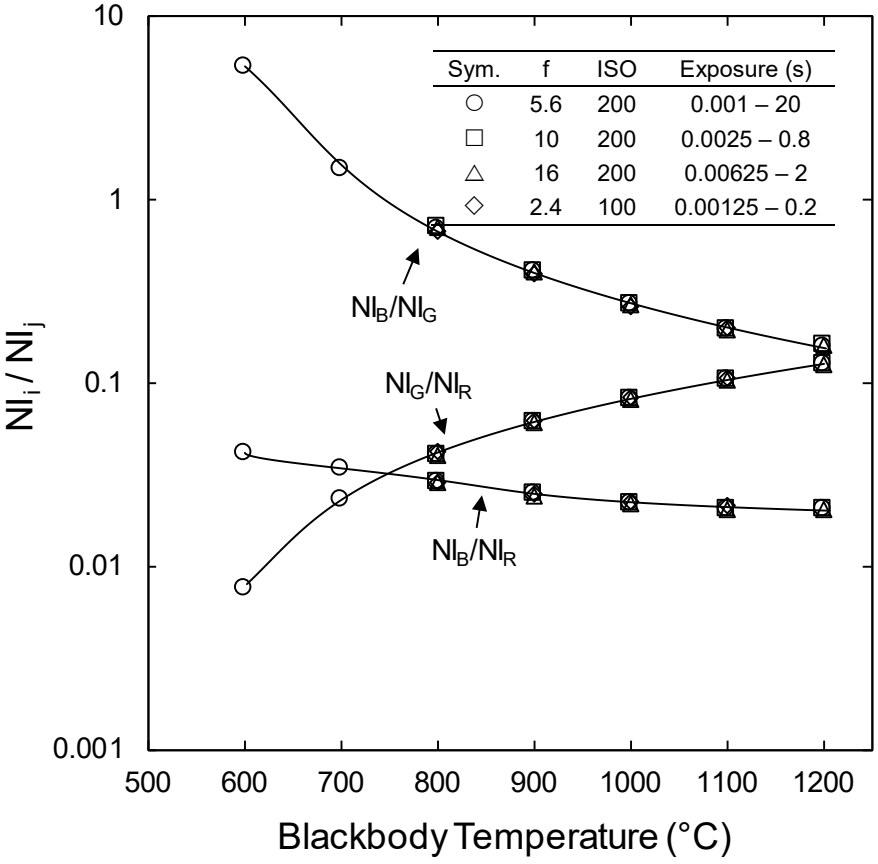

Figure 2-11 Normalized intensity ratios of the blackbody furnace images.

For ratio pyrometry the three *NI* of Fig. 2-10 are converted to three ratios as plotted in Fig. 2-11. These are smooth and monotonic with respect to temperature. A camera whose red, green, and blue planes had no wavelength overlap would yield a monotonic increase in these ratios with increasing temperature. Such monotonicity has been observed before for some cameras [28,45,51], but not for others [42,52]. It is seen in Fig. 2-11 only for G/R. Both ratios involving the blue color plane decrease with temperature owing to the low slope of NI_B evident in Fig. 2-10.

The B/R curve in Fig. 2-11 is too flat for pyrometry with reasonable signal-to-noise ratios. B/G ratio pyrometry was found to yield unacceptably high scatter because it omits the red pixels, which have the highest pixel values and the highest signal-to-noise ratios. Thus, only G/R is considered below for ratio pyrometry.

The variation in NI_G / NI_R in Fig. 2-11 varies by only a factor of 16, indicating a decreased signal-to-noise ratio for ratio pyrometry as compared to grayscale pyrometry using Fig. 2-10. Pyrometry performed on the blackbody images indicated SNRs (the temperature mean divided by standard deviation) of 30 and 530 for ratio and grayscale pyrometry, respectively. These values vary by a factor of 18.

2.4 Curve Fits for NI_{GS} and NI_i/NI_j

2.4.1 Intensity Pyrometry

The curve fit for NI_{GS} in Fig. 2-10 is a 2nd order best-fit polynomial of T in terms of $\log_{10}(NI_{GS})$ as shown in Fig. 2-12. It was used to convert NI_{GS} to firebrand and smoldering material temperatures.

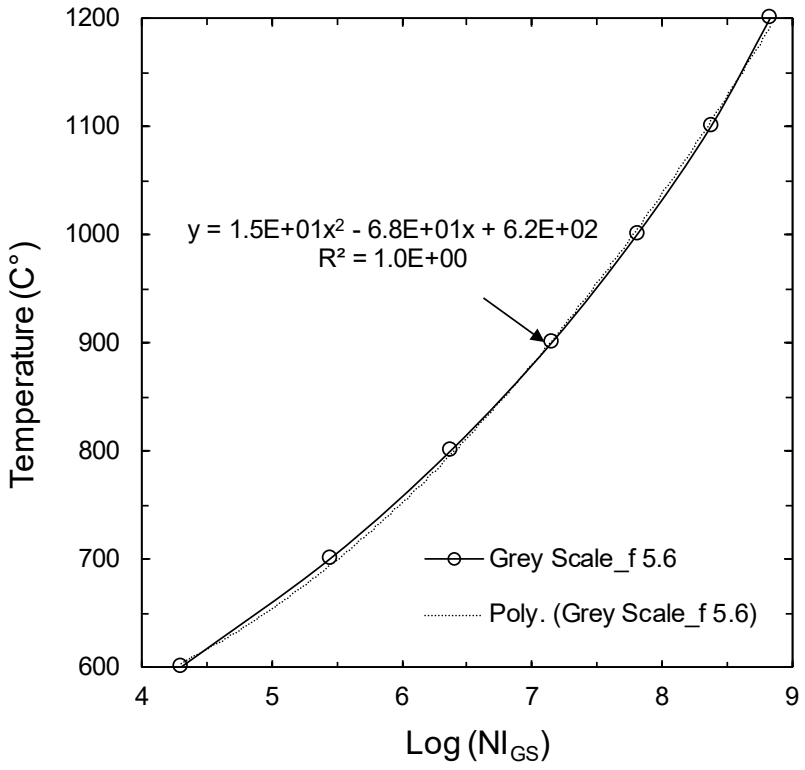

Figure 2-12 Temperature plotted with respect to normalized intensity.

2.4.2 Ratio Pyrometry

The curve fits for NI_i / NI_i in Fig. 2-11 are 3rd and 4th order best-fit polynomials of $\log_{10}(NI_i / NI_j)$ in terms of T as shown in Fig. 2-13. From three ratios, the G/R ratio was used to convert NI_{GS} to firebrand and smoldering material temperatures. Fig. 2-14 represents all pyrometry data in Excel.

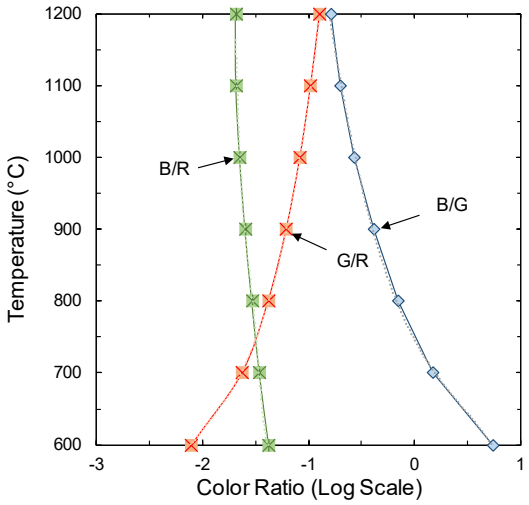

DSC-RX10 III Cyber-shot digital camera, Sony
No filter, ISO : 200, f# : 5.6
Mechanical shutter
Pixel counts : middle 200 x 200 square

$y_{G/R} = 2.92E+02x^3 + 1.73E+03x^2 + 3.61E+03x + 3.25E+03$
$R^2 = 1.00E+00$

$y_{B/R} = 2.59E+05x^4 + 1.57E+06x^3 + 3.56E+06x^2 + 3.59E+06x + 1.35E+06$
$R^2 = 9.89E-01$

$y_{B/G} = -1.70E+02x^3 + 2.27E+02x^2 - 2.75E+02x + 7.46E+02$
$R^2 = 9.99E-01$

Figure 2-13 Temperature plotted with respect to color ratio.

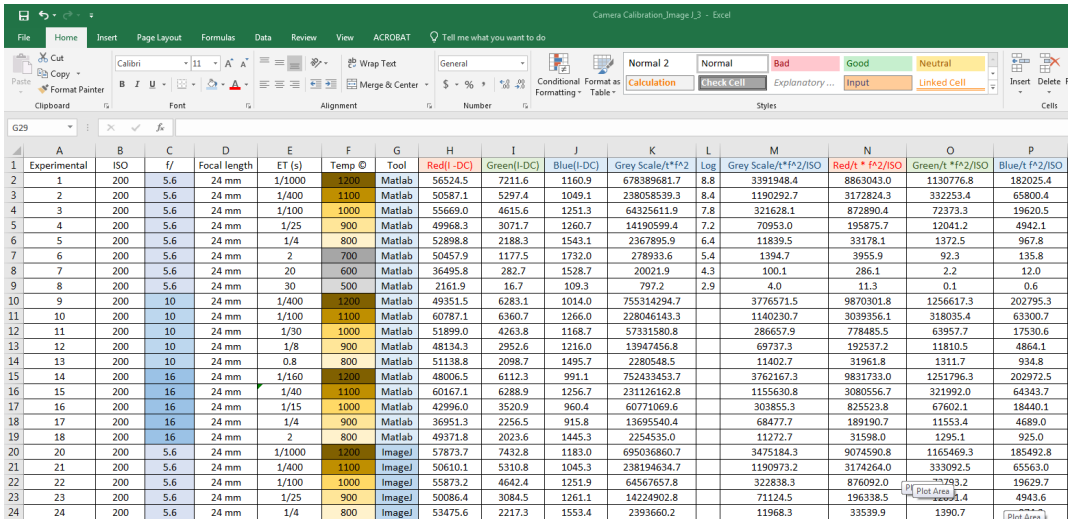

Experimental	ISO	f/	Focal length	ET (s)	Temp ©	Tool	Red(I -DC)	Green(I-DC)	Blue(I-DC)	Grey Scale/t*f^2	Log	Grey Scale/t*f^2/ISO	Red/t * f^2/ISO	Green/t *f^2/ISO	Blue/t f^2/ISO
1	200	5.6	24 mm	1/1000	1200	Matlab	56524.5	7211.6	1160.9	678389681.7	8.8	3391948.4	8863043.0	1130776.8	182025.4
2	200	5.6	24 mm	1/400	1100	Matlab	50587.1	5297.4	1049.1	238058539.3	8.4	1190292.7	3172824.3	332253.4	65800.4
3	200	5.6	24 mm	1/100	1000	Matlab	55669.0	4615.6	1251.3	64325611.9	7.8	321628.1	872890.4	72373.3	19620.5
4	200	5.6	24 mm	1/25	900	Matlab	49968.3	3071.7	1260.7	14190599.4	7.2	70953.0	195875.7	12041.2	4942.1
5	200	5.6	24 mm	1/4	800	Matlab	52898.8	2188.3	1543.1	2367895.9	6.4	11839.5	33178.1	1372.5	967.8
6	200	5.6	24 mm	2	700	Matlab	50457.9	1177.5	1732.0	278933.6	5.4	1394.7	3955.9	92.3	135.8
7	200	5.6	24 mm	20	600	Matlab	36495.8	282.7	1528.7	20021.9	4.3	100.1	286.1	2.2	12.0
8	200	5.6	24 mm	30	500	Matlab	2161.9	16.7	109.3	797.2	2.9	4.0	11.3	0.1	0.6
9	200	10	24 mm	1/400	1200	Matlab	49351.5	6283.1	1014.0	755314294.7		3776571.5	9870301.8	1256617.3	202795.3
10	200	10	24 mm	1/100	1100	Matlab	60787.1	6360.7	1266.0	228046143.3		1140230.7	3039356.1	318035.4	63300.7
11	200	10	24 mm	1/30	1000	Matlab	51899.0	4263.8	1168.7	57331580.8		286657.9	778485.5	63957.7	17530.6
12	200	10	24 mm	1/8	900	Matlab	48134.3	2952.6	1216.0	13947456.8		69737.3	192537.2	11810.5	4864.1
13	200	10	24 mm	0.8	800	Matlab	51138.8	2098.7	1495.7	2280548.5		11402.7	31961.8	1311.7	934.8
14	200	16	24 mm	1/160	1200	Matlab	48006.5	6112.3	991.1	752433453.7		3762167.3	9831733.0	1251796.3	202972.5
15	200	16	24 mm	1/40	1100	Matlab	60167.1	6288.9	1256.7	231126162.8		1155630.8	3080556.7	321992.0	64343.7
16	200	16	24 mm	1/15	1000	Matlab	42996.0	3520.9	960.4	60771069.6		303855.3	825523.8	67602.1	18440.1
17	200	16	24 mm	1/4	900	Matlab	36951.3	2256.5	915.8	13695540.4		68477.7	189190.7	11553.4	4689.0
18	200	16	24 mm	2	800	Matlab	49371.8	2023.6	1445.3	2254535.0		11272.7	31598.0	1295.1	925.0
19	200	5.6	24 mm	1/1000	1200	ImageJ	57873.7	7432.8	1183.0	695036860.7		3475184.3	9074590.8	1165469.3	185492.8
20	200	5.6	24 mm	1/400	1100	ImageJ	50610.1	5310.8	1045.3	238194634.7		1190973.2	3174264.0	333092.5	65563.0
21	200	5.6	24 mm	1/100	1000	ImageJ	55873.2	4642.4	1251.9	64567657.8		322838.3	876092.0	32793.2	19629.7
22	200	5.6	24 mm	1/25	900	ImageJ	50086.4	3084.5	1261.1	14224902.8		71124.5	196338.5	6269.4	4943.6
23	200	5.6	24 mm	1/4	800	ImageJ	53475.6	2217.3	1553.4	2393660.2		11968.3	33539.9	1390.7	

Figure 2-14 Excel Data for Figure 2-12 and Figure 2-13.

2.5 Blackbody Uncertainty

2.5.1 Blackbody uncertainty

Representative blackbody images were used to estimate the pyrometer uncertainties. The calibrations above were confirmed with pyrometry performed on blackbody images recorded at 700 – 1100 °C. Fig. 2-15 represents how many pixels were lost out of a 200 x 200 pixel square from blackbody images when using B/G, B/R, and G/R

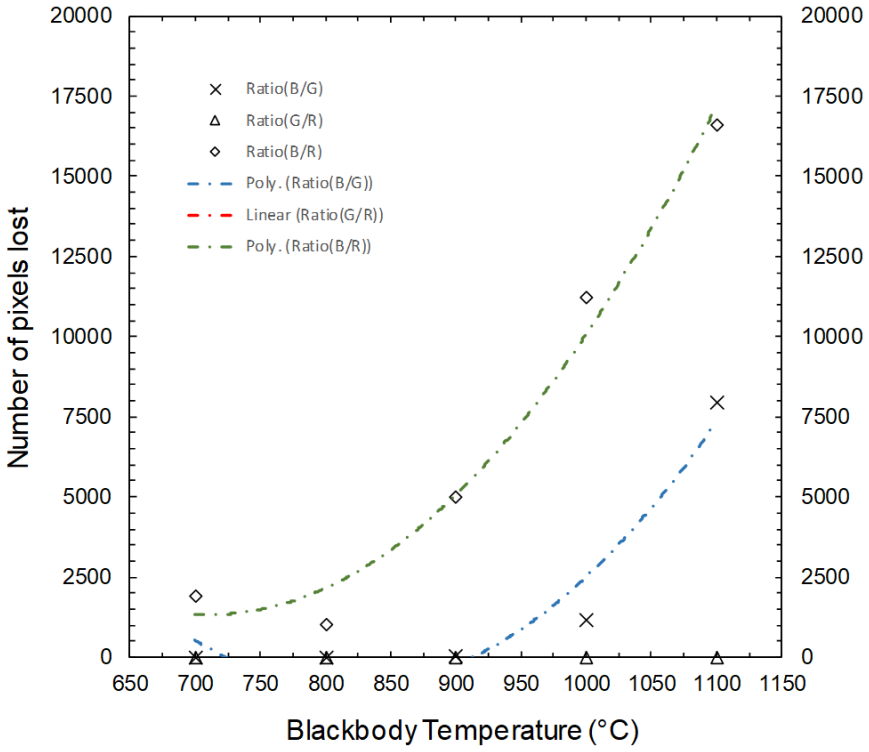

Figure 2-15 Blackbody uncertainty: Number of pixels lost from outside temperature bound and low signal.

pyrometry. Due to weak blue signals with increasing temperature, the number of pixels lost increased to 7500 and 17500 pixels from B/G and B/R pyrometry, respectively. Fig. 2-16 indicates the mean temperatures of 200 × 200 pixels using G/R, B/R, and B/G ratio pyrometry and GS pyrometry to estimate the pyrometer uncertainties. The calibrations from Fig. 2-12 and Fig. 2-13 were used to obtain these pixel temperatures. The blackbody images were interrogated to determine color ratios for each pixel using

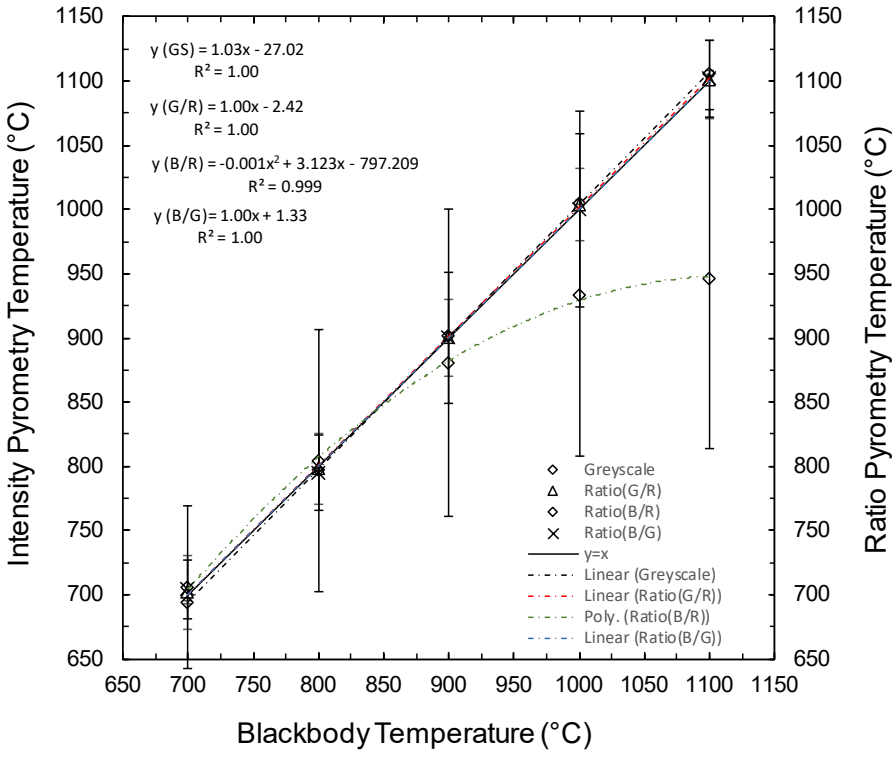

Figure 2-16 Blackbody uncertainty: Mean temperatures from ratios and GS pyrometry with respect to blackbody temperature.

three different fit curves in Fig. 2-13. Polynomials of 3rd and 4th order of $\log_{10}(NI_R / NI_G)$ in terms of temperature were used. To estimate the GS pyrometer uncertainties, a 2nd order best-fit polynomial curve of T in terms of $\log_{10}(NI_{GS})$ was used in Fig. 2-12. The results determined that B/R ratio pyrometry in Fig. 2-16 was completely off the ideal linear fit (y = x) and became worse as the blackbody temperature increased with higher standard deviation. This is due to the curve being too flat in Fig.2-11 as described in section 2.3. Also, B/G pyrometry was found to yield unacceptably high scatter as shown in Fig. 2-15.

Fig. 2-17 and Table 2-2 summarize the mean blackbody temperatures using G/R ratio pyrometry and grayscale pyrometry. For blackbody pyrometry, the uncertainties

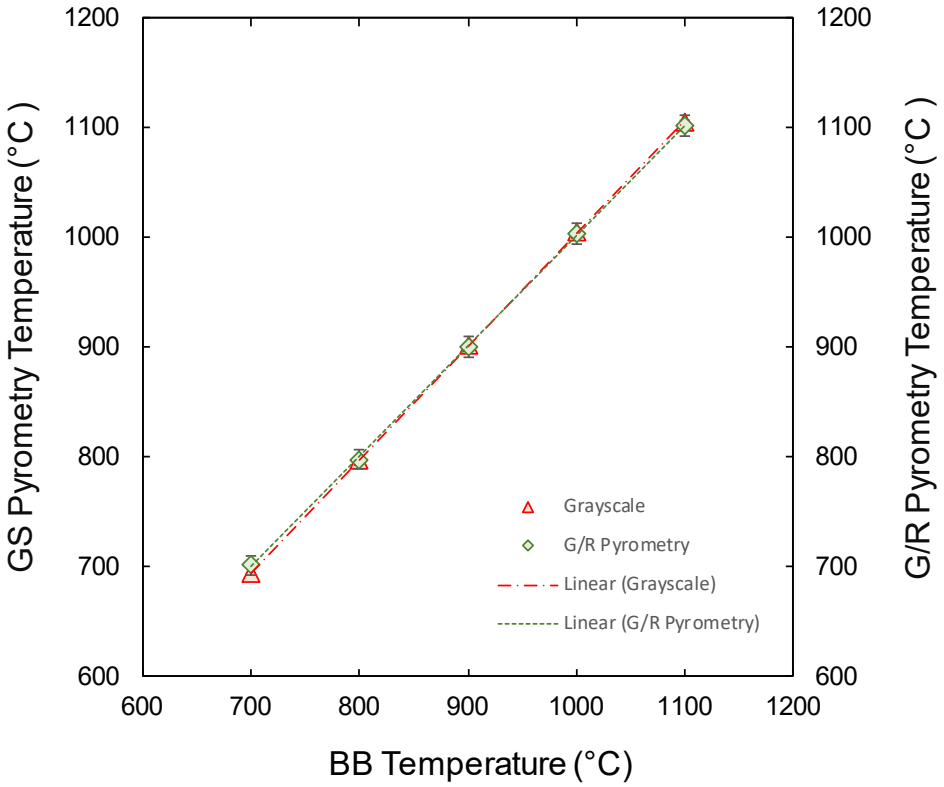

Figure 2-17 Calculated blackbody temperature using G/R ratio pyrometry and GS pyrometry.

of both ratio and grayscale pyrometry for a 7 × 7 pixel region are estimated at ±10 °C. Without any smoothing, the mean temperatures of these pixels were within 3 °C of the blackbody temperature. The absolute value of the difference between the pixel

Table 2-2 Calculated mean temperatures and standard deviation using G/R ratio and GS pyrometry.

Temp	G/R	G/R (Smoothing)	Grayscale	Grayscale (Smoothing)
700	702.0 ± 29.1	702.0 ± 8.9	694.2 ± 0.9	694.2 ± 0.4
800	798.1 ± 28.0	798.2 ± 8.6	797.1 ± 1.3	797.1 ± 0.7
900	900.3 ± 29.8	900.2 ± 9.7	902.1 ± 1.7	902.1 ± 1.1
1000	1003.6 ± 28.4	1003.5 ± 8.9	1005.5 ± 2.0	1005.6 ± 1.3
1100	1101.17± 30.3	1101.8 ± 10.0	1105.5 ± 2.5	1105.6 ± 1.8

temperatures and the blackbody temperature had means of 23 and 4 °C for T_{ratio} and T_{GS}, respectively.

Fig. 2-18 – Fig. 2-22 represent temperature contour plots created in Tecplot, which were converted from blackbody images. Since some pixels were lost from B/R and B/G, some blank cells were filled with linear values from top to bottom and from left to right in Excel. It was verified that blue signals yielded unacceptable high scatter in images of the blackbody from all temperatures. G/R ratio pyrometry was accurate without any signal loss.

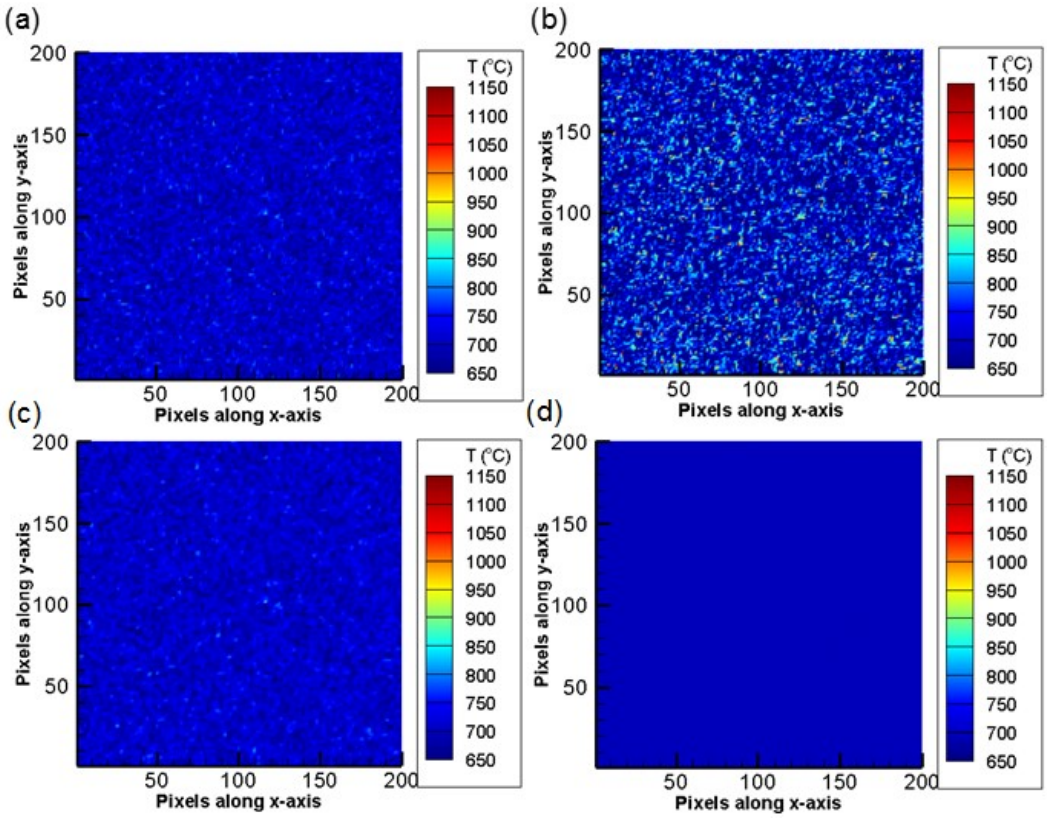

Figure 2-18 Temperature contour plots converted from blackbody images recorded at 700 °C using three normalized intensity ratio curves: (a). G/R; (b). B/R; (c). B/G; and (d). GS.

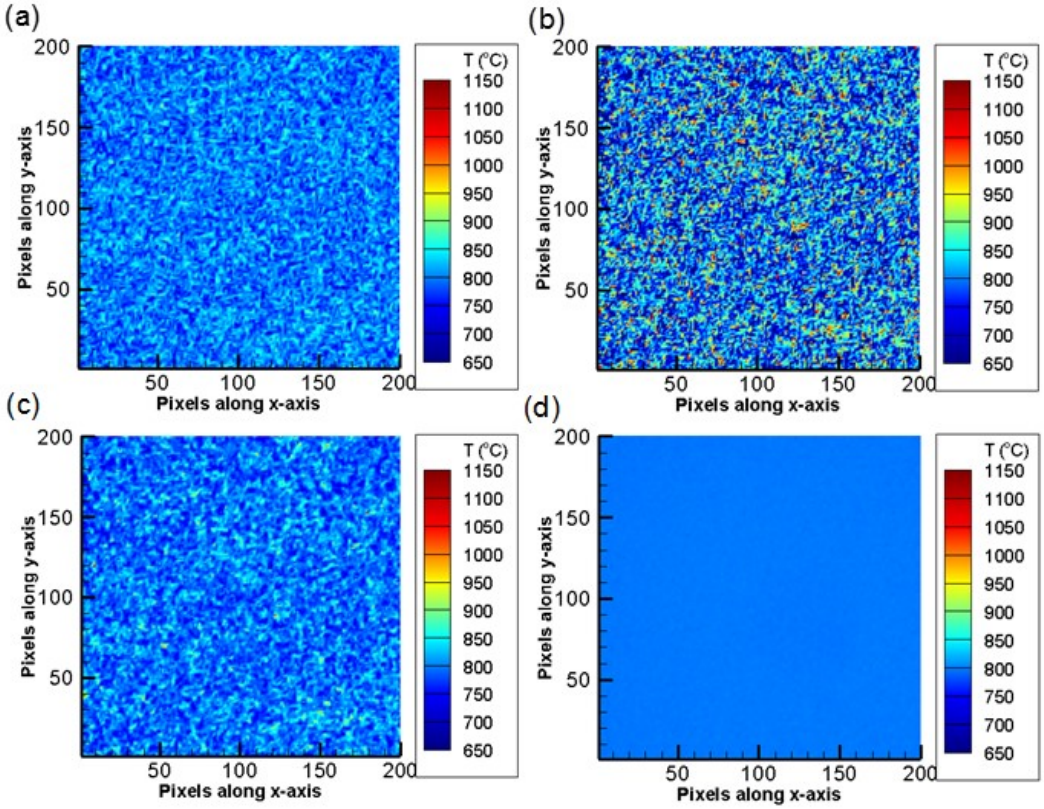

Figure 2-19 Temperature contour plots converted from blackbody images recorded at 800 °C using three normalized intensity ratio curves: (a). G/R; (b). B/R; (c). B/G; and (d). GS.

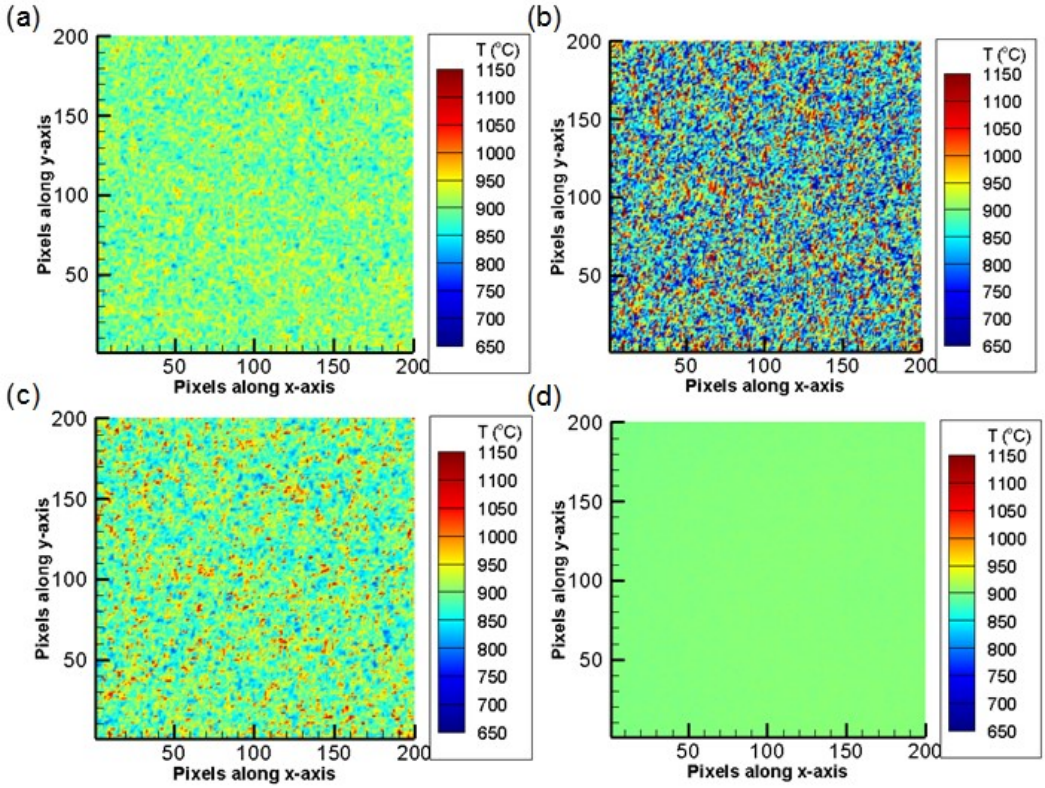

Figure 2-20 Temperature contour plots converted from blackbody images recorded at 900 °C using three normalized intensity ratio curves: (a). G/R; (b). B/R; (c). B/G; and (d). GS.

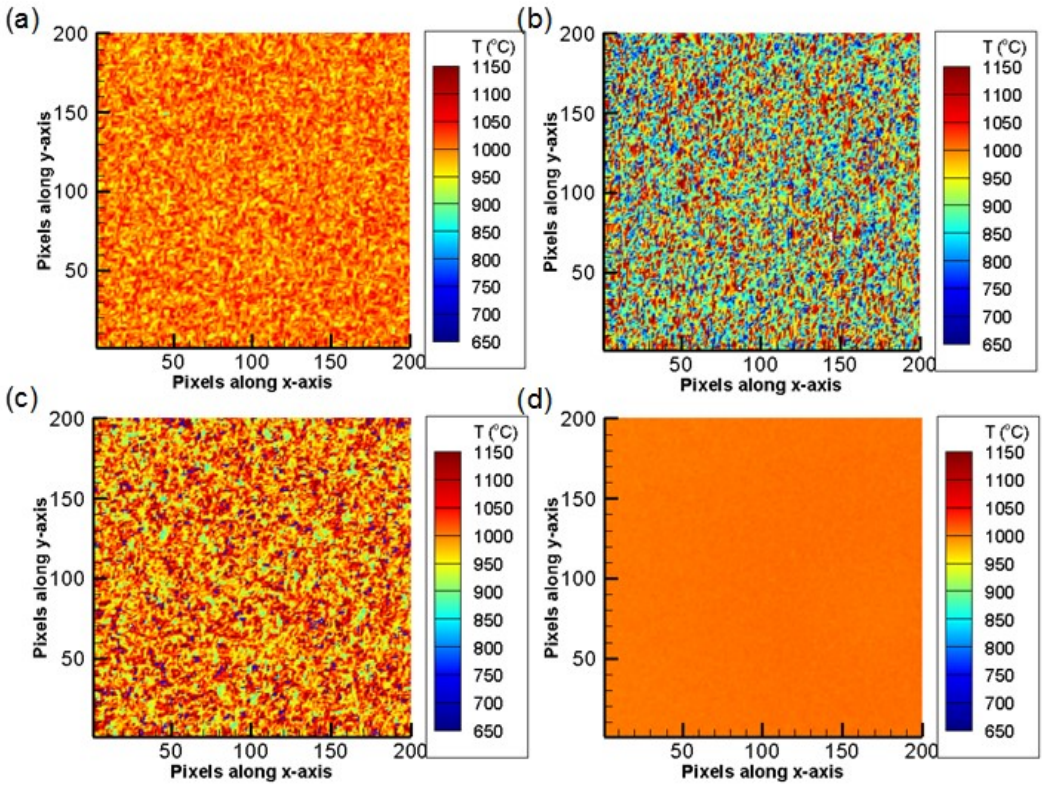

Figure 2-21 Temperature contour plots converted from blackbody images taken at 1000 °C using three normalized intensity ratio curves: (a). G/R; (b). B/R; (c). B/G; and (d). GS.

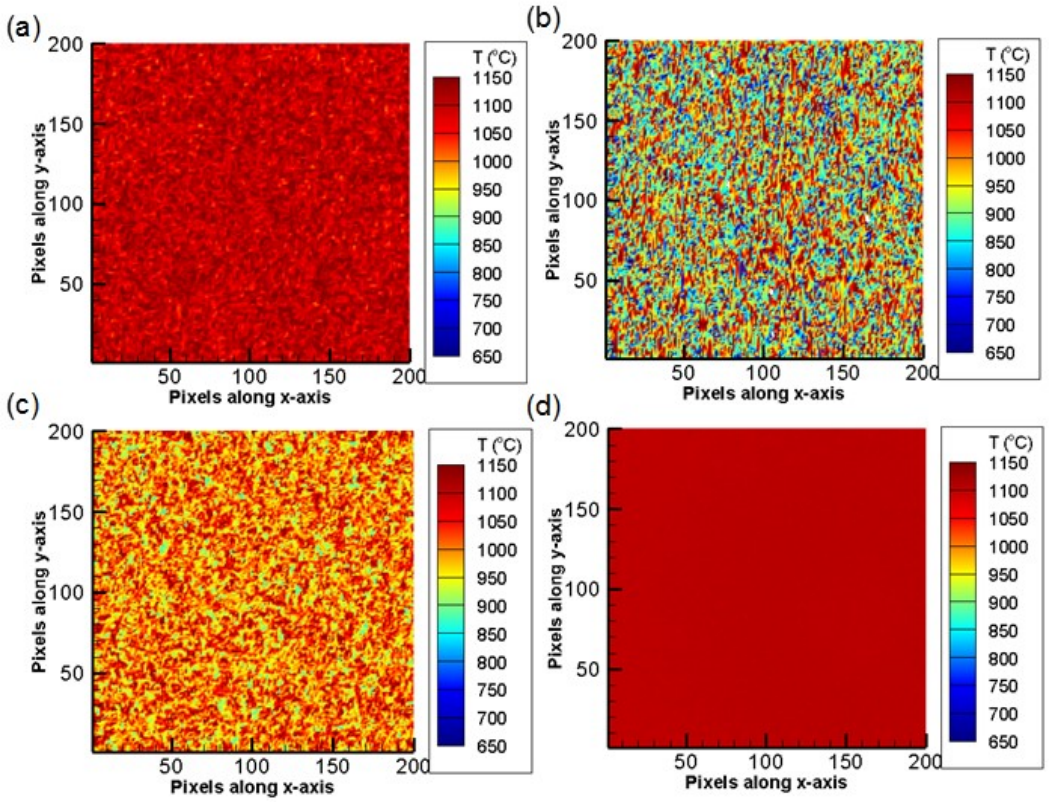

Figure 2-22 Temperature contour plots converted from blackbody images recorded at 1100 °C using three normalized intensity ratio curves: (a). G/R; (b). B/R; (c). B/G; and (d). GS.

2.6 Schott Filters

Some past imaging ratio pyrometer have used Schott filters to reduce the red pixel values. This requires longer exposures to approach saturation. Appropriate exposure time with and without BG 7 and BG 40 filters was studied. Fig. 2-23 represents

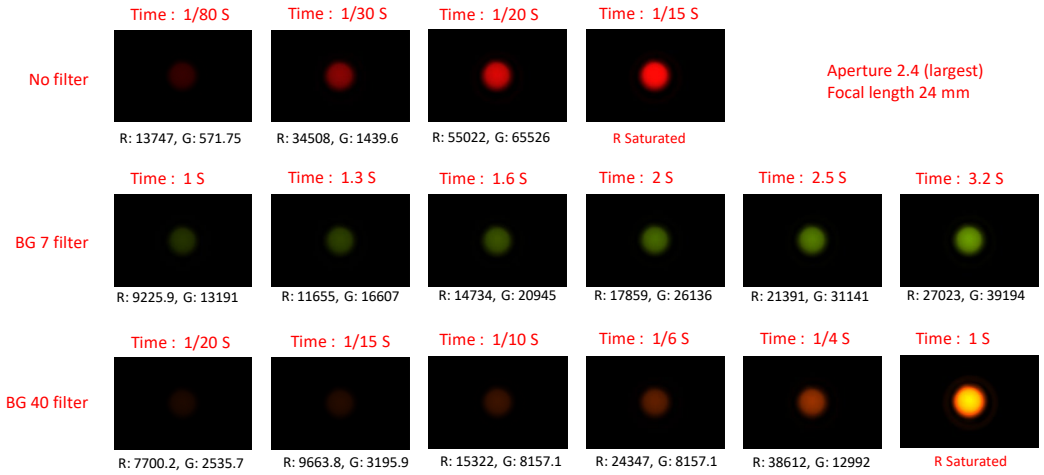

Figure 2-23 Color images of blackbody images at 1000 °C. For this, ISO = 200 and f = 2.4.

blackbody images at 800 °C with varying exposure time. R,G,B signals from 200 × 200 pixel regions centered on the middle of the aperture from each image are plotted with respect to exposure time in Figs. 2-24 – 2-26. Both BG filters maximizes S/N ratios by increasing green signals relative to red, but the cost was an increased exposure time. As described in Fig. 2-23, 3 s was needed to obtain high pixels of green (40000) with BG 7 filters, while the highest pixel of red (about 60000) without filters was obtained with only 0.25 s of exposure time. This was tested with different blackbody temperatures. From images of the blackbody using BG 7 filter at 1000 °C, a factor of 60 increase in exposure time was needed to obtain comparable pixel values.

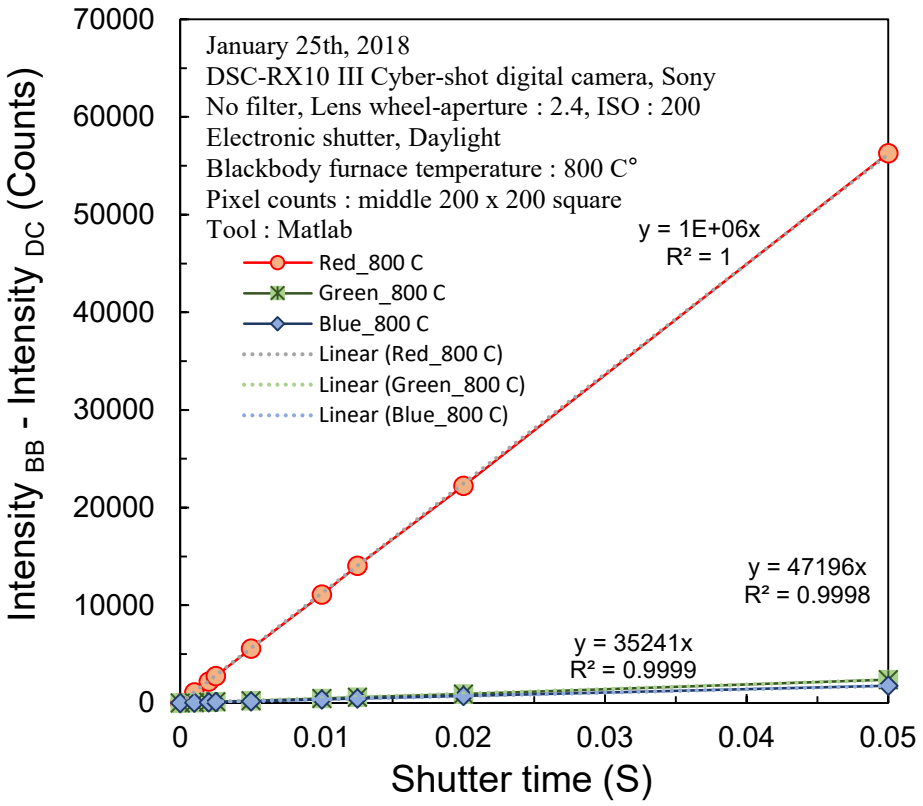

Figure 2-24 Measured pixel values with no filter.

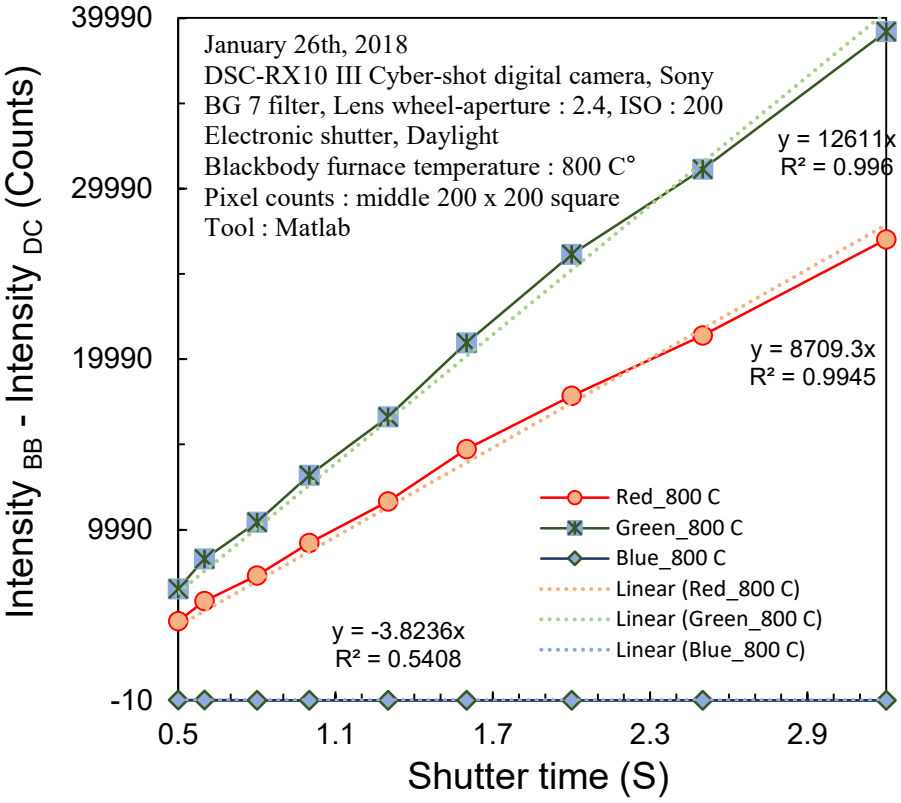

Figure 2-25 Measured pixel values with Schott BG 7 filter.

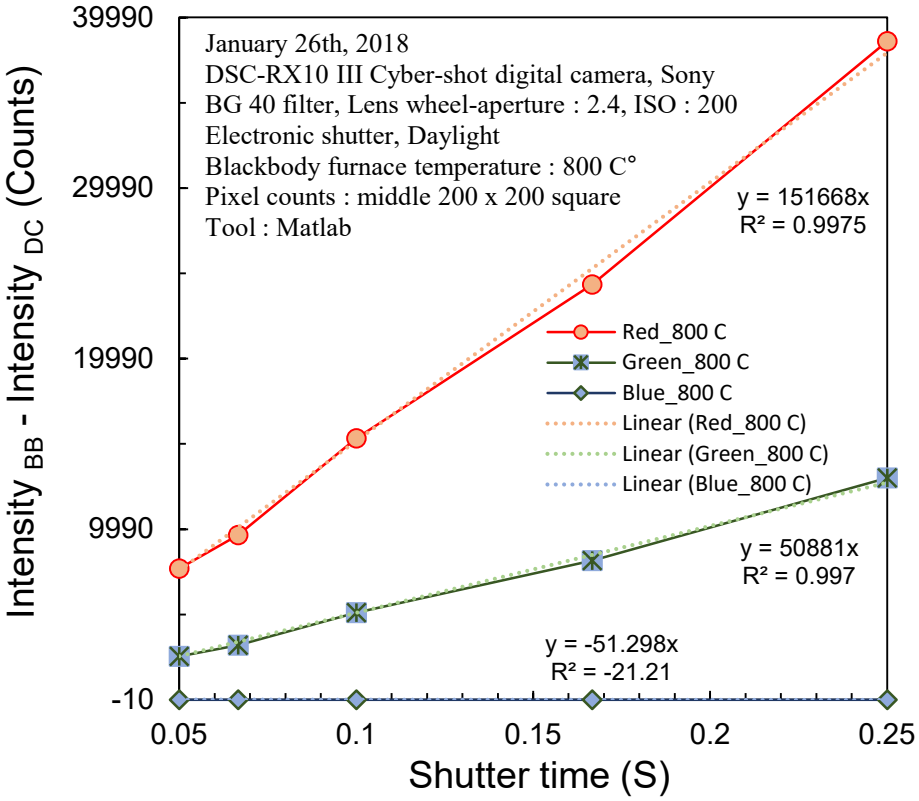

Figure 2-26 Measured pixel values with Schott BG 40 filter.

Chapter 3: Stationary Ember Temperatures

3.1 Introduction

By considering both ratio and grayscale pyrometry for stationary ember temperature measurement, a hybrid pyrometer is identified that incorporates the accuracy of ratio pyrometry and the precision of grayscale pyrometry in this chapter. It also yields the ember emissivity times transmittance in the visible range.

3.2 Experimental

3.2.1 Sample preparation

The fuel was round maple rods, 6.4 mm in diameter (McMaster Carr). These were cut 20 mm long and 3.2 mm axial holes were drilled to promote burning. Maple rods were

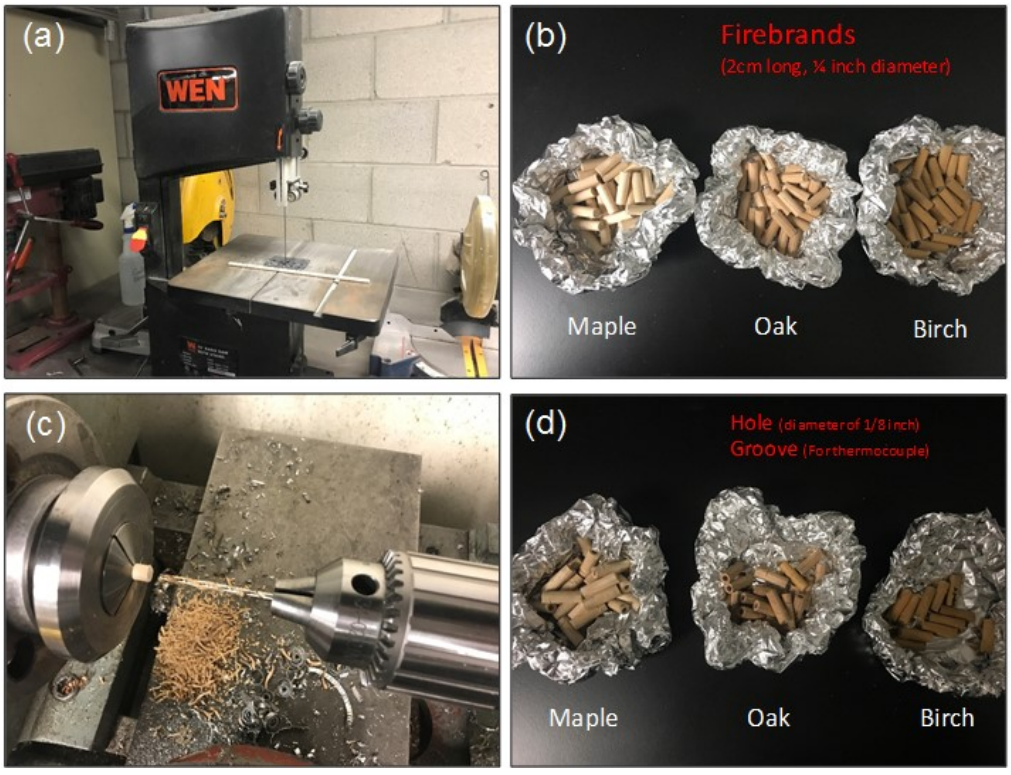

Figure 3-1 Sample preparation of maple, oak, and birch rods. Shown here are: (a). cutting rods into small pieces; (b). preparing rods after cutting; (c). drilling holes along horizontal axis via lathe machining; and (d). preparing rods after drilling.

observed to burn more steadily than oak or birch rods. Prior to ignition the rods were dried for at least 3 hours in an oven at 103 °C [53]. SiC yarn, 0.5 mm in diameter, was inserted into the holes for mounting. No effect of ember cooling by the yarn was detected. The rods were mounted horizontally. The terminal velocity of such a rod (neglecting its hole) with its axis horizontal in air at 25 °C and 1.01 bar is 12 m/s [54].

3.2.2 Ember Generation

Fig. 3-2 represents experiment setup. For some tests a thermocouple was used. For this a circumferential groove with a width of 0.5 mm was cut in the rod. Into the groove was placed a bare-wire K-type thermocouple with a wire diameter of 125 μm. Tension

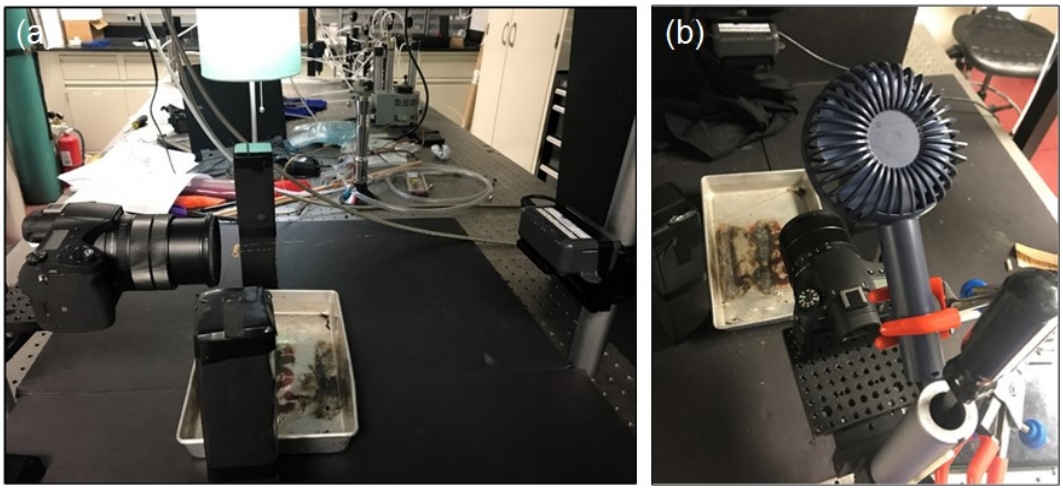

Figure 3-2 Experiment setup. (a). Side view; and (b). top view.

was applied such that the wire maintained good contact with the rod. The thermocouple output was recorded at a sampling rate of 2 kHz. No corrections were made for thermocouple radiation or conduction.

A 50 mm long laminar diffusion flame from a butane lighter was used for ignition. The flame tip impinged on the bottom of the rod, translated back and forth across its

length for 8 s, and was removed. Time zero was defined as the onset of flame impingement.

Figure 3-3 A color image of maple ignition with a gas phase flame.

The ember supported flaming combustion until approximately 35 s. A fan above the camera was activated at 40 s to promote uniform smoldering on the ember surface. The fan discharge was at an angle of 30° below horizontal, producing an air velocity near the firebrand of 2.5 m/s (determined with a handheld rotating vane anemometer.) At approximately 70 s, the rod began to break up and fall from its mount. Little or no smoke was observed. Small amounts of gray ash accumulated on the ember and then fell away.

3.3 Results

3.3.1 Color image of ember

Pyrometry was performed on smoldering embers. For this the camera was mounted with its optical axis horizontal and perpendicular to an ember. The front of the lens was 1 cm from the closest part of the ember and the zoom setting was 11.5 mm. The focus was adjusted to be clear across as much of the ember surface as possible.

An image of a smoldering ember without external illumination is shown in Fig. 3-4a. This was recorded 40 s after ignition. The initial cross section of the ember was a

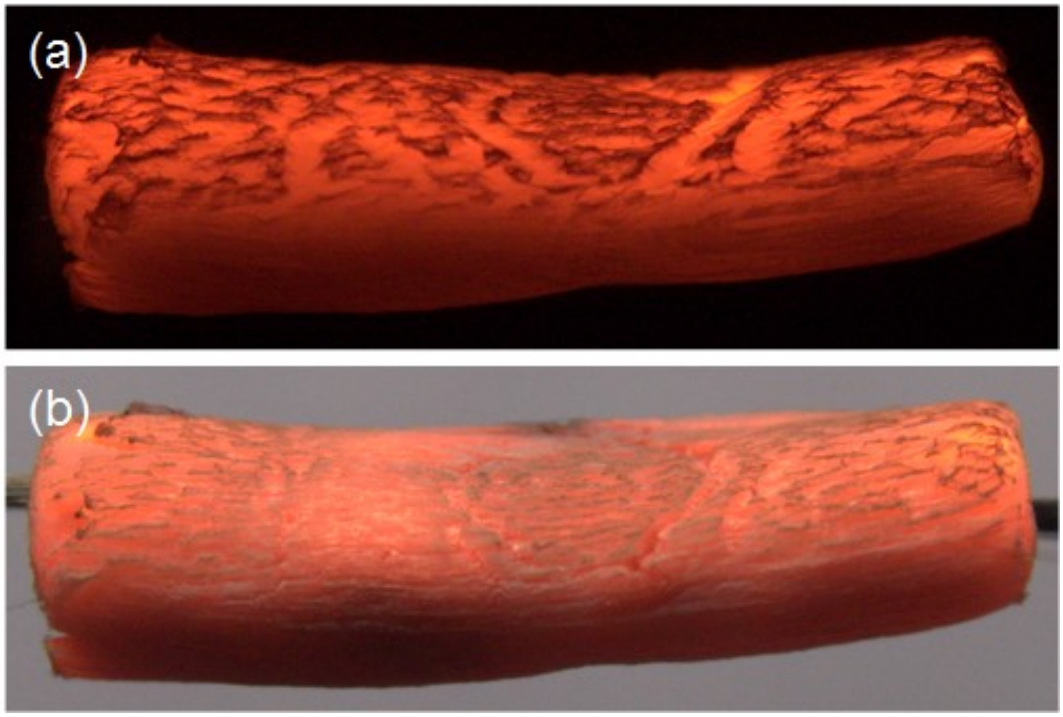

Figure 3-4 Representative color images (1212 × 396 pixels) of a glowing ember (a) with no external illumination; and (b) with a lamp behind the camera. For both images *ISO* = 400, *f* = 2.8, and *t* = 1.56 ms. For improved visualization, some pixels are saturated.

rectangle, but it deformed during burning. The bottom of the ember is relatively dim owing to the downward fan orientation. The top of the ember is mostly orange but has many raised black regions.

The image of Fig. 3-4b was recorded 6 s earlier with a lamp behind the camera. This illumination changes the black regions to light gray, indicating they are ash. This identification of ash was confirmed by scratching ember surfaces with a small blade, whereby gray ash fell away, and the black regions became orange.

3.3.2 Ember pyrometry

For ember pyrometry, images similar to Fig. 3-4a were recorded with dimmer exposures such that the pixel values were as high as possible without saturation at any pixel in any color plane. One such image is shown in Fig. 3-5a. The size of each pixel in the object plane is 17 μm. The thermocouple (TC) is visible as the dark vertical band and its bead location is indicated in Fig. 3-5a.

Intensities of red, green, and blue color planes from the glowing ember of the image in Fig. 3-5a were examined to ensure they were free from saturation, as shown in Fig. 3-6. Intensity contour plots for each component were created in Tecplot. It was confirmed that the brightest pixels in red plane were not saturated but were close to saturation. However, green and blue contour plots show some pixels were lost. This indicates that color ratio pyrometry has a reduced signal-to-noise ratio compared to grayscale pyrometry and B/R and B/G ratios are of little or no value.

For ratio pyrometry, NI_G / NI_R was found for each pixel in Fig. 3-5a. These were converted to temperatures using the curve fit of Fig. 2-13, a 3rd order best-fit polynomial of T in terms of log(NI_G / NI_R). A null temperature was assigned to every pixel that was outside the ember, had a green pixel value below 100, and/or was outside the range of 600 – 1200 °C. Owing to scatter, spatial smoothing was performed. For this, each pixel was assigned the mean temperature of the unsmoothed temperatures of

the 7 × 7 pixel region centered on it. Pixels with a null temperature were excluded from

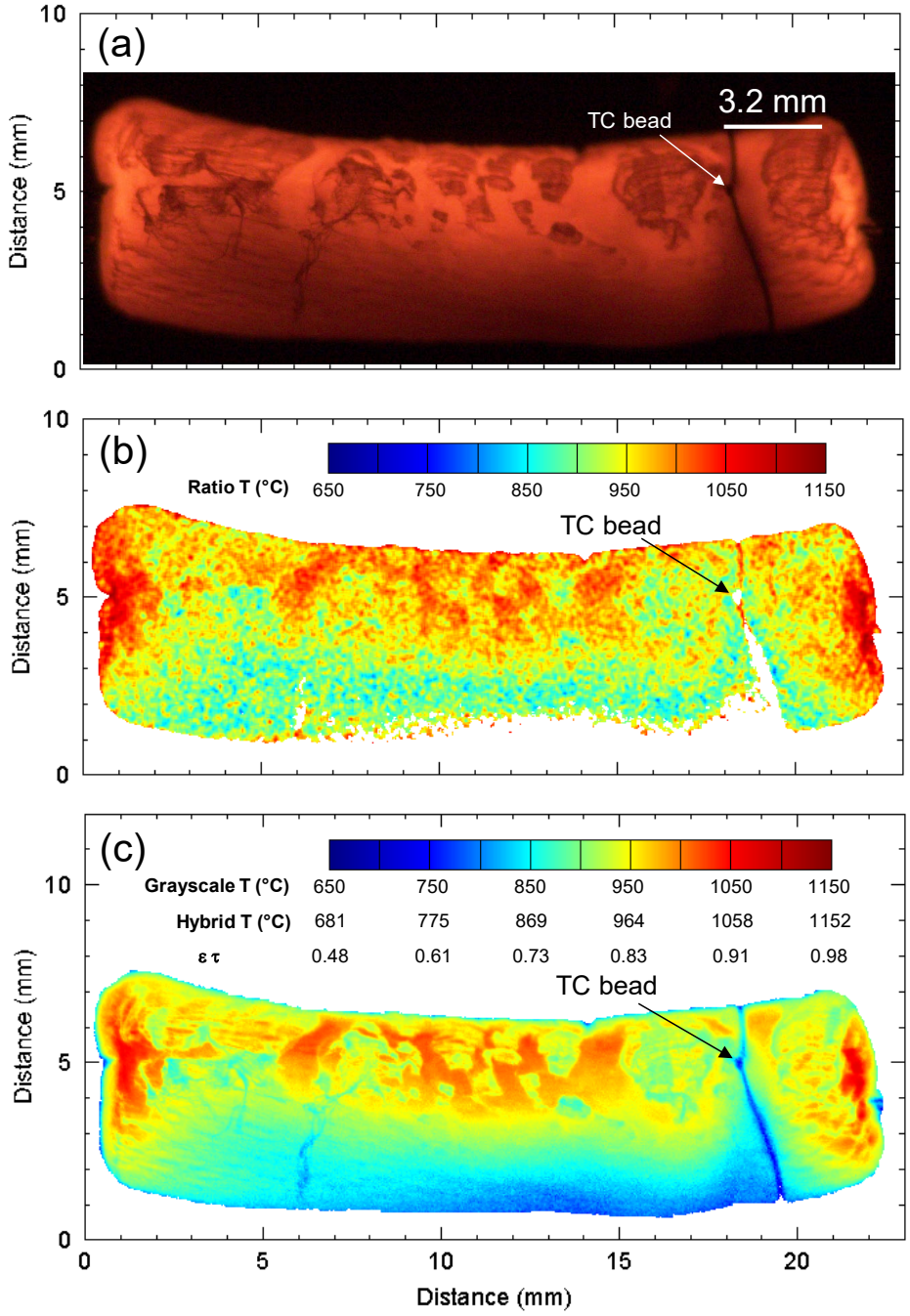

Figure 3-5 (a) Representative color image (1200 × 432 pixels) of a smoldering ember at 50 s. For this image ISO = 200, f = 2.8, and t = 1.3 ms. Figure (b) is the resulting color contour plot of ratio pyrometry temperatures. Figure (c) is the resulting color contour plot of: grayscale pyrometry temperatures, hybrid pyrometry temperatures, and visible emissivity.

this mean. If more than 50% of these 49 pixels had null temperatures, the smoothed center pixel was assigned a null temperature.

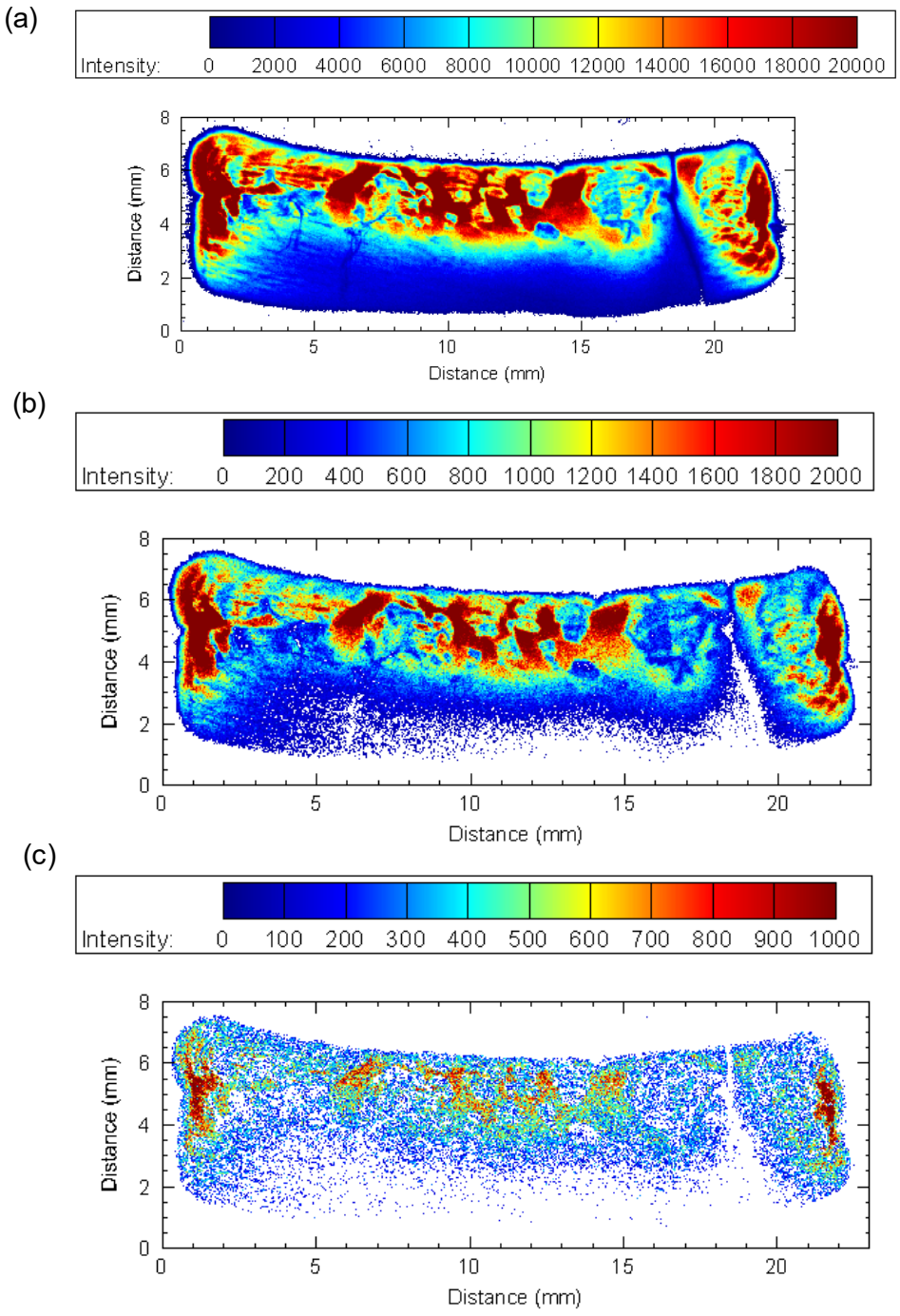

Figure 3-6 Signal loss from (a). red; (b). green; and (c). blue.

Fig. 3-5b shows the ratio pyrometry results. The hottest regions correspond to the orange regions in Fig. 3-5a. The coolest are near the ember bottom, where air velocities are low. The ends of the embers are hot owing to low heat conduction into the unburned wood. The black regions surrounded by orange, identified above as ash, are cool because the ash slows the transport of oxygen and products.

For grayscale pyrometry, NI_{GS} was found for each pixel in Fig. 3-5a. These were converted to temperatures using the curve fit of Fig. 2-12, a 2nd order best-fit polynomial of T in terms of log(NI_{GS}). A null temperature was assigned to every pixel that was outside the ember or within 6 pixels of the ember edge. No pixel within the ember was outside the range of 600 – 1200 °C. No spatial smoothing was applied. Figure 4c, with its first legend line, shows the grayscale pyrometry results.

Figure 3-5c shows the grayscale pyrometry results. Compared to the ratio pyrometry results these temperatures are far less scattered. This is despite 7 × 7 pixel spatial smoothing in the ratio pyrometry and no spatial smoothing in the grayscale pyrometry.

Grayscale pyrometry indicates lower temperatures than ratio pyrometry at most locations. The ratio pyrometer is immune from interference of nonunity emissivity times ash transmittance ($\varepsilon\tau$) when $\varepsilon\tau$ is the same for the R and G pixel wavelengths. The grayscale pyrometer has no such immunity, as it interprets decreased GS pixel values as decreased temperatures.

This was investigated by comparing the mean temperatures of 30 × 30 pixel regions that were nearly isothermal for both methods. Several ember images were analyzed, using different wind velocities from 0 – 7 m/s, and the results are plotted in Fig. 3-7.

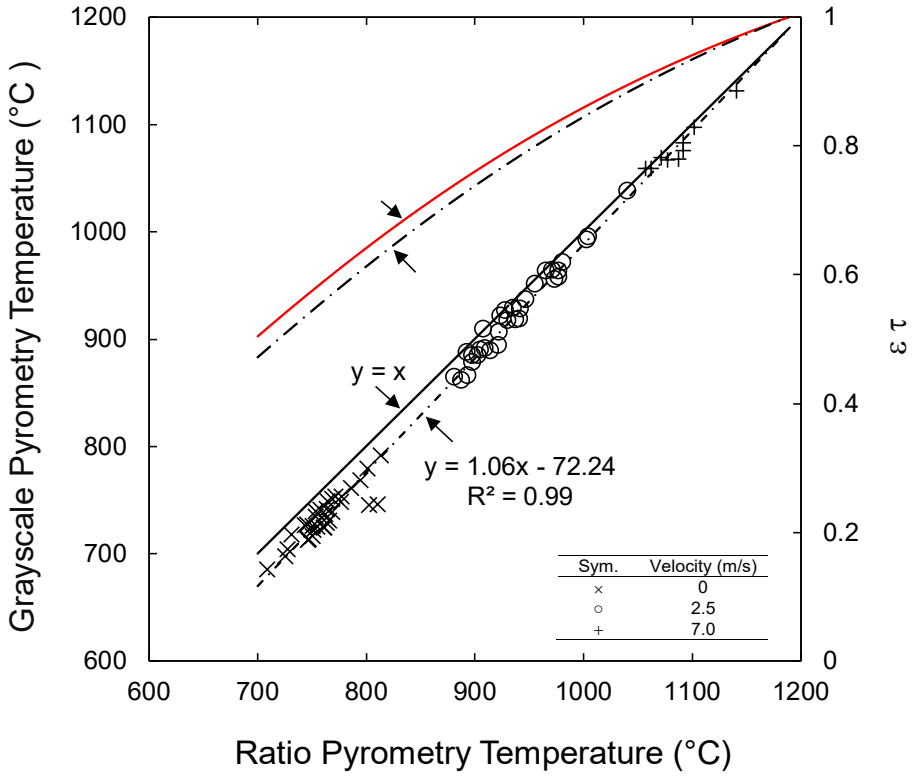

Figure 3-7 Grayscale pyrometry temperature and visible emissivity plotted with respect to ratio pyrometry temperature for smoldering embers. For the 7 m/s tests the ratio pyrometry correlation was extrapolated to 1300 °C.

The mean pyrometry temperature and emissivity times ash transmittance from 73 isothermal regions were investigated. Details are described in Appendix B. These data include images captured without and with the fan activation (leading to 2.5 m/s of velocity) and with higher velocity of air supply (7 m/s). Airborne firebrands typically move at their terminal velocity [15]. The terminal velocity of the cylindrical maple rods (assuming no hole inside) with its axis horizontal in air at 25 °C and 1.01 bar was 12 m/s [54]. This is close to the 7 – 8 m/s terminal velocities measured by Tarifa et al [15] using similar size of cylindrical firebrands.

The measurements in Fig. 3-7 are well correlated with the line fit shown. This line allows the grayscale pyrometry temperatures, with their low noise, to be corrected upward to match the ratio pyrometry results, with their resilience against nonunity emissivity, ash, and smoke. This correction is called hybrid pyrometry. The fit shown in Fig. 3-7 yields

$$T_{hybrid} = (T_{GS} + 72.24\ °C) / 1.06 , \quad (3\text{-}1)$$

where T_{hybrid} is the temperature from hybrid pyrometry. For the ember of Fig. 4a, the hybrid pyrometry results are shown in Fig. 4c using the second legend.

Figure 3-8 shows the probability distribution function (pdf) of the hybrid temperatures of Fig. 3-5c. Its shape is similar to pdfs of smoldering coal [37]. The mean

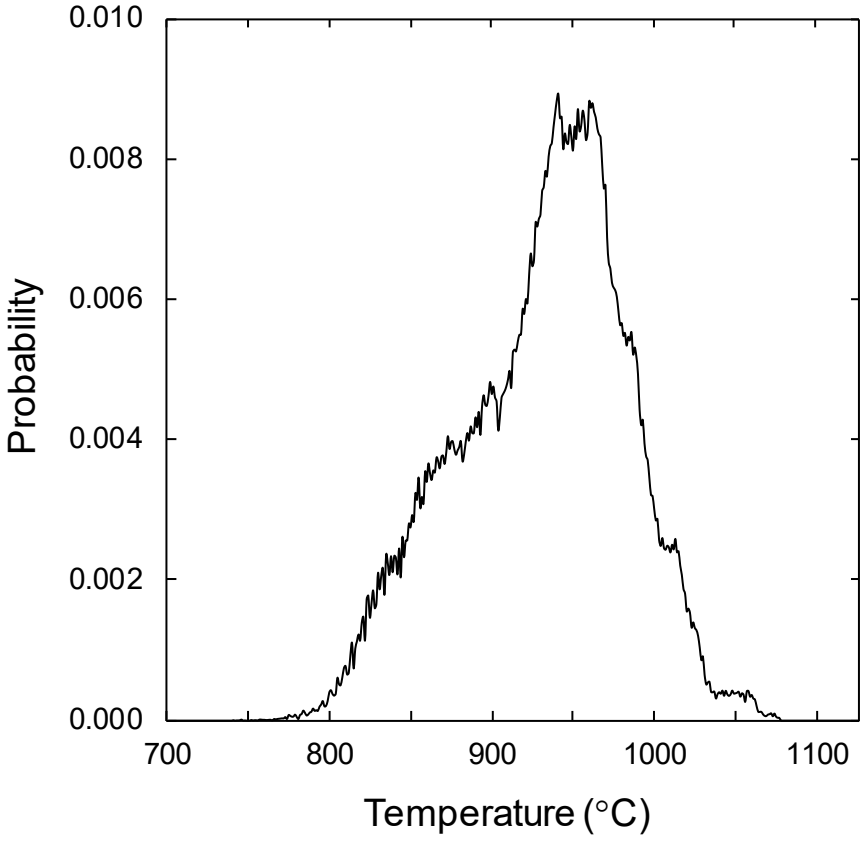

Figure 3-8 PDF of the temperature of the ember in Fig. 3-5c using hybrid pyrometry. The bin width was 1 °C.

temperature was 930 °C, and the standard deviation was 52 °C. The minimum and maximum temperatures (excluding the 20 coolest and 20 hottest pixels) were 750 and 1070 °C.

3.3.3 Visible emissivity times transmittance

The transmittance in the visible of a thin layer of ash on these embers can be estimated from this form of the Lambert-Beer Law,

$$\tau = \exp (- k_p \rho \, Y \, L) , \tag{3-2}$$

where k_p is the ash mass extinction coefficient, L is the ash layer thickness, Y is the mass of ash per mass of wood burned, and ρ is the virgin wood density. Reference [55] reports k_p = 0.229 m^2/g for coal ash in the visible. The measured density of the maple rods is 746 kg/m^3. Quantity Y for wood is estimated from Table 1 of Ref. [56] to be 5.8E-3. The ember images of Fig. 3-4 indicate an ash layer thickness of 0 – 0.3 mm. Inserting these values into Eq. (3-2) predicts a range of τ of 0.74 – 1 as shown in Fig. 3-9. The uncertainties on this estimate are large owing to uncertainties in k_p and L.

Although smoke was occasionally seen above the embers, none was observed between the embers and the camera. Because both ash-free regions, with unity τ, and ash-covered regions follow the same correlation in Fig. 3-7, it is possible that the minimum τ of 0.74 estimated above is too low and that τ is nearly unity for this ember.

As shown in Fig. 3-10, two different scenarios were considered for visible ember emissivity. For a smoldering ember with emissivity ε and with emission passing through ash and/or smoke with transmissivity Tr, the resulting spectral emissive power is

$$E_\lambda = \varepsilon \, Tr \, E_{\lambda b} , \tag{3-3}$$

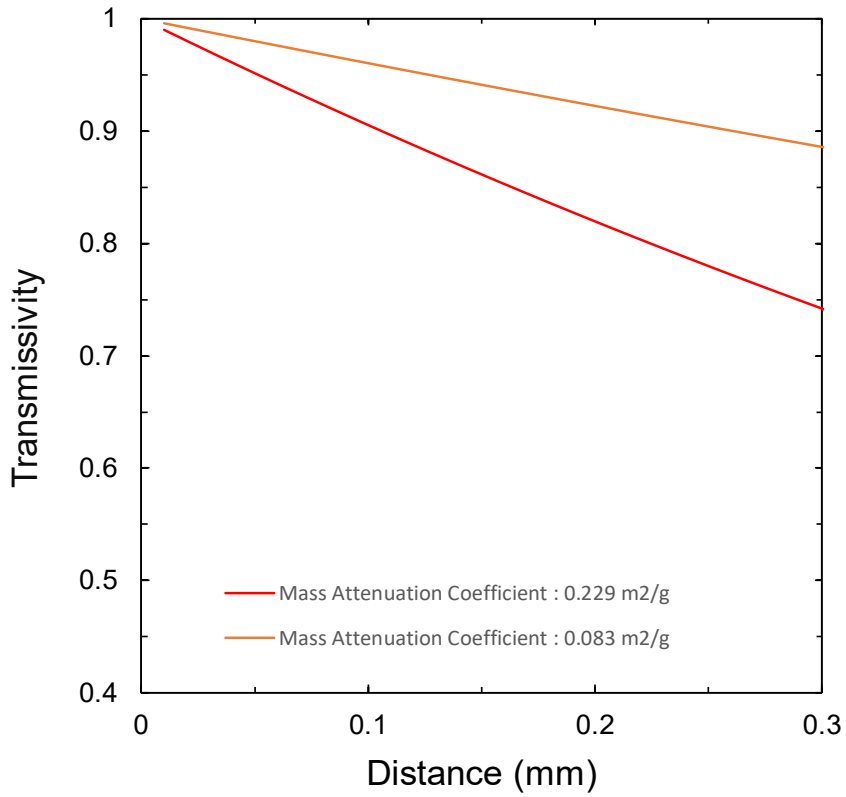

Figure 3-9 Estimated transmissivity of ashes and smoke.

where $E_{\lambda b}$ is given by Eq. (2-3) and where E_λ, Tr, and ε pertain to the wavelengths imaged by the camera. Assuming the product $\varepsilon\,\tau$ is the same for the wavelengths recorded by the R and G pixels, the temperature indicated by ratio pyrometry, T_{ratio}, is the true temperature of the ember below the ash. The temperature indicated by grayscale pyrometry, T_{GS}, predicated on $\varepsilon = Tr = 1$, is the temperature of a blackbody with the same spectral emissive power. Evaluating Eq. (3-3) at T_{ratio} and Eq. (2-3) at T_{GS} and equating them allows the product $\varepsilon\,Tr$ to be determined from

$$\varepsilon\,Tr = \exp\left[- C_2 / \lambda \left(T_{GS}^{-1} - T_{ratio}^{-1} \right) \right] . \qquad (3\text{-}4)$$

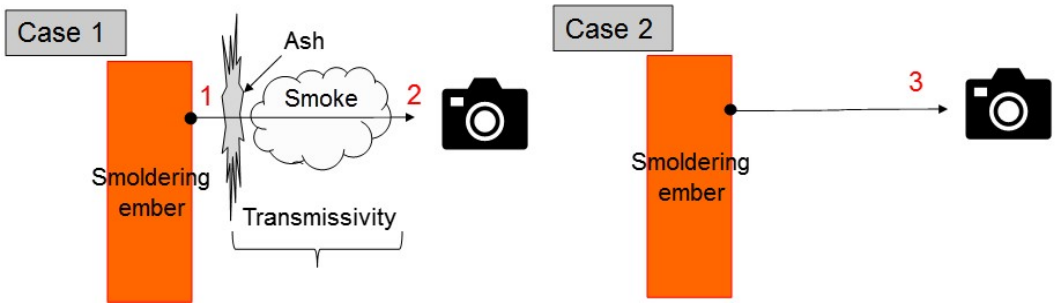

Figure 3-10 Two different scenarios.

Eq. (3-4), combined with the linear relationship between T_{GS} and T_{ratio} in Fig. 3-7, allows ε times τ to be plotted with respect to T_{ratio} in Fig. 3-7. This curve increases with temperature. This is consistent with past work, which found emissivity to increase with metal temperature [43] and with ember burn time [28].

Because the red pixel values are the highest, the 680 nm curve is the best estimate of the ember emissivity in the visible. This curve is used to convert T_{hybrid} to visible emissivity, with the results shown in Fig. 3-5c using the third legend. This ember has a mean visible emissivity of 0.73, which is similar to the ember emissivity of 0.6 reported by Ref. [21].

For a more rigorous version of Eq. (3-4), the camera sensitivity should be considered. Typical color CMOS and charged-couple device (CCD) cameras are sensitive to wavelengths between 450 – 650 nm [28,41,45,51]. A camera sensitivity can be defined as

$$S = NI / E, \tag{3-5}$$

where NI and E are the intensity and the light energy at single wavelength. Eqs. (2-3) and (3-3) can be substituted into the total emissive powers of blackbody and the

smoldering ember with limit 0 to infinite, respectively. For example, the total emissive power of the smoldering is described in Eq. (8).

$$E = \int_0^{\infty} E_{\lambda}\, d\lambda, \tag{3-6}$$

where E in this case is the total emissive power, and E_{λ} is spectral emissive power of the smoldering ember. Hence, evaluating the total emissivity power of the smoldering at T_{ratio} and the blackbody at T_{GS} using Eq. (3-6) combining into Eq. (3-5), and Eq. (3-7) and Eq. (3-8) can be derived as

$$E_{GS} = \int_{450\ \mathrm{nm}}^{650\ \mathrm{nm}} S(\lambda)\, E_{\lambda b}\,(\,T_{GS}\,)\,\mathrm{d}\lambda., \tag{3-7}$$

$$E_{ratio} = \int_{450\ \mathrm{nm}}^{650\ \mathrm{nm}} S(\lambda)\ \varepsilon\,\tau\, E_{\lambda b}\,(\,T_{ratio})\,\mathrm{d}\lambda., \tag{3-8}$$

where E_{GS} and E_{ratio} are the total emissivity power of the blackbody and the smoldering ember. Equating Eq. (3-7), and Eq. (3-8) allows the product $\varepsilon\,\tau$ to be determined from

$$\varepsilon\,\tau \int_{450\ \mathrm{nm}}^{650\ \mathrm{nm}} S(\lambda)\, E_{\lambda b}\,(\,T_{ratio}\,)\,\mathrm{d}\lambda = \int_{450\ \mathrm{nm}}^{650\ \mathrm{nm}} S(\lambda)\, E_{\lambda b}\,(\,T_{GS}\,)\,\mathrm{d}\lambda\,. \tag{3-9}$$

Assuming the camera sensitivity is constant in the given wavelength range, Eq. (3-9) can be simplified as

$$\varepsilon\,\tau = \int_{450\ \mathrm{nm}}^{650\ \mathrm{nm}} E_{\lambda b}\,(\,T_{GS}\,)\,\mathrm{d}\lambda \,/\, \int_{450\ \mathrm{nm}}^{650\ \mathrm{nm}} E_{\lambda b}\,(\,T_{ratio}\,)\,\mathrm{d}\lambda\,. \tag{3-10}$$

Equation (3-10), combined with the linear relationship between T_{GS} and T_{ratio} in Fig. 3-7, allows ε times τ to be plotted with respect to T_{ratio} with a black dash line in Fig. 3-7. This curve was slightly shifted from the 680 nm curve. This ember has a mean visible emissivity of 0.71.

3.3.4 Thermocouple results

The thermocouple temperatures for the test of Fig. 3-5 are plotted in Fig. 3-11. When Fig. 3-5a was recorded this temperature was 695 °C, which is over 200 °C lower than the mean ember temperature. This is a concern for past work that relied on thermocouples to measure ember temperatures of 220 – 850 °C [21,25].

Grayscale and hybrid pyrometry indicated the thermocouple bead temperature to be 757 and 781 °C as shown in Fig. 3-12 and Fig. 3-13. For measuring GS and hybrid temperatures in thermocouple bead region (white cells), a 3 × 3 pixel region centered

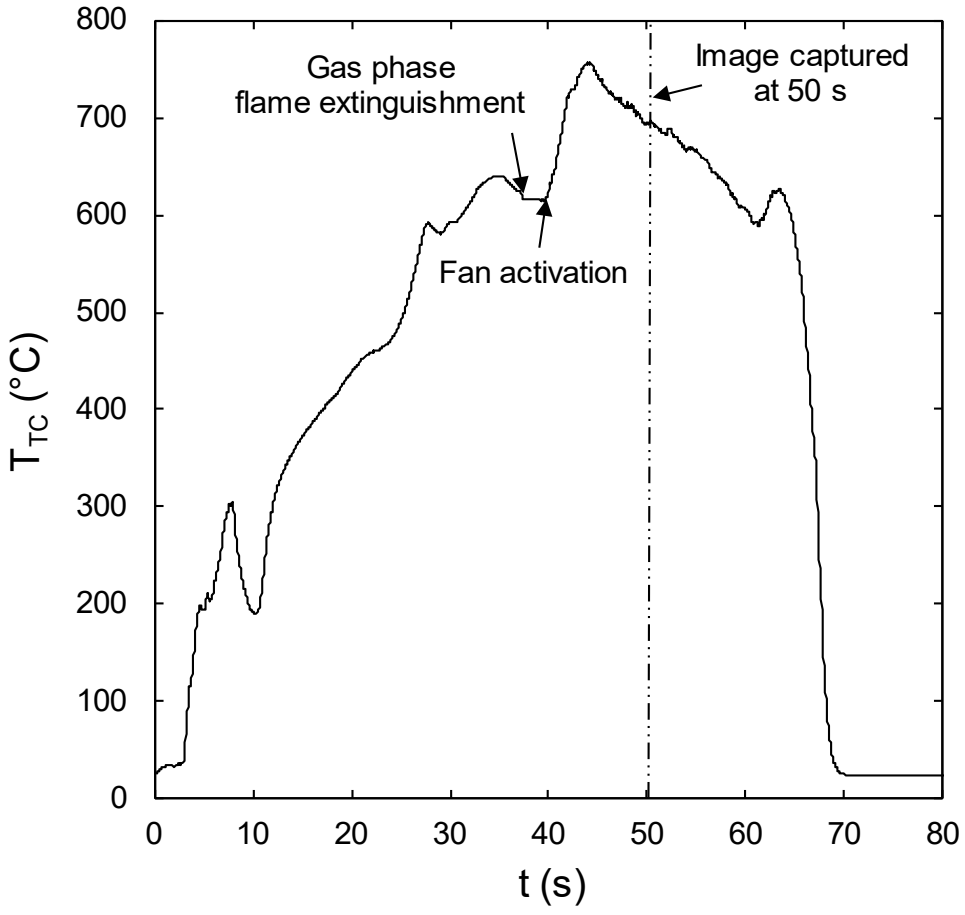

Figure 3-11 Thermocouple temperature plotted with respect to time. The temperature was 695 °C at 50 s.

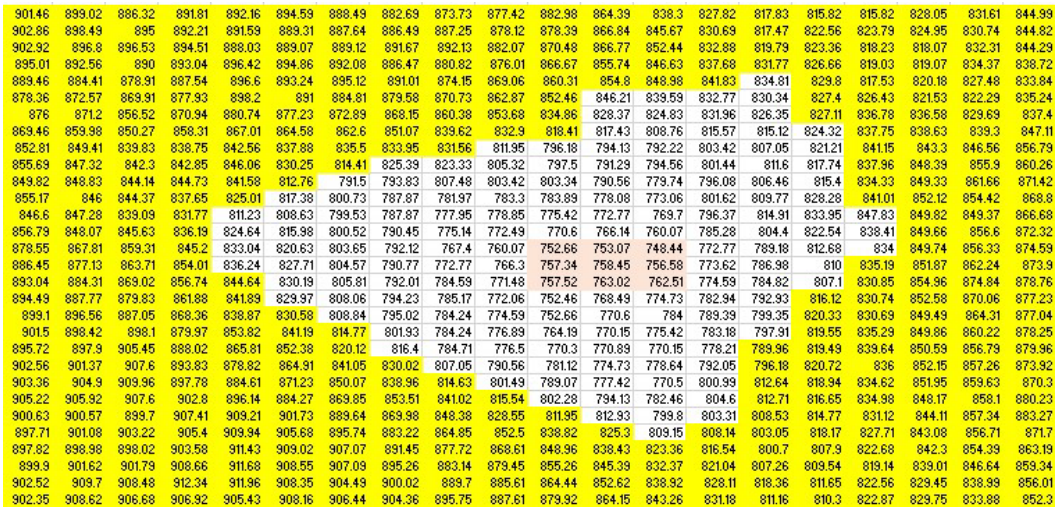

Figure 3-12 Grayscale temperatures in thermocouple bead region.

on the middle of the thermocouple bead was selected. Grayscale pyrometry indicates the thermocouple bead temperatures to be 757 ± 4.2°C. Hybrid pyrometry indicates the thermocouple bead temperatures to be 781 ± 4.2°C. These temperatures are higher

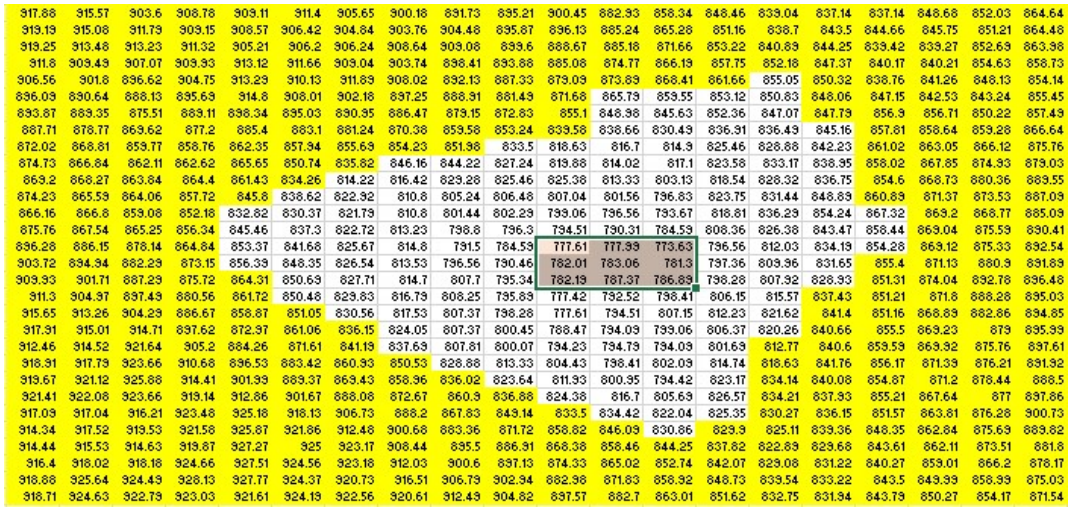

Figure 3-13 Hybrid temperatures in thermocouple bead region.

owing to imperfect imaging of the small bead. Hybrid pyrometry indicated a temperature of the smolder region near the bead of 860 °C. Fig. 3-5b and 3-5c show that the thermocouple causes significant smolder quenching. Additionally, the

thermocouple bead is cooler than the adjacent ember owing to imperfect thermal contact.

3.3.5 Uncertainty of ember temperature

Owing to less uniform temperatures and uncertainties in emissivity times transmittance, for smoldering embers the uncertainty in T_{hybrid} at any pixel is estimated at ±20 °C. Fig. 3-14 supports estimated uncertainties of ember temperature, which

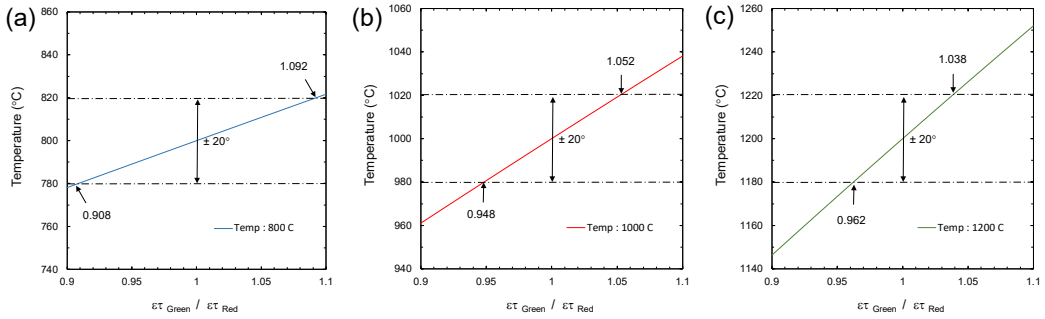

Figure 3-14 Uncertainty of G/R ratio pyrometry function for temperature difference at (a). 800 °C; (b). 1000 °C; and (c). 1200 °C.

shows that measured ratio pyrometry temperatures change depending on ratios of emissivity times transmittance of green to red signals from camera detectors at fixed temperatures. The estimated uncertainty for $\varepsilon\tau$ is ±10%.

It is of interest to consider whether this pyrometer can be applied with similar uncertainty to embers of other materials and shapes and/or in environments with different compositions and flow fields. The main limitations are that the ember temperatures should be within the range of the blackbody furnace calibration: 600 – 1200 °C, and the ember emissivity times transmittance should be constant for the wavelengths recorded by the camera.

3.3.6 Tests in a fluorescent light versus sunlight

Tests were conducted in sunlight and with a fluorescent bulb light. Fig. 3-15 is a color image of a smoldering ember in daylight with ISO = 200, f/3.2, and t = 1.6 ms. As shown in Fig. 3-16, the daylight disrupts pyrometry. With the lights on, the embers

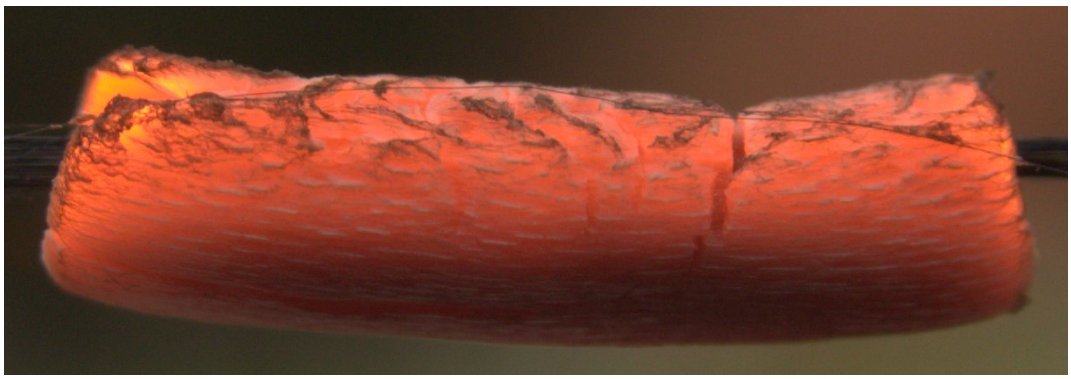

Figure 3-15 A representative color image of a glowing ember with sunlight.

become gray, and red, green, and blue have similar values as shown in Figure 3-15. Hence, comparing the red, green, and blue values for the same ember in many lighting situations will be required to decide how to correct these to representative dark environment signals in the future. Subtraction based upon a method that considers the colors of nearby objects may be required. It was found that the test results were not significantly affected by the fluorescent bulb light as described in Figure 3-17.

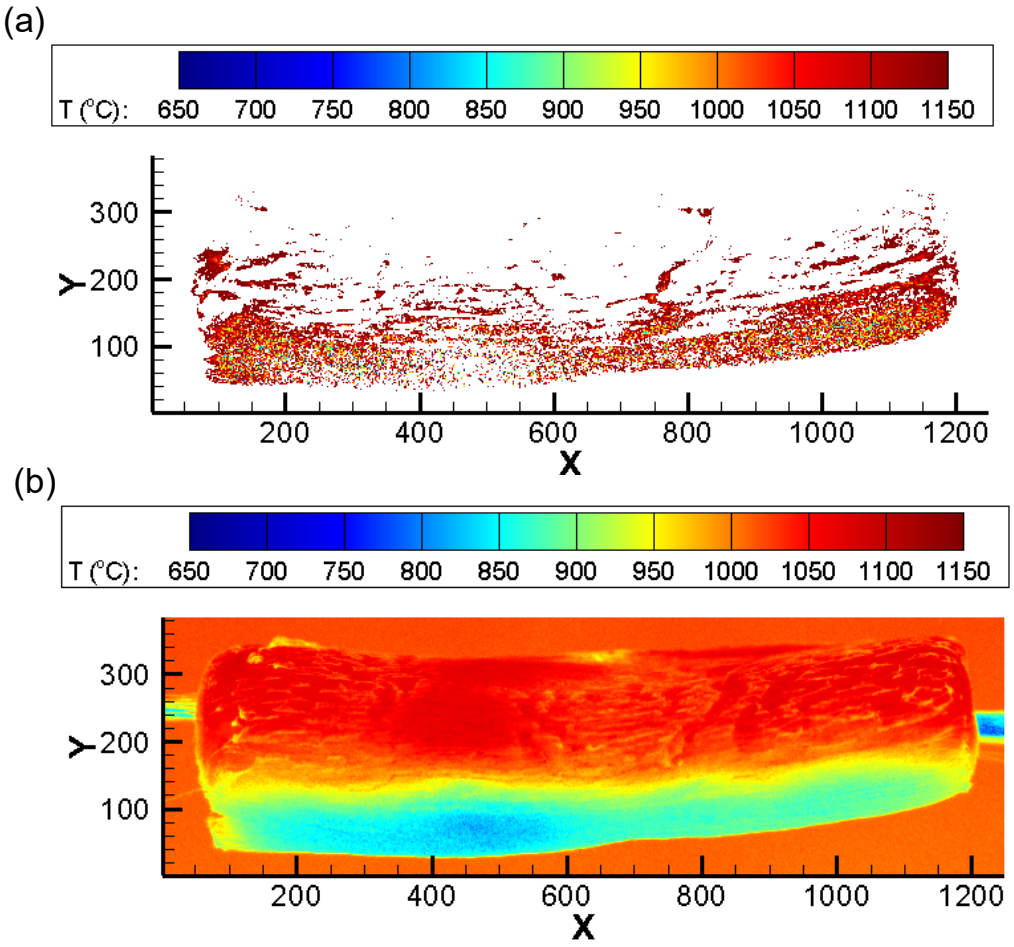

Figure 3-16 Figure (a) and Figure (b) are the resulting color contour plots of ratio pyrometry temperatures and grayscale pyrometry temperatures from a smoldering ember in sunlight.

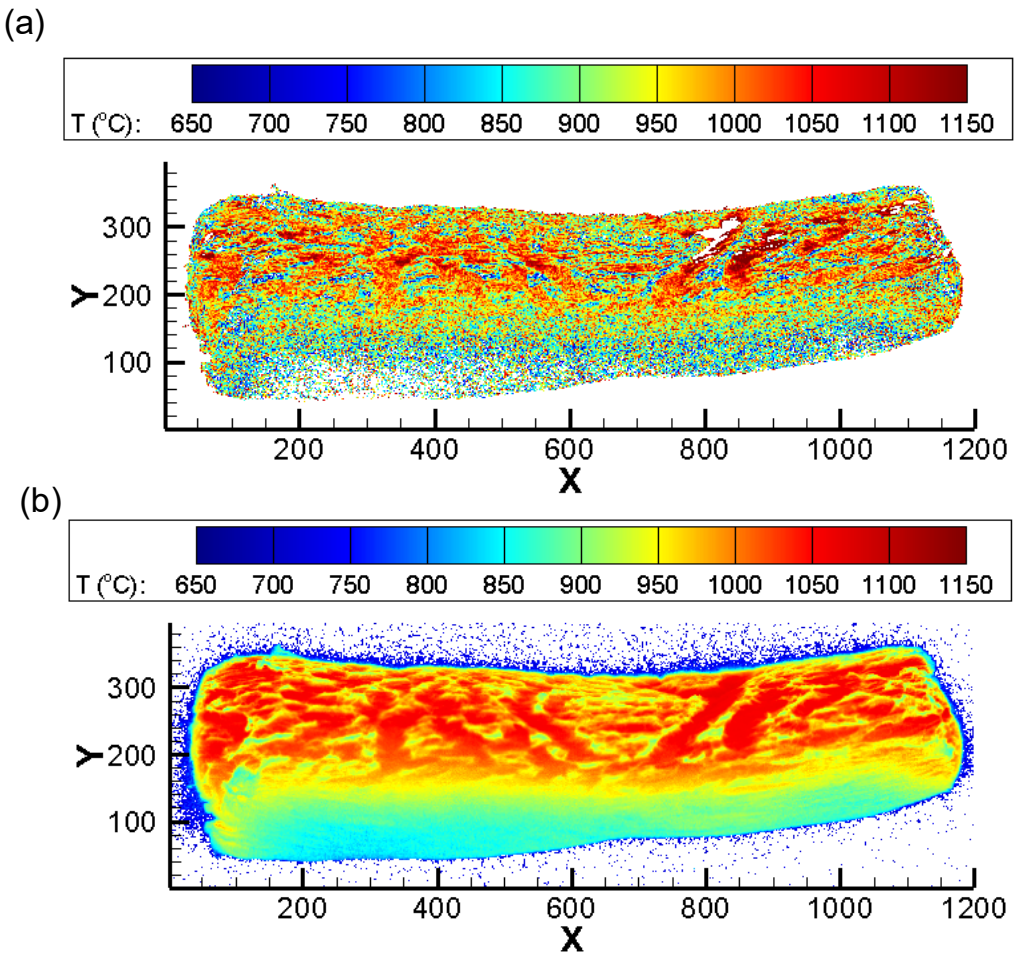

Figure 3-17 Figure (a) and Figure (b) are the resulting color contour plots of ratio pyrometry temperatures and grayscale pyrometry temperatures from a smoldering ember in fluorescent bulb light in the laboratory.

Chapter 4: Pendulum Firebrand Temperatures

4.1 Introduction

In a real fire scenario, many wind-driven firebrands (called firebrand showers), attack materials and structures. These airborne firebrands can have different temperatures and temperatures that vary with time. It has been challenging to measure airborne firebrand temperatures in real fire scenarios.

Here pendulum firebrands that emulate airborne firebrands are observed and their temperatures are measured with pyrometry. Quantitative correlations between firebrand temperature and velocity were studied.

4.2 Experimental

4.2.1 Sample preparation

The fuel was the same maple rod that was used for the stationary ember in Chapter 3. Round maple rods with a diameter of 6.4 mm (McMaster Carr) with 3.2 mm axial holes were selected. Those were put in the oven at 103 °C to eliminate moisture [53].

Fig. 4-1 represents the pendulum experimental apparatus. For the pendulum rod, a C360 brass solid round rod of 12.7 mm diameter (Chase Brass and Copper Company, 0500RD03) was selected because brass is easily machinable. The rod length was 50 cm. The mass of the rod was distributed along its length. The maple rod ends were held with a tweezer. The pendulum pivot was a bearing with negligible friction.

For camera triggering, Imaging Edge software from SONY was used. Images were recorded in raw format.

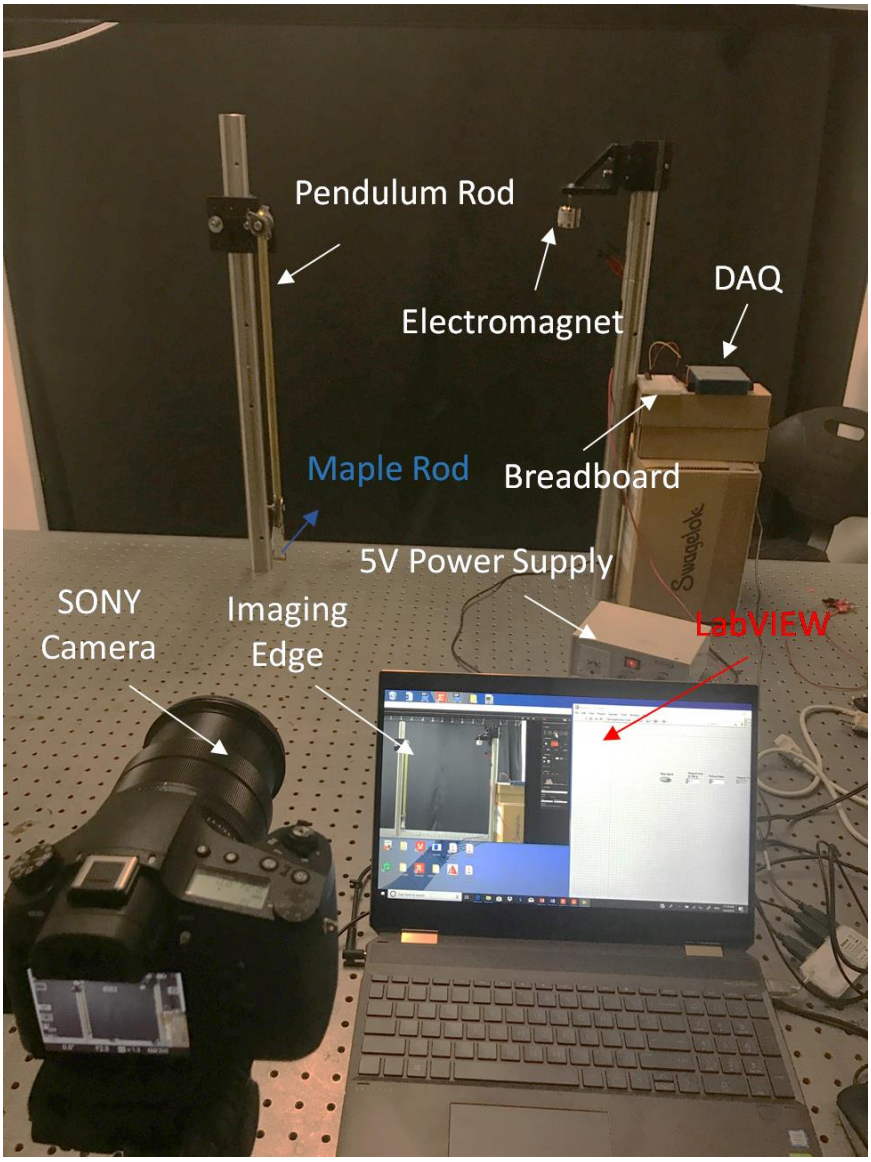

Figure 4-1 Experiment setup.

To release the rod consistently, a 5 VDC electromagnet solenoid was used as shown in Fig. 4-1. The solenoid was controlled by a data acquisition system, DAQ (National Instruments, NI USB-6003) connected to a reed relay, shown in Fig. 4-2.

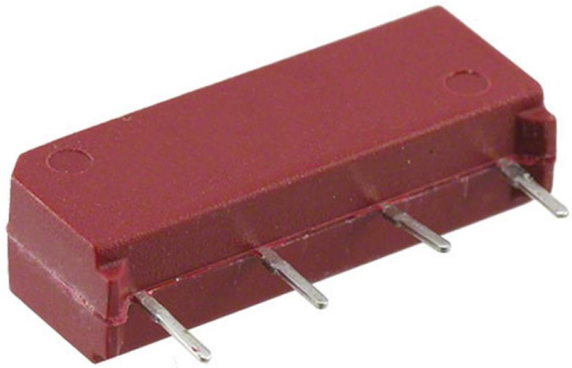

Figure 4-2 Reed relay SPST 500mA 5V (DigiKey, 306-1247-ND).

4.2.2 Data Acquisition System

The NI DAQ was controlled by LabVIEW 2017 software, which provides a graphical programming language for creating instrumentation, acquisition, and control application. An additional LabVIEW driver, DAQmx, was used for rapid processes with simplified programming. It also triggered the digital camera by clicking the mouse on the Imaging Edge software's press button consistently and repeatedly. Fig. 4-3 represents a block diagram in LabView.

A wiring diagram is shown in Fig. 4-4. The output voltage power source and maximum current of the DAQ are +5 V, ±3% and 150 mA, respectively. For the relay output electric circuit, load 1 and 4 were connected to electromagnet and power supply.

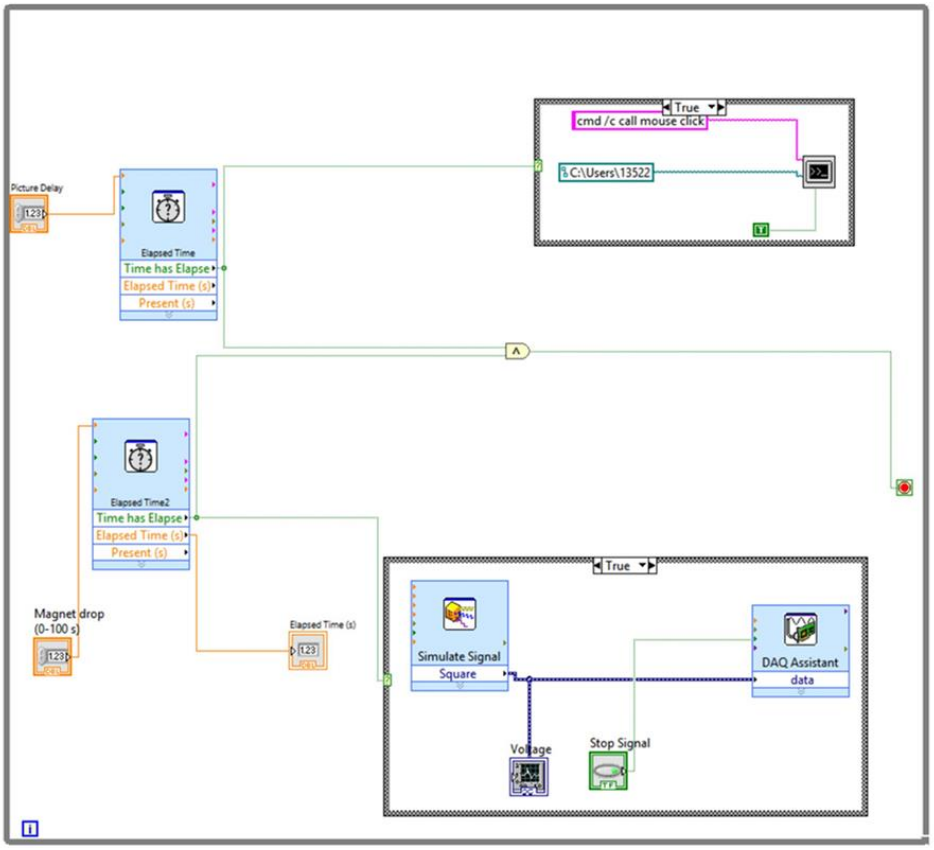

Figure 4-3 A block diagram in LabView.

For the control circuit, control 2 and 3 in the relay module, which has 10 mA coil current and 5 VDC coil voltage, were connected to analog output channels on DAQ.

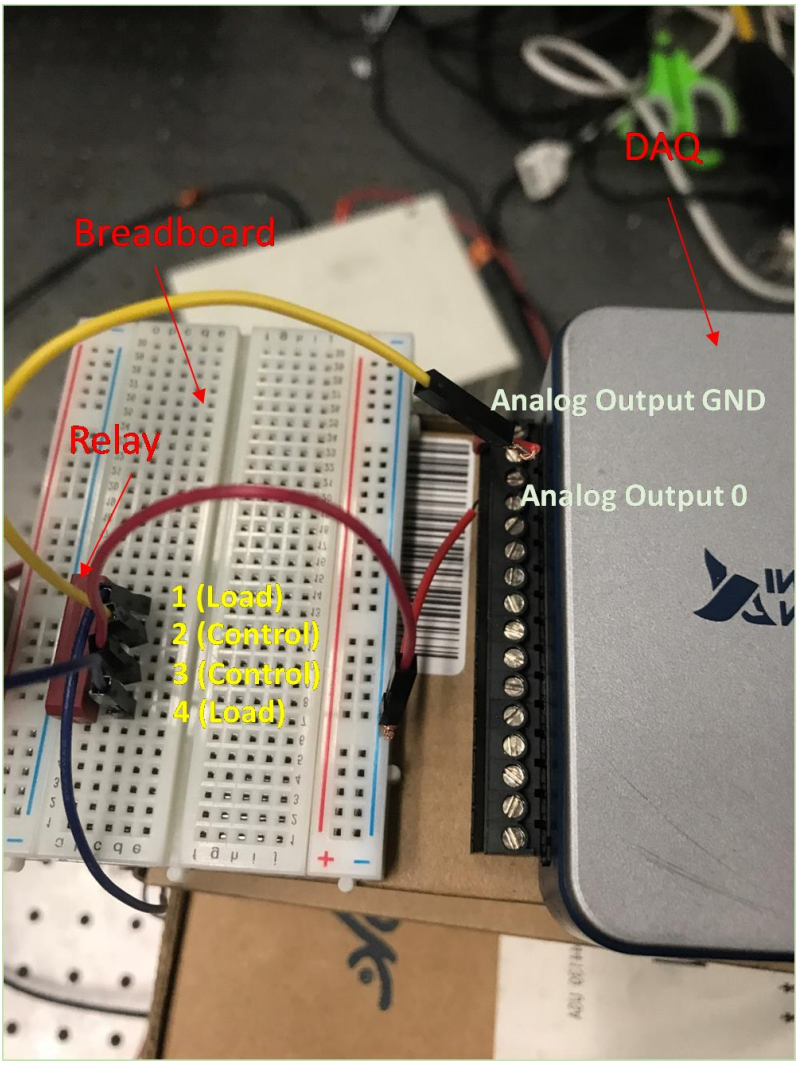

Figure 4-4 Data acquisition and reed relay on breadboard wiring diagram.

4.2.3 Firebrand generation

The procedure to generate smoldering firebrands was the same one used to generate smoldering embers. A butane lighter flame was introduced under the suspended rods in initial position for ignition. When flaming (see Fig. 4-5) self-extinguished, the rod was elevated by 90° and held by the electromagnet. A left click on the laptop triggered the camera and released the magnet. The camera exposure was set to capture the initial 90° of pendulum motion. With longer exposure time, the firebrand trajectories were

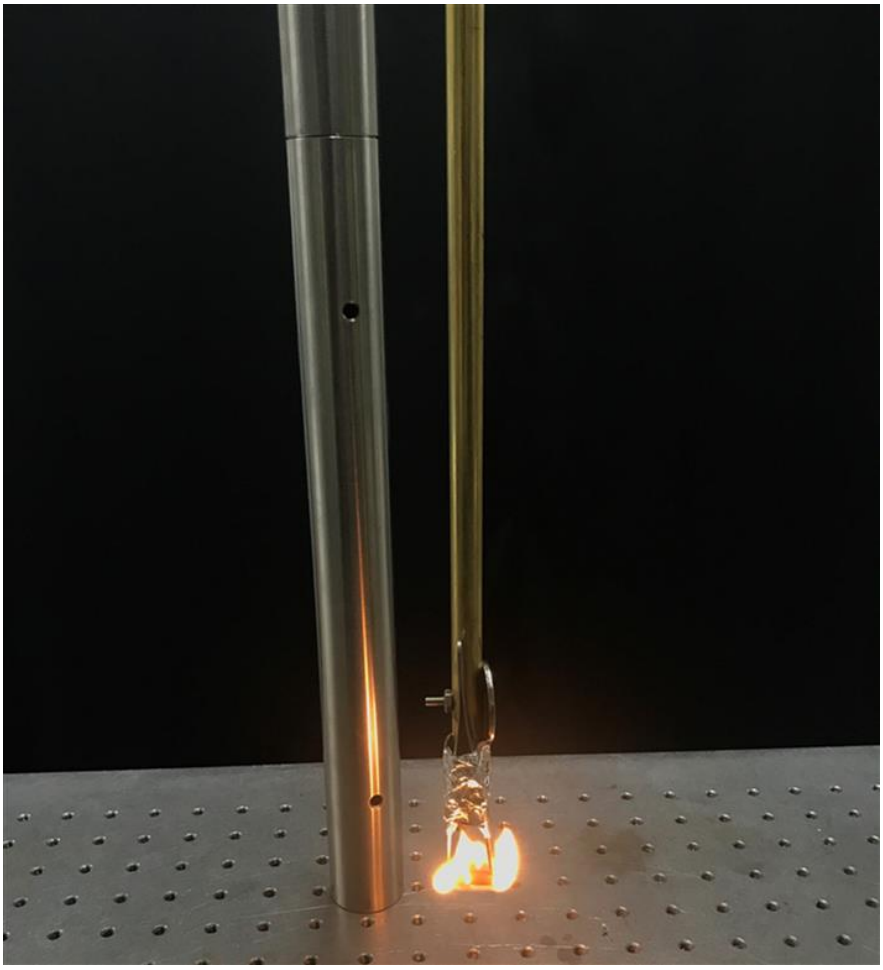

Figure 4-5 A color image of maple ignition with a gas phase flame.

recorded when the pendulum rod swung away from left to right as illustrated in Fig.4-6. The ISO and f number were selected to avoid saturation at any pixel in any color plane. The front of the camera lens was 1 m from the ember. The lens focal length was set to 11.8 mm. The mechanical shutter was used to avoid rolling shutter distortion. The camera was focused on the firebrand. Images were recorded in a dark room with a dark background.

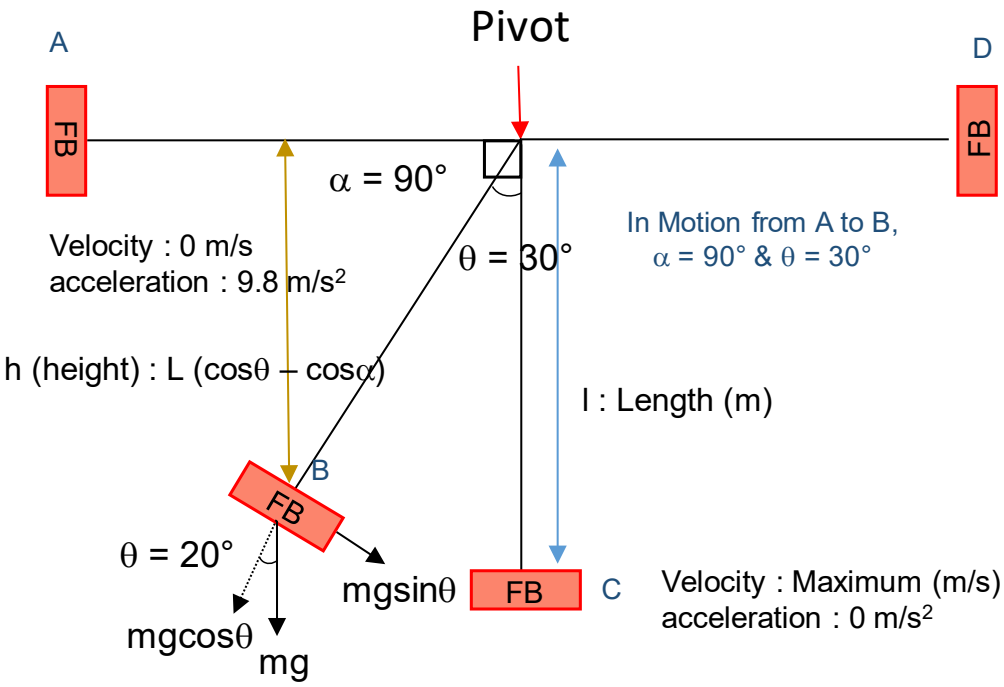

Figure 4-6 A schematic figure of a pendulum firebrand.

4.3 Results

4.3.1 Color image of pendulum firebrand

Fig. 4-7 represents a color image of a pendulum firebrand. The exposure time was 0.8 s. The ISO was 200 and the f number was 4. Unlike stationary ember images, most of the image of a pendulum firebrand images is dark.

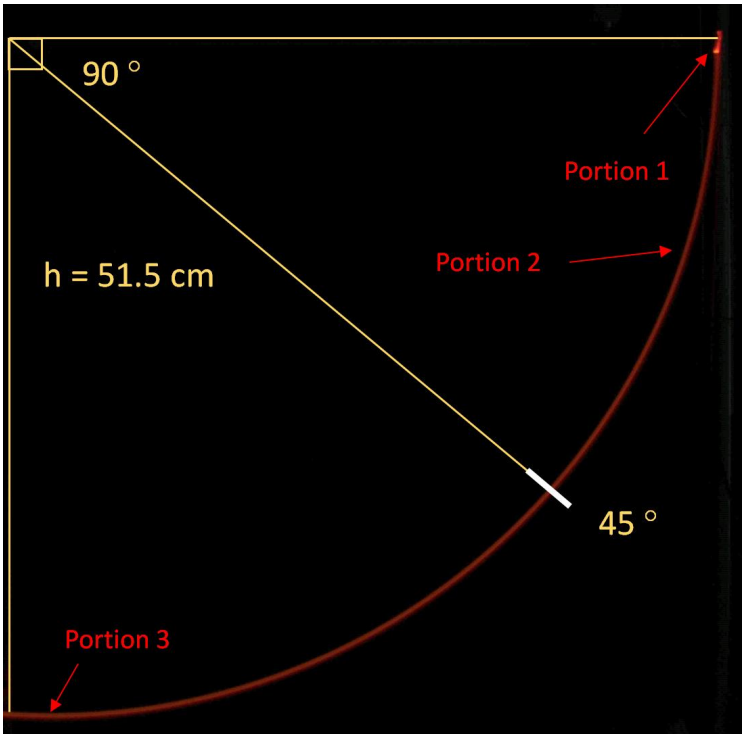

Figure 4-7 A color image (2874 × 2760 pixels) of a pendulum firebrand. For this image ISO = 200, f = 5, and t = 0.8 s.

4.3.2 Firebrand ratio pyrometry

The pendulum firebrand image of Fig. 4-7 was analyzed to determine color ratios for each pixel. These were converted to temperatures using the curve fit of G/R ratio from Fig. 2-13 and the pendulum firebrand temperature contour plot was created as illustrated in Fig. 4-8. No spatial smoothing was applied. MATLAB was used to convert ratios to temperatures. (Note that MS Excel was used for this function in Chapter 2.)

The ratio pyrometry correlation was extrapolated to 1300 °C. The temperature limits in the contour plots were adjusted to 650 – 1150 °C.

Three different positions were zoomed in to get a better view of the firebrand. Unsmoothed contour plots are shown in Fig. 4-9. Position 1 is when the smoldering

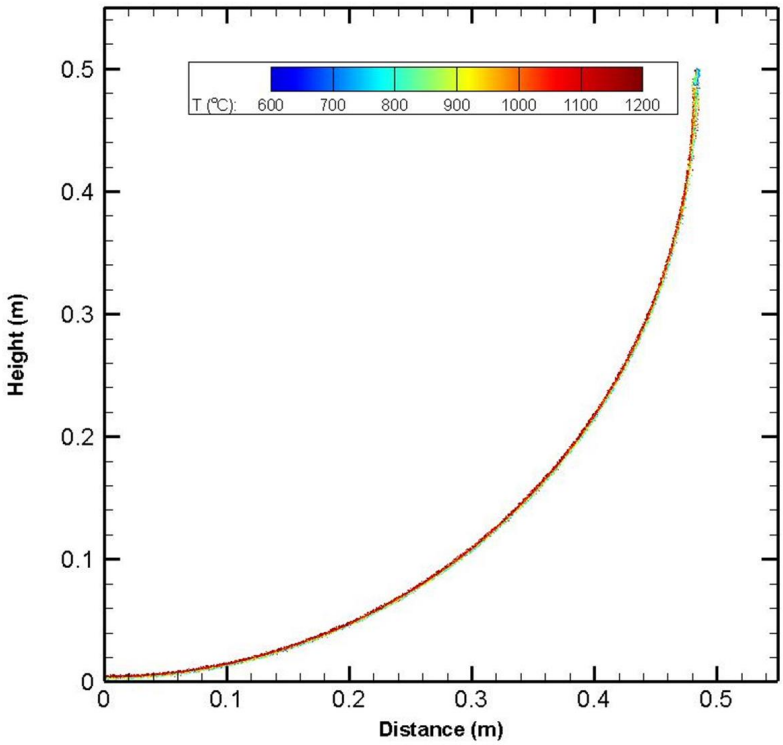

Figure 4-8 It is the resulting color contour plot of ratio pyrometry temperatures of pendulum firebrands.

ember was generated and starts to move. Position 2 is when the firebrand was moving downward. Position 3 is when the firebrand was passing the bottom. As shown in position 1, the relatively cold ember surface was starting to heat up as it began to move, and a hotter firebrand was observed in position 2 and 3. However, temperatures above

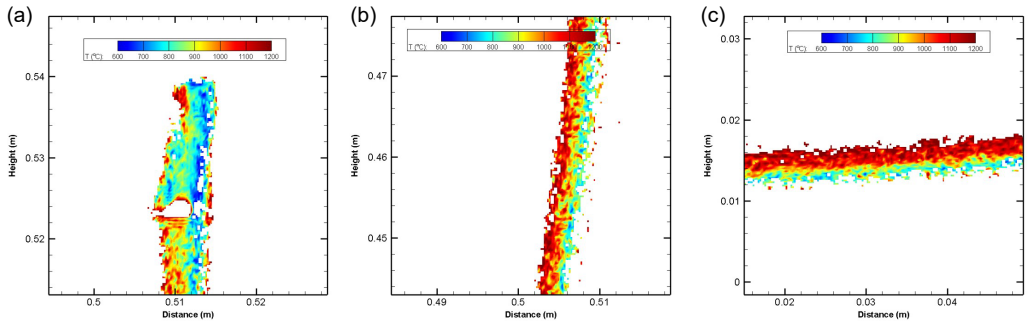

Figure 4-9 Contour plot zoomed in to three specific locations in the firebrand trajectory. (a) portion 1; (b) portion 1; and (c) portion 3 with unsmoothing.

0.5 m height including initial ember temperatures were discarded owing to oversaturated pixels.

Pendulum firebrand temperatures were determined by G/R pyrometry. Because the low SNR for ratio pyrometry, many signals were lost from the entire of firebrand trajectories.

4.3.3 Time correction for firebrand grayscale pyrometry

GS pyrometry on moving firebrands complicates temperature measurement because a pixel illumination time estimate for each pixel is required. The grayscale pyrometry temperatures along firebrand height were determined by GS pyrometry with a time correction.

A null temperature was assigned to every pixel that was outside the firebrand and to some pixels on the firebrand edge. Grayscale pixel values are found using Eq. (2-1). The mean temperatures every 20 pixels along the height and width above and below 45° angle as its starting point, respectively, were determined. Heights are plotted as a function of grayscale intensities, shown in Fig. 4-10. Grayscale values increase with decreasing height.

The firebrand velocity was measured with a high-speed camera and was also predicted using conservation of energy (Eq. 4-1). Neglecting friction, the total energy of the pendulum is constant [57]. Conservation of energy is

$$U_1 - U_2 = K_2 - K_1 \,, \tag{4-1}$$

where K_1, K_2, U_1, and U_2 are initial and final rotational kinetic energy and initial and final potential energy. Friction and drag are assumed to be negligible. K_1 and U_2 are equal to 0 at the top and bottom of the swing, respectively. U_1 is

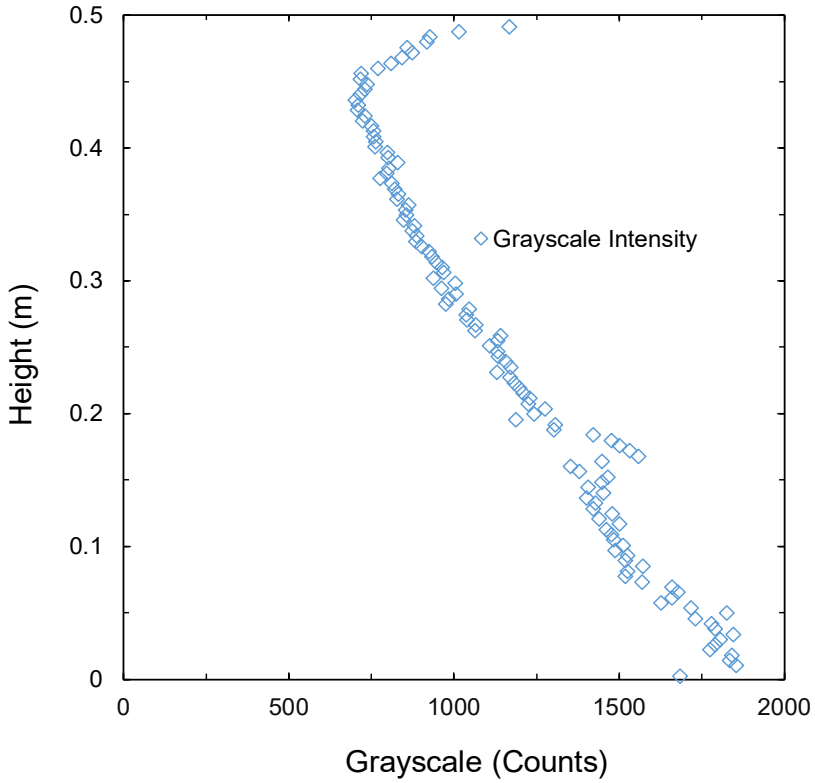

Figure 4-10 Heights plotted with respect to grayscale intensities. Height is defined as zero at the bottom of the trajectory.

$$U_1 = \mathrm{m\ g\ L}\ (\cos\theta - \cos\alpha)\,, \tag{4-2}$$

where g, L, m, α, and θ are the standard acceleration due to gravity (9.8 m/s), which causes the mass of firebrand to rotate downward, height of the firebrand (m), mass of firebrand, initial angle from A position (°), and angle from B position (°) in the motion. K_2 about the pivot point is found from:

$$K_2 = 1 / 2\ \mathrm{I}\ \omega^2\,, \tag{4-3}$$

where I is the moment of inertia about its center of mass for mass distributed pendulum rod. The moment of inertia about the end point of the rod is given by [58–59]

$$\mathrm{I} = 1 /3\ \mathrm{m\ L}^2\,. \tag{4-4}$$

Equating the change in potential energy and kinetic energy allows the angular velocity, ω (rad/s) to be determined from

$$\omega = [\ 24\ g\ (\cos\theta - \cos\alpha)\ /\ L\ ]^{-1/2}. \quad (4\text{-}5)$$

When the pendulum at an initial angle (α) moves to at an angle (θ), the height of firebrand can be defined as

$$h = L\cos\theta - \cos\alpha. \quad (4\text{-}6)$$

Substituting Eq. 4-6 into Eq. 4-5, the resulting angular velocity in terms of height is

$$\omega = [\ 24\ g\ h\ /\ L^2\ ]^{-1/2}. \quad (4\text{-}7)$$

Hence, the resulting firebrand velocity (m/s) is

$$v = 2\ \pi\ L\ /\ 360°\ 57.3\ \omega\ . \quad (4\text{-}8)$$

The pixel illumination time is defined as

$$t_p = L\ /\ v\ . \quad (4\text{-}9)$$

The firebrand height is plotted with respect to measured and calculated velocities and pixel illumination times using Eq. (4-8) and Eq. (4-9) in Fig. 4-11. The predicted maximum velocity at the bottom is 11.0 m/s but that measured is 4.0 m/s due to the friction. The predicted pixel illumination time is 2 – 14 ms and that measured is 5 – 130 ms, respectively.

On the basis of firebrand velocity and illumination time, firebrand locations are plotted as a function of normalized grayscale pixel values, which were determined by using Eq. (2-2), in Fig 4-12. Pixel illumination time is corrected by simple models and recording videos for each pixel along the height and velocity. The normalized grayscale values increase with decreased height with a 6 – 7 order of magnitude increase in *NI*.

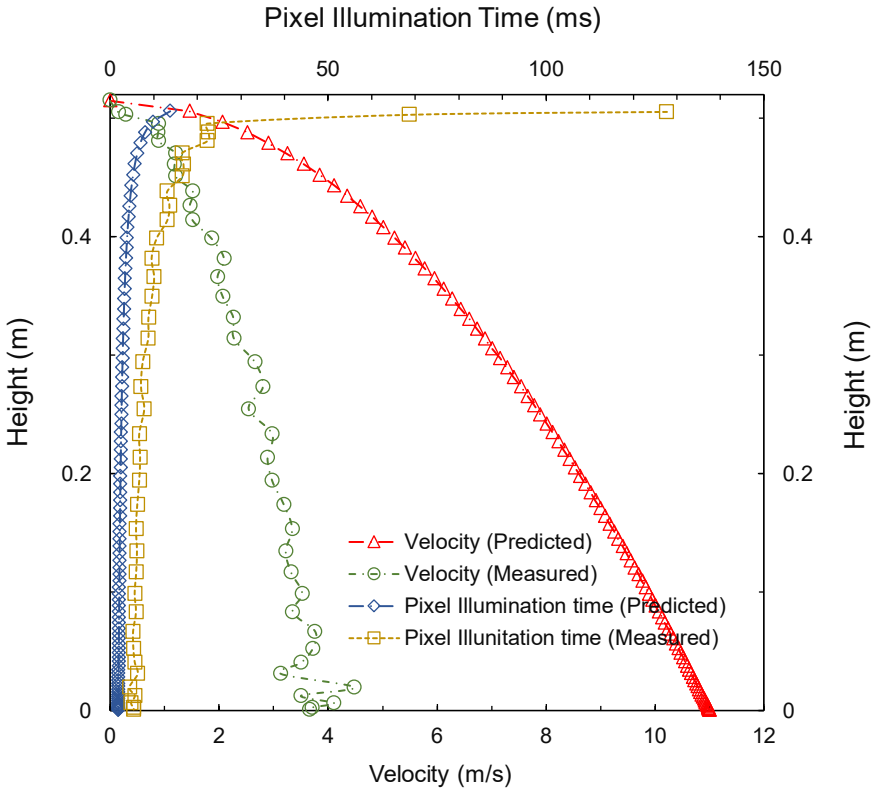

Figure 4-11 Heights plotted with respect to velocity (primary x axis) and pixel illumination time (secondary x axis).

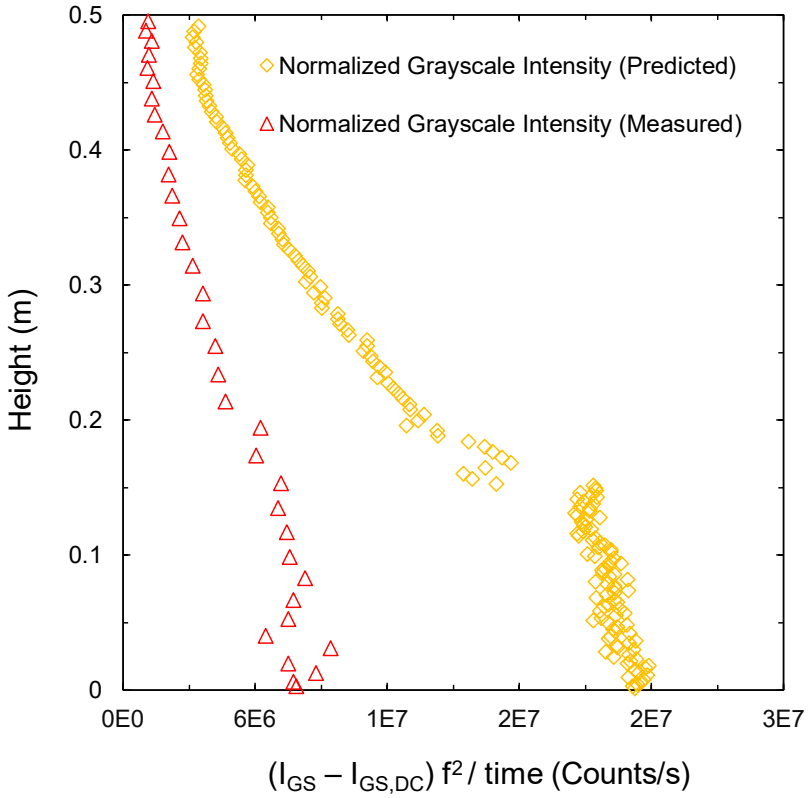

Figure 4-12 Heights plotted with respect to velocity with GS pixel values normalized by pixel illumination time and f-number.

4.3.4 Correlations between firebrand velocity and pyrometry temperatures

The quantitative correlation between pendulum firebrand temperature and velocity was studied comparing the resulting mean G/R and GS temperature every 20 pixels along the firebrand location in y axis above 45° angle and x axis below 45° angle. For grayscale pyrometry, the normalized GS results in Fig. 4-12 were converted to temperatures using the curve fit of Fig. 2-12. Comparing the two pyrometry methods, pendulum firebrand heights are plotted with respect to pyrometry temperatures as shown in Fig. 4-13. GR and GS temperatures slightly increased until reaching the location of maximum velocity.

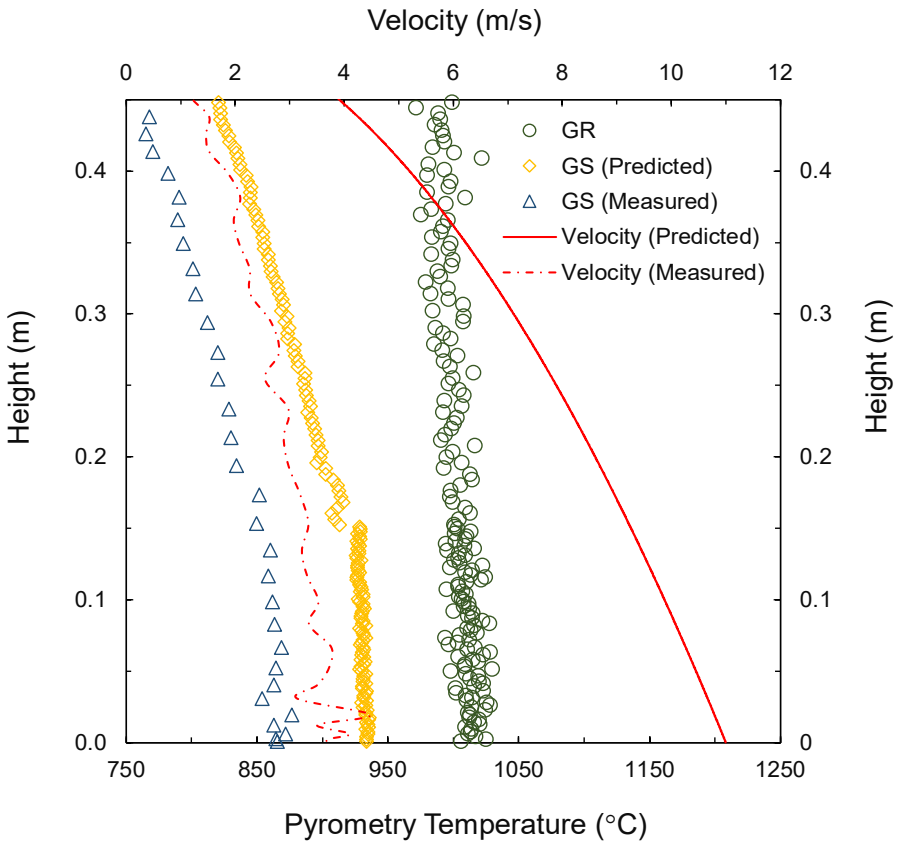

Figure 4-13 Heights are plotted with respect to G/R and GS temperatures.

GS temperatures, which had times corrected by simple models and recording videos, are lower than G/R temperatures.

Chapter 5: Spectrometer Calibration

5.1 Introduction

An optical spectrometer (also called a spectrophotometer, spectrograph, or spectroscope), is a device that measures light intensity as a function of wavelength [60]. It can be used to measure temperatures of smoldering materials. Optical spectrometers have many applications, including material identification, flame spectral diagnostics, and pyrometry in fire research [42,51,61–64].

A spectrometer was used to monitor the emission spectrum from the radiating shock wave by Deep et al. [42]. A spectral emissivity model was established by Xu et al. [51] to measure char particle temperatures determined by ratio pyrometry in combination with emission in the visible range detected by the spectrometer. Zhang et al. [61] observed excited radicals in co-flow jet normal and inverse diffusion flames by flame emission detected by spectrometry accompanied by image analysis. Hu et al. [62] measured the spectral impinging zone signals. Yan et al [63] measured spectral intensity, temperature, and emissivity of heated metal in coal power plant boiler furnaces using a spectrometer. The spectrometer was also coupled with Laser-Induced Breakdown Spectroscopy (LIBS) imaging and was used for analysis of elements in mining cores at the vacuum ultraviolet level by Trichard et al [64]. To date no study has measured the temperature of smoldering materials using optical spectrometry.

This chapter elucidates the spectrometer calibration in detail using a 16-bit Optics FLAME-S spectrometer. A blackbody radiation furnace was used to calibrate the spectrometer in the 700 – 1200 °C temperature range by measuring the optical emission

spectrum over a range of 200 – 850 nm. The calibration can be used to evaluate smoldering material temperatures such as embers and firebrands.

5.2 Spectrometer Calibration

5.2.1 Acquire components

The spectrometer was a FLAME-S-UV-VIS-ES (Ocean Optics) as shown in Fig. 5-1.

Figure 5-1 Optical Spectrometer.

Table 5-1 summarizes specifications of the spectrometer. It is a 16-bit Optics FLAME-S Spectrometer and costs $4400. It has a Sony ILX-511B line detector with 2048 pixels. Its wavelengths range is 200 – 850 nm and its resolution is 50 µm. The pixel

Table 5-1 Specifications of a spectrometer, FLAME-S-UV-VIS-ES (Ocean Optics).

	Minimum wavelength, nm	Maximum wavelength, nm	Number of Pixels	Bit depth
Manual	200	850	2048	16
Measurement	192.185	877.203	2048	15

corresponding to 623.02 nm was permanently saturated from previous improper use with a red laser. The available integration time was 1 ms – 65 s.

For spectrometry calibration, blackbody, radiometric and lamp calibration are possible. Here a blackbody furnace (Oriel 67032) was used. OceanView 1.6.7 software was used for data acquisition. For collecting light, a cosine corrector (Lambartian surface to collect light from 180 field of view, FOV), integrating sphere, bare fiber, and gershun tube have been widely used. In this experiment, a gershun tube was used, with interchangeable aperture disks for view angles of 1, 3, 8, 10, and 14° without any lenses. A 400 μm premium fiber, solarization-resistant with a length of 25 cm, was used.

5.2.2 Experiment setup

The spectrometer was calibrated with the blackbody as pictured in Fig. 5-2. The spectrometer and the blackbody furnace were mounted on the stage and apertures on the spectrometer and the hole made in the blackbody wall were aligned.

Measured spectral intensities at fixed temperatures were corrected for dark current and normalized by integration time. Dark current subtraction is important to correct baseline offset and fixed pattern noise [65]. Spectra of the blackbody were recorded for

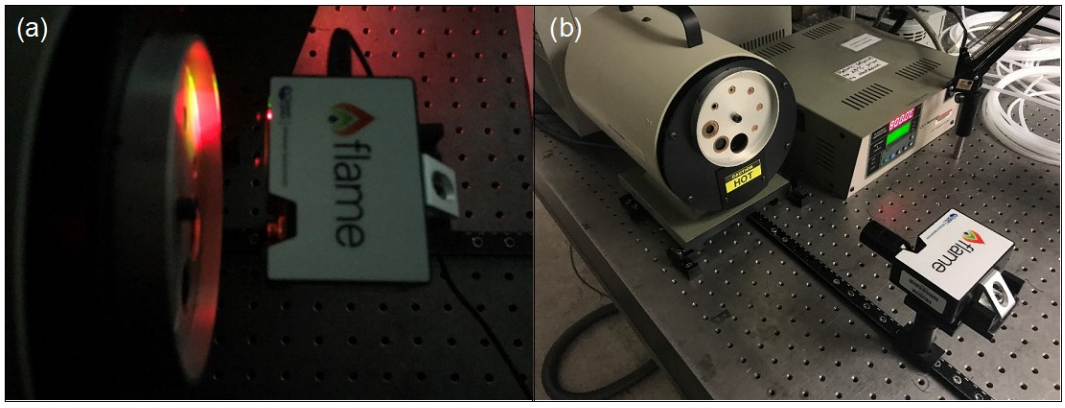

Figure 5-2 (a) Front; and (b) side views of the test apparatus: a blackbody furnace and a spectrometer.

various integration times, blackbody temperature, separation distances, and blackbody aperture diameters. A quantitative calibration was performed in the range of 600 – 850 nm.

5.2.3 Dark current

The dark spectra was measured by varying integration time from 0.1 s to 60 s as shown in Fig. 5-3. These were probed from up close within the range of 10 nm wavelength as

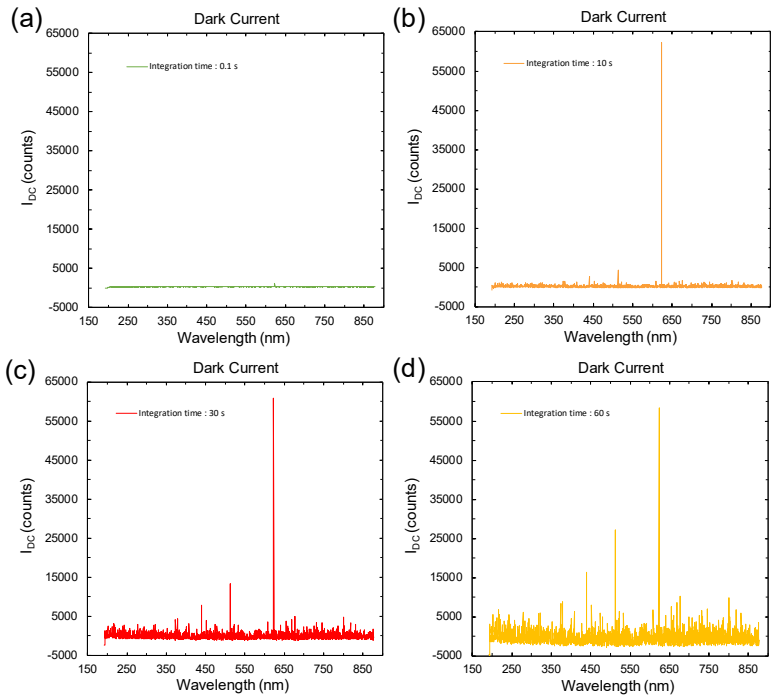

Figure 5-3 Intensity of dark currents plotted with respect to wavelength for different integration times. (a). 0.1 s; (b). 10 s; (c). 30 s; and (d). 60 s. Dead pixel counts were found at 623.02 nm.

shown in Fig. 5-4. This represents day-to-day variation of dark current signals for wavelengths of 750 – 760 nm over varying integration times. The dark currents were measured three times and were repeatable. Higher integration times had a wider range of dark current intensities. Similar results were obtained in the 250 – 260 nm wavelength region. Fig. 5-5 represents mean intensity of dark currents with

respect to integration time. The mean dark current intensity at 0 – 10 s integration time

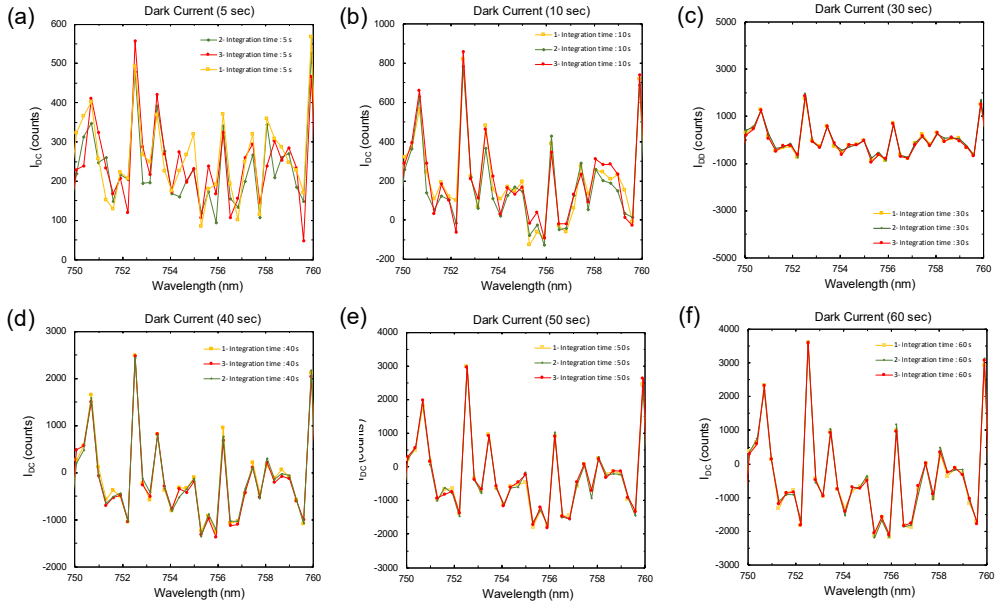

Figure 5-4 Day-to-day variation of dark current signals in the wavelength region of 750 – 760 nm varying integration time of (a). 5 s; (b). 10 s; (c). 30 s; (d). 40 s; (e). 50 s; and (f). 60 s.

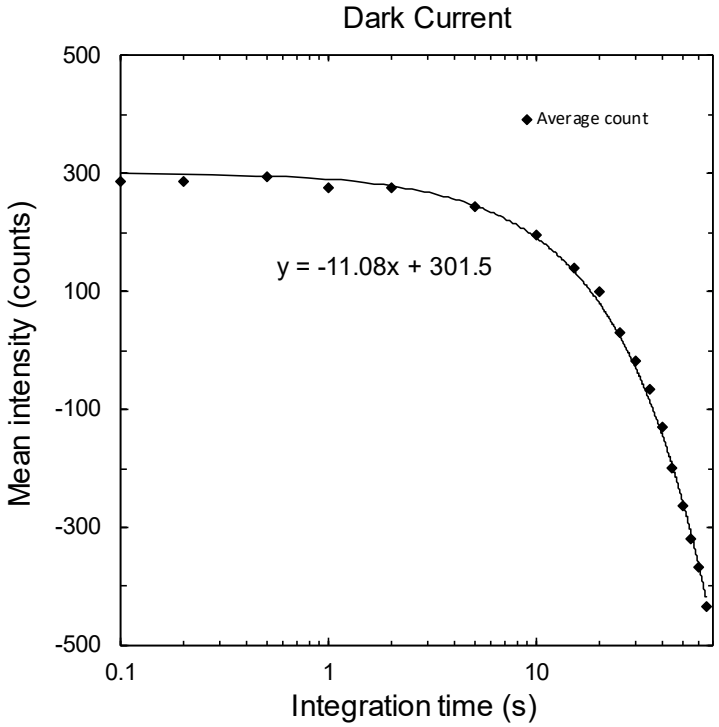

Figure 5-5 Mean intensity of dark current as a function of integration time.

was nearly constant, but signals abruptly decrease as integration times increase and become negative for times above about 10 s.

5.2.4 Effect of distance

The effect of distance between the camera sensor and the blackbody radiation furnace was investigated by measuring mean blackbody intensity integrated over the range of 200 – 850 nm wavelength. The blackbody temperature was 800 °C and the integration time was 2 s. There was no interchangeable aperture attached to the spectrometer. Fig. 5-6 represents mean intensity signals plotted with respect to the distance. The

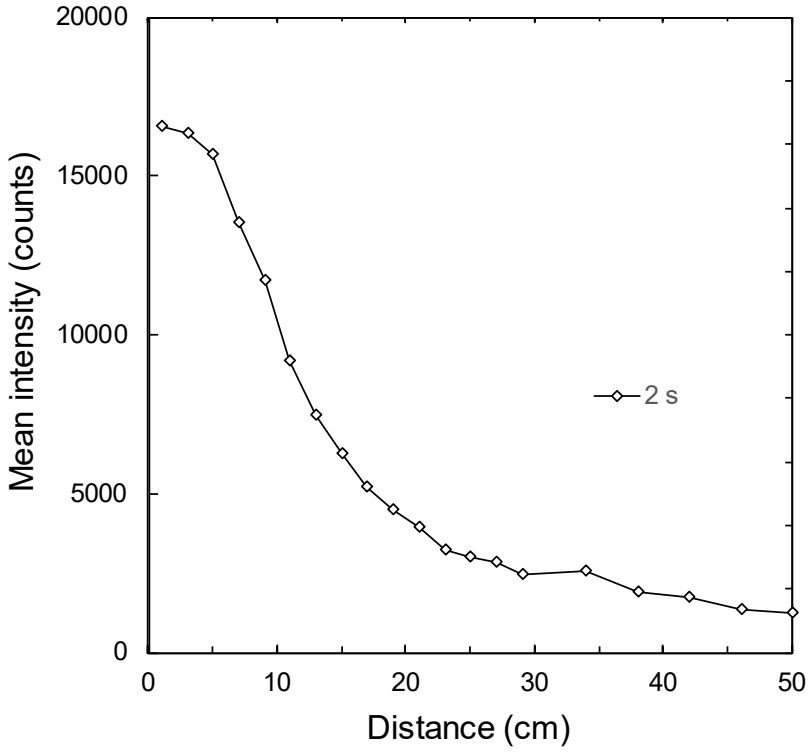

Figure 5-6 Mean signals plotted with respect to distance.

response was dependent on distance because the spectrometer collected light from outside the blackbody.

5.2.5 Linear response to integration time

Blackbody intensities were measured by varying the integration time at fixed temperatures as shown in Figs. 5-7 – 5-8. The blackbody temperature was 800 °C. An

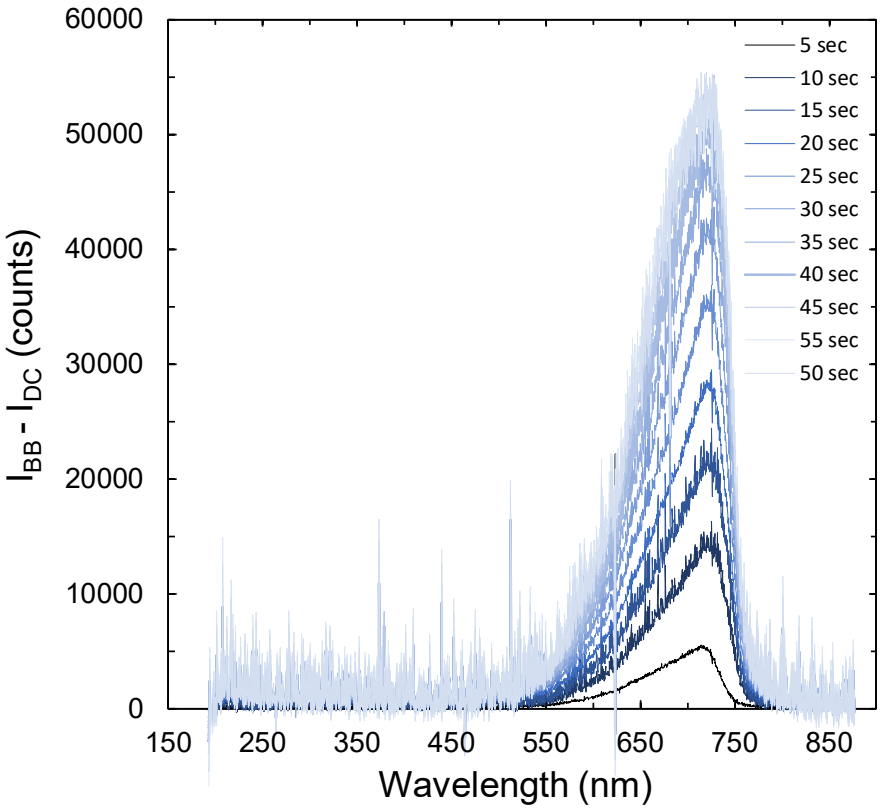

Figure 5-7 Linear response to the integration time. Raw data.

interchangeable aperture disk at the smallest field of view of 1° was installed. Fig. 5-7 shows the intensity measurements. The peak values were found at a wavelength of 710 nm regardless of the integration time. Measured blackbody intensities at 710 nm increase as integration times increases from 5 – 50 s. Fig. 5-8 shows mean blackbody intensity adjusted by dark current. It was found that the spectrometer response is linear with respect to integration time.

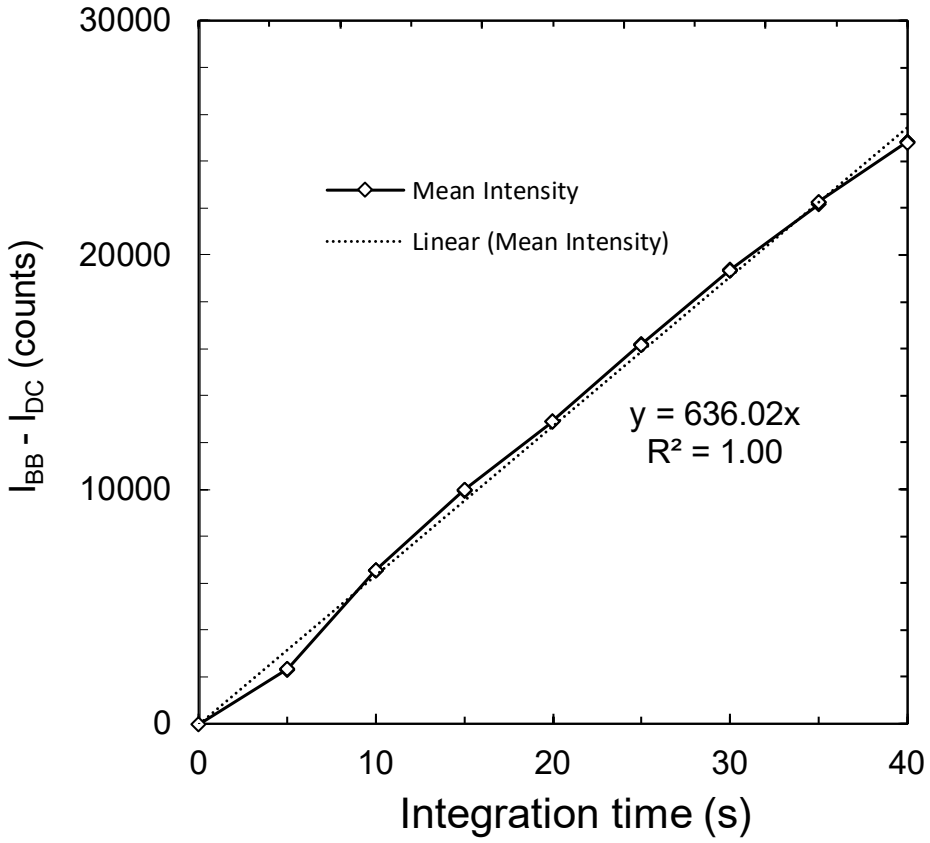

Figure 5-8 Linear response to the integration time. (a) raw data; (b) mean intensity as a function of integration time.

5.2.6 Effect of aperture size

The effect of field of view (FOV) at different aperture angles was investigated for a blackbody temperature of 800 °C. Aperture disks at 1, 3, 8, 10, and 14° were used. The distance between the blackbody and the spectrometer was 8 cm. Fig. 5-9 represents intensities normalized by the integration time plotted with respect to the wavelength. When FOV was limited to a smaller angular area, signals of radiance were weak due to insufficient incident flux. The signal was being saturated at angles of 10° and14°.

The spectrometer calibration curve for each aperture angle is shown in Fig. 5-10. Blackbody intensities were normalized by integration time and corrected by the spectral

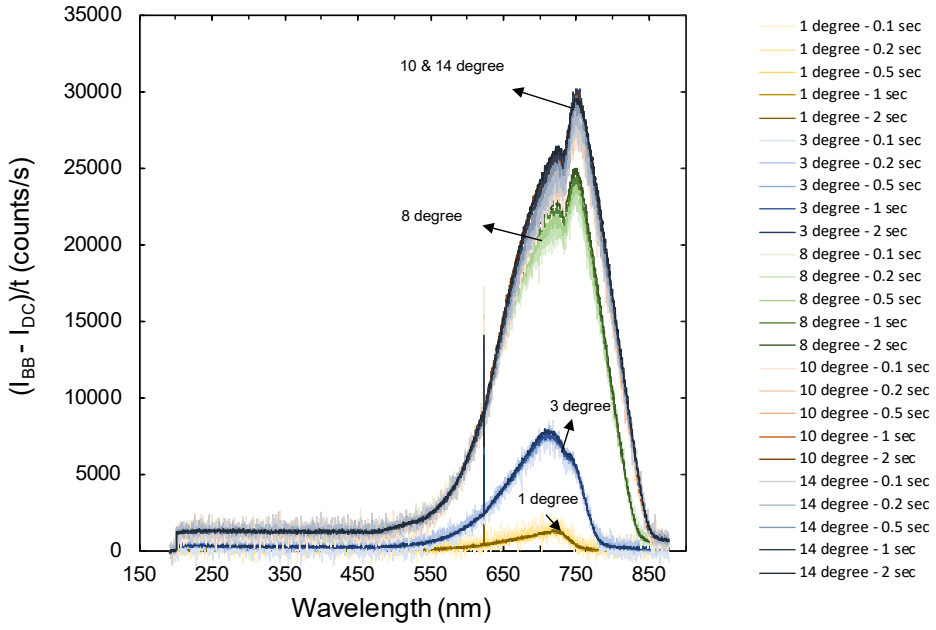

Figure 5-9 Mean intensity of dark current as a function of integration time.

emissive power of an ideal blackbody (Eq. 2-3). Only the 600 – 800 nm wavelength range was considered because different behaviors were found at shorter and longer wavelengths. All the curves collapse the measurements regardless of the integration time and blackbody temperature for each different aperture angle. However, the calibration curves vary with aperture size. The limitation of the optical spectrometry is a spatial emission integrated spectrum over the target measured under the viewing angle of the aperture attached on the spectrometer [42]. The 3° aperture size was selected for measuring the spectra of smoldering materials.

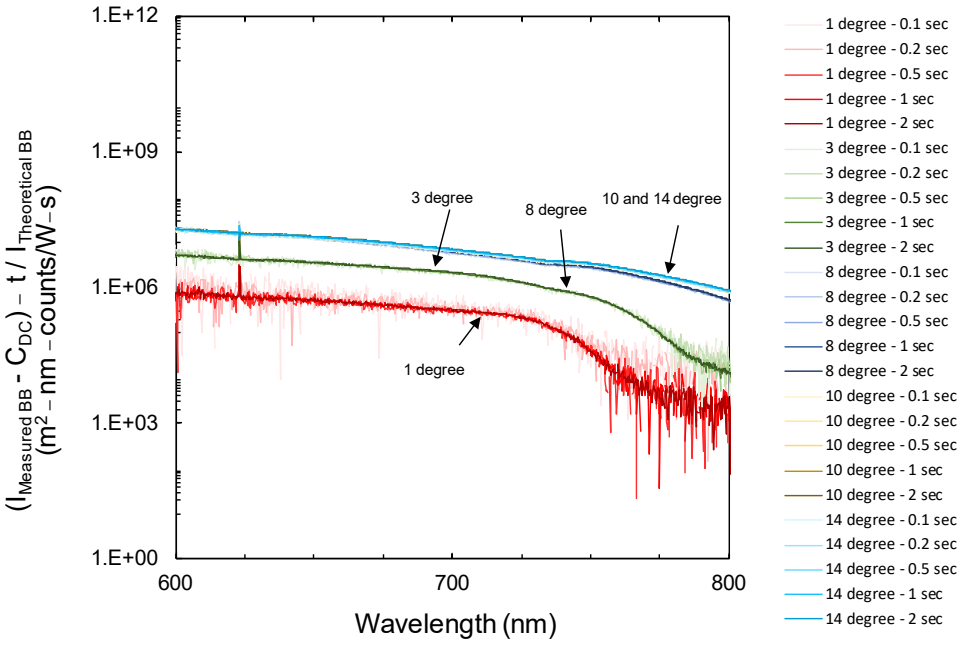

Figure 5-10 Intensity normalized by integration time and blackbody spectral intensity with different aperture size.

5.2.7 Effect of temperature

The blackbody intensities were measured at blackbody temperatures of 700 – 1200 °C. The distance between the blackbody and the spectrometer was fixed. The view angle was 3°. The largest aperture on the blackbody entrance was used. The calibration curves were made as shown in Fig. 5-11. The curves at different temperatures are in agreement from 600 – 800 nm. Any curve fits in Fig. 5-11 allow spectrometry on smoldering materials.

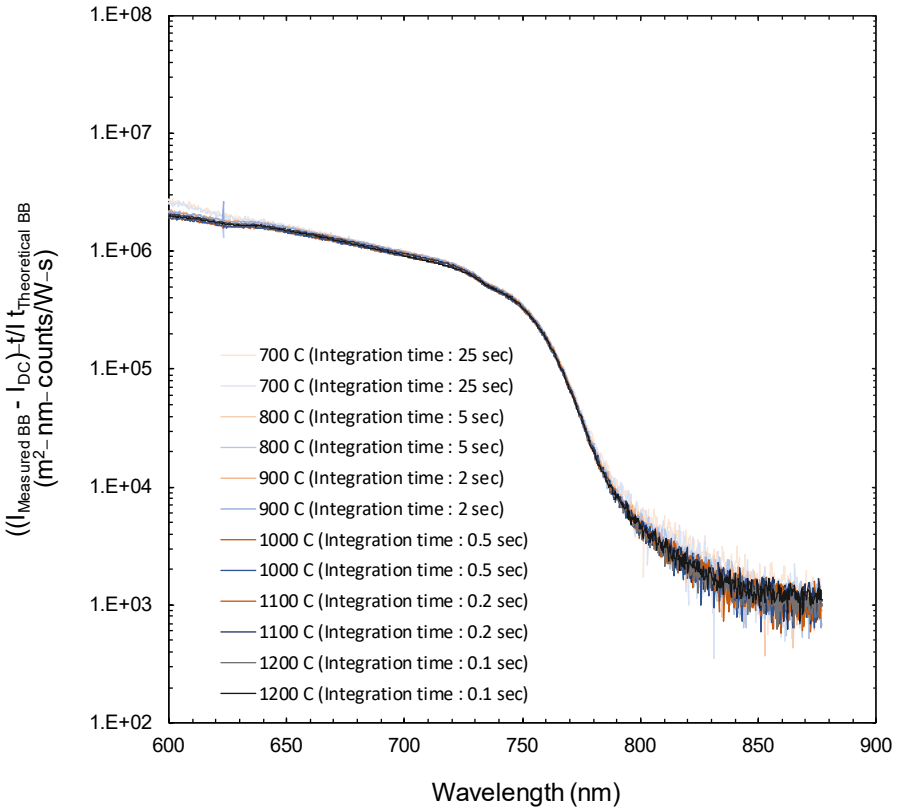

Figure 5-11 Intensity normalized by the integration time and the blackbody spectral intensity with different blackbody temperature.

Chapter 6: Smoldering Materials with High Air Velocity

6.1 Introduction

This chapter involves upward smoldering of materials varying air jet flow velocity. Smoldering combustion is a heterogenous surface combustion reaction [66–70]. Smoldering can occur for various materials such as wood, cotton, cellulose, cigarette, peat, polyurethane foam, dust, etc.

Smoldering can be controlled by two mechanisms: the rates of oxidizer supply to and heat transfer from the reaction zone [67–69]. Increasing the rate of oxidizer supply generally promotes the rate of smoldering spread. Smolder temperatures generally increase with increasing air velocity.

There have been many studies of smoldering. Moussa et al. [71] investigated the theory and performed experiments on the smoldering combustion mechanism of cylindrical cellulosic materials. Three regions were distinguished: pyrolysis, char, and porous residual char and/or ash. A correlation between the maximum temperature and the rate of smoldering spread was found but without any convection. Kinbara et al. [72] measured the velocity of downward smoldering propagation using circular cylindrical incense, rolled paper, cardboards strips, and piles of cardboard. The theory of downward smoldering was developed assuming (1) heat produced from smoldering is governed by air supplied by diffusion, (2) heat is proportional to ignition temperature of the materials, and (3) air supply and heat dissipation occur at a stagnant layer.

Smoldering behavior was also investigated with different air velocities for upward and downward flows. Yang et al. [73] investigated the effects of air flow on smoldering incense in controlled air flow (around 0 – 10 m/s). They studied correlations between

smoldering temperature and burning rate of materials and air flow velocities. These studies were conducted with air flowing in the opposite direction of the smoldering propagation. Ohlemiller et al. and Torero et al. [67–69] demonstrated forward and reverse smoldering through porous fuels with imposed air flow and modeling. Air flow was limited to 5 mm/s in polyurethane foam. Palmer [74] studied smoldering combustion for fine cork, grass dust, sawdust, and fireboard with air flow in the range of 0 – 4 m/s. Previous studies of smoldering materials in air flow were conducted in relatively low air flows and little is known about the extinction of smoldering at high air velocities. Temperatures were measured with fine thermocouples, which are not accurate due to conductive and radiative heat losses and smoldering quenching.

Here smoldering materials are experimentally investigated with high air velocities. Effects on the temperature, burning velocity, and extinction are explored. The main difference between this study and previous studies is the investigation of possible smoldering extinction at high air velocity. Upward smoldering with upward air flows are studied. The temperatures were determined by the pyrometry established in Chapter 2 and were validated by optical spectrometry developed in Chapter 5. Different materials such as incense, maple rod, rolled paper, rattan sticks, and ashless filter paper were selected as fuels, oriented vertically, and aligned with an air jet a few centimeters away. The major effort was to identify correlations between air velocity and burning rate and temperature.

Among the fuels, only smoldering incense achieved steady state smoldering.

6.2 Experimental

6.2.1 Sample preparation and generation

Incense sticks (Hosley AMZ-BS53731ON-1-EA), rolled paper, maple rod (McMaster Carr 97015K13), rattan sticks (Shenzhen Aigua Technology Co,. Ltd. B071DPG9T1), and ashless filter paper (Whatman F1241-1A) were prepared. Vertical pieces of rolled paper with 10 cm length were prepared. The paper was rolled as tightly as possible by using small drill bits. The round maple rods were 6.4 mm in diameter and 20 mm long. 3.2 mm holes were drilled on axis to promote burning. The rattan sticks, 3 mm in diameter and 30 cm long were prepared. The ashless filter paper was round with a diameter of 4.7 cm diameter. It was rolled into cylinders. All prepared materials were dried in an oven at 103 °C to remove moisture.

Fig. 6-1 shows the test schematic for experiments. All fuels were vertically placed for steady burning as shown in Fig. 6-1. A camera and an air jet were mounted securely in a fixed position. The materials were mounted on a post with a jack screw to keep the smolder region in a nearly fixed position. The distance between the ember and the jet

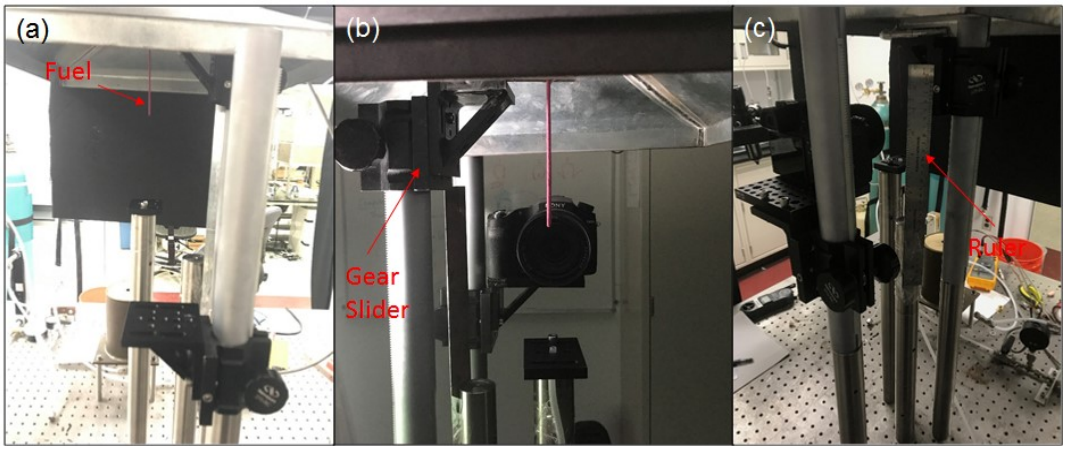

Figure 6-1 Testing configuration for incense. Shown here are: (a). front view; (b). back view; and (c). side view.

was 10 cm. The boundary of a virgin fuel and the end of smoldering tip was examined. A butane lighter flame was introduced under the end of materials for ignition. For generating steady smoldering, the gas phase flame was extinguished when the tip began glowing. Air was supplied from the air jet with varying air velocities. The jet velocity was controlled by a needle valve, which was attached to a pressure gauge. The air velocity was measured by an anemometer (Omega AI.05261). This procedure was repeated many times to ensure repeatability.

6.3 Results

6.3.1 Color image of incense

Images of smoldering incense without the air jet are shown in Fig. 6-2. For all images, ISO = 200, f = 2.4, and t = 0.02 s. Ashes accumulated on the tip and then collapsed. The rate of ash production was far more than with maple rods. The camera was focused son the ember. Images were recorded in a dark room with a dark background.

Figure 6-2 Smoldering incense.

6.3.2 Results of smoldering incense without air supply

Fig. 6-3 illustrates smoldering incense temperatures determined by G/R and GS pyrometry with no air flow supply. The pyrometry developed in Chapter 2 was performed. The polynomials in Figs. 2-12 and 2-13 were used to determine the incense temperatures.

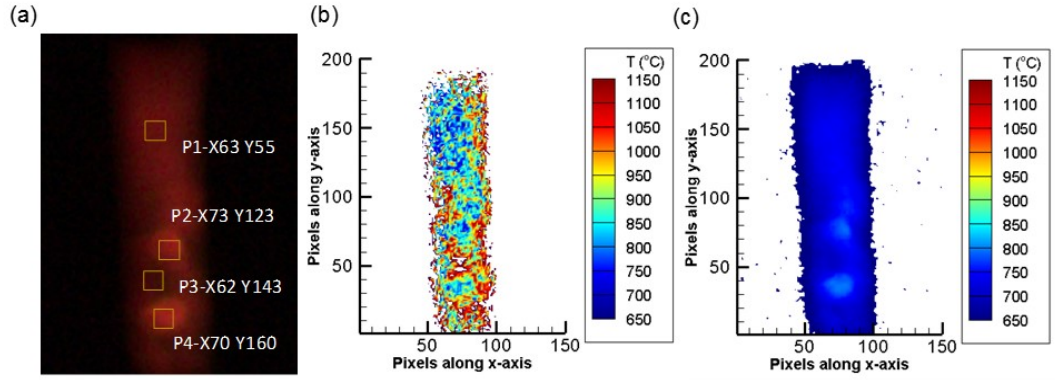

Figure 6-3 A representative color image (150 × 200 pixels) of smoldering incense. Shown here are: (a) a color image; (b) ratio pyrometry result; and (c) grayscale pyrometry result.

A representative color image of smoldering incense displayed in Fig. 6-3a. Fig. 6-3b and Fig. 6-3c shows the ratio pyrometry and grayscale pyrometry results. Table 6-1 summarizes the incense temperatures measured from 4 isothermal regions in Fig. 6-3a. The G/R ratio and GS pyrometry indicate temperatures of 844 – 964 °C and 704 - 790

Table 6-1 Smoldering incense results.

	X	Y	GR (°C)	GS (°C)	Emiss x trans
P1	63	55	841.0	741.3	0.12
P2	73	123	844.1	773.9	0.24
P3	62	143	964.2	704.4	0.01
P4	70	160	867.0	790.3	0.22

°C, respectively. Mean G/R ratio and GS pyrometry over all whole pixels (200X150) were 929 ± 115.9 °C and 692.6 ± 45.9 °C. The incense's mean emissivity times transmissivity using Eq. (3-4) was 0.01 – 0.24 (assuming a wavelength of 600 nm) due to interference from emissivity, ash transmissivity, and smoke from incense. This is smaller than an ember's mean emissivity times ash transmittance found in Chapter 3 because thicker ash was created from the incense.

The pyrometry temperatures were validated by the temperature characterized by the optical spectrometer. Light emission from the smoldering incense, which was 8 cm away from the spectrometer, was measured in the field of view (FOV) at 3° as shown in Fig. 6-4. Fig. 6-4 shows incense intensity normalized by 5 s of the integration time.

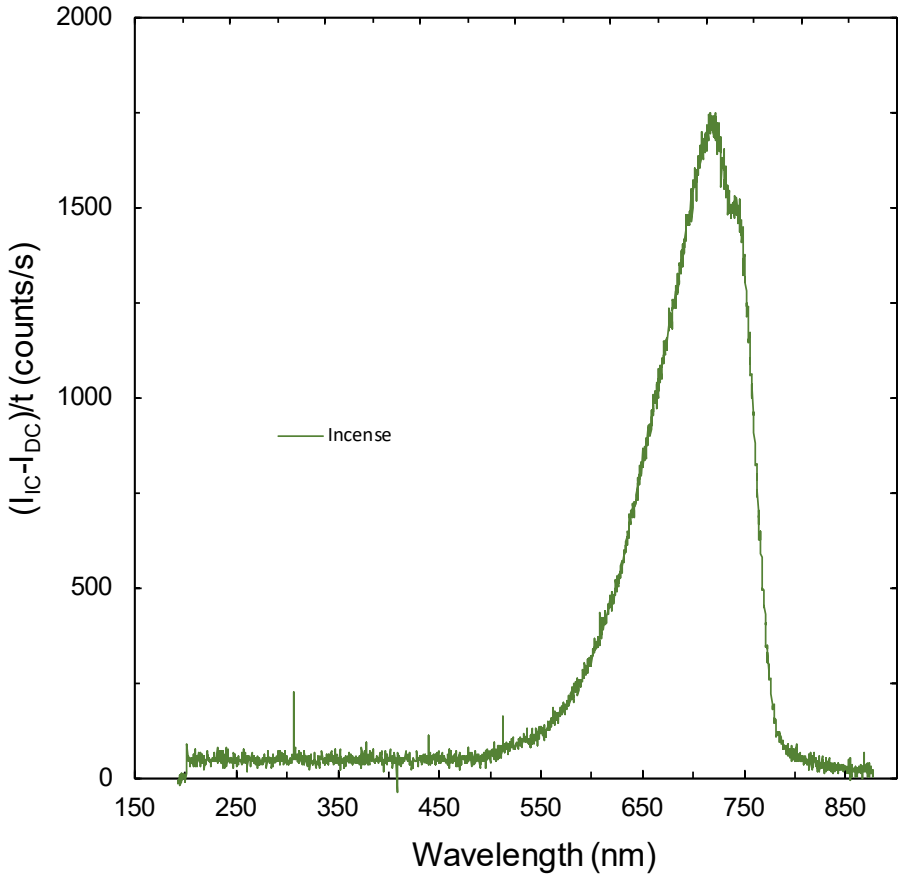

Figure 6-4 Incense intensity normalized by time.

As shown in Fig. 6-5, this data was corrected by calibration in the 550 – 800 nm wavelength range represented in Fig. 5-11. To quantify incense temperature from incense intensity, spectrum pyrometry was performed. The measured corrected incense intensity was 0.00754 W/m^2 at 700 nm. It was divided by 0.00048 and 0.0034 W/m^2,

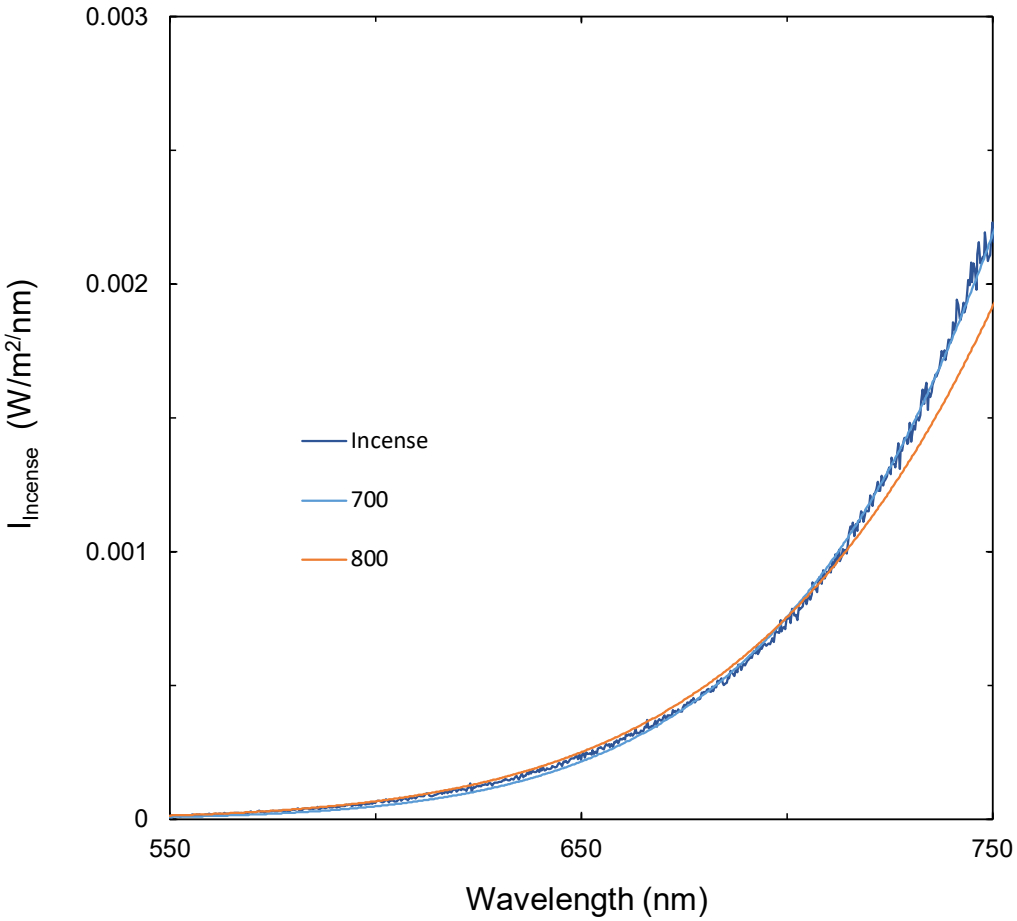

Figure 6-5 Incense intensity calibrated by correction factor.

which corresponds to the blackbody spectral intensities from the Planck's law at 700 and 800 °C temperatures at 700 nm wavelength. The resulting constant values, 1.58 and 0.22 were multiplied by blackbody spectral intensities at 700 and 800 °C over the whole wavelength range. The resulting two curves of blackbody spectral intensity at 700 and 800 °C are plotted in Fig. 6-5. Incense temperature was 700 – 800 °C. There was significant difference between G/S ratio pyrometry temperature and optical spectrometry temperature. It is attributed here to the error of the optical spectrometer: The spectrometer has low spatial resolution so that collected spectra can be measured

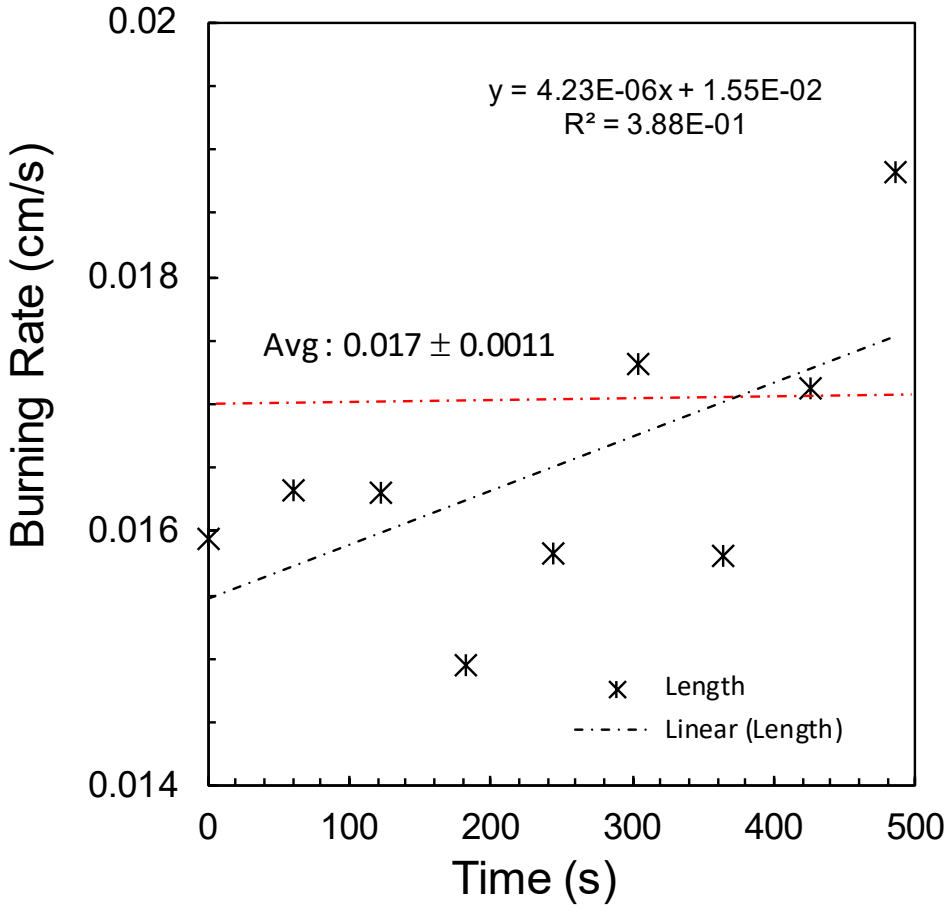

Figure 6-6 Burning rate (primary y axis) plotted as a function of time.

from unwanted areas. Also, smoldering material emissivity should be assumed to have large uncertainty. Fig. 6-6 represents the burning rate of smoldering incense plotted with respect to time. The mean burning rate was 0.017 ± 0.001 cm/s.

6.3.3 Results of smoldering incense with varying air velocity

Tests were performed with the air jet flowing. Mean smoldering incense temperatures were determined by G/R ratio and GS pyrometry. Burning rates at various air velocities

were measured. Fig 6.6 represents burning rate and ratio pyrometry temperatures plotted as a function of air velocity.

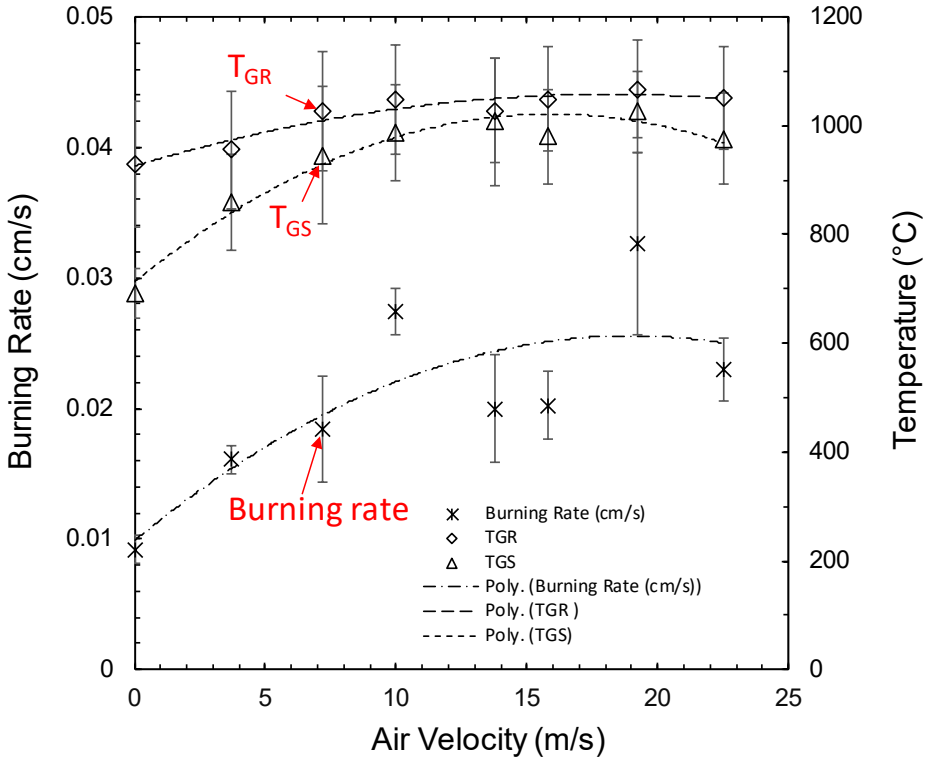

Figure 6-7 Burning rate (primary y axis) and ratio/grayscale pyrometry temperature (secondary y axis) plotted as a function of air velocity.

The temperature increased with increasing jet velocity owing to more oxygen attacking the surface, faster reactions, and heat transfer until air velocity reached 19.2 m/s. However, temperatures and burning rate were reduced at 22.5 m/s and extinction occurred at 28 m/s, which higher than in previous work [67–69,73–74]. A large variation of these measurements may come from unsteady flow rates.

6.3.4 Results of other smoldering materials

It is remarkable that none of the other fuels supported steady smoldering wither with or without the air jet. These were: rolled paper, maple rod, rattan sticks, and ashless filter paper. Smoldering rolled paper was generated uniformly in the beginning but at one point, smoldering only inside the rolled paper was propagating, while the smoldering rate outside was extinct. At least fifteen rolled papers were burned, with the same results. It was not possible to generate steady state smoldering of the vertical maple rods and smoldering was extinguished even if a slow air flow was supplied. Rattan sticks and ashless filter paper did not smolder. Ashless filter paper burned fast with a gas-phase flame, but never smoldered without flaming.

Chapter 7: Conclusions

In this dissertation, an imaging stationary ember and airborne firebrand pyrometer, which can contribute to better understanding of temperature measurement in WUI society, was developed. It uses an inexpensive digital color camera. The main findings are as follows:

1. An inexpensive and accurate pyrometer for embers was developed using a Sony DSC-RX10 III Cyber-shot digital camera. Ratio pyrometry and grayscale pyrometry were considered. The pyrometer was calibrated for ratio and grayscale pyrometry with a blackbody furnace with the range of 600 – 1200 °C.

2. A digital color camera was used to perform pyrometry on smoldering wood embers. The major findings are as follows.
    a. Ratio pyrometry is accurate when the product $\varepsilon\tau$ is invariant across the detected wavelengths. Grayscale pyrometry is accurate when $\varepsilon\ \tau$ is unity, which is less common. The SNR for grayscale pyrometry is 18 times as high.
    b. Grayscale pyrometry temperatures are lower and are linearly correlated with ratio pyrometry temperatures. This correlation allows hybrid pyrometry, whereby the grayscale temperatures are corrected upward to account for nonunity $\varepsilon\tau$. It also allows determinations of $\varepsilon\tau$.
    c. The hybrid pyrometer had a spatial resolution of 17 μm, a SNR of 530, and an estimated uncertainty of ± 20 °C.

d. The measured ember temperatures were between 750 – 1070 °C with a mean of 930 °C. Ash and smoke caused negligible attenuation. The mean $\varepsilon\tau$ was 0.73.

e. The pyrometer precision was +/- 0.0005 °C.

f. Even fine bare-wire thermocouples quench smolder reactions and make imperfect thermal contact. For these tests the thermocouple indicated a temperature 230 °C below the mean ember temperature.

3. A digital color camera was used to perform pyrometry on a pendulum firebrand. There are key results, as follows.

   a. The pendulum firebrand temperature was measured using pyrometry. The trajectory of a pendulum firebrand was recorded in a color image with a streak using 0.8 s exposure time.

   b. Temperature increases as the velocity of pendulum firebrands increases.

   c. Ratio pyrometry determined mean temperatures of pendulum firebrand between 878 – 1064 °C.

   d. Grayscale pyrometry temperatures were lower.

4. Pyrometry was performed on upward smoldering materials. There are key results were as follows.

   a. The burning rate of incense in quiescent air was 0.01 cm/s. Ratio pyrometry determined a mean temperature of 929 °C. Grayscale

pyrometry determined a lower temperature. The spectrometer determined the temperature between 700 – 800 °C.

b. The incense's mean $\varepsilon\,\tau$ was 0.01 – 0.24, which is smaller than an ember's $\varepsilon\,\tau$ because thicker ash was created from the incense.
c. Ratio pyrometry determined mean temperatures of smoldering incense between 929 – 1067 °C with an air velocity of 0 – 19 m/s. The burning rate increased to 0.03 cm/s. At 22.5 m/s, the incense temperature decreased to 1050 °C.
d. The smoldering incense was extinguished with an air velocity of 28 m/s.
e. Rolled paper, maple rod, rattan sticks, and ashless filter paper were unable to generate steady one-dimensional propagation of the reaction front during smoldering regardless of air supply.

Chapter 8: Future work

8.1 Firebrands

1. Different firebrand materials, sizes, and moisture contents will be tested.
    a. (e.g. birch, pine, oak, etc.)
2. The overall emissivity will be measured using a heat flux sensor and pyrometry.
3. Additional tests are needed such as daylight tests, far away tests, and tests with smoke.
    a. Light correction is needed, comparing values for the same ember in many lighting situations. The light intensities outside the ember should be subtracted (e.g. direct sunlight).
    b. Pyrometry will be performed on blackbody and firebrands with a large amount of smoke generation (thick enough) to verify ratio pyrometry works well in the presence of smoke.
    c. Far away tests are needed varying the distance between the camera and embers/firebrands.
4. Pyrometry will be performed on airborne firebrand showers in real fire scenarios. The relationship between firebrand velocity and temperature will be identified.

8.2 Smoldering materials

1. The effect of air velocity on smoldering materials will be investigated.
    a. An accurate wind velocity measurement should be used. The air flow rate in the air jet tube will be measured.
    b. Different fuels such as improved rolled paper, smoldering woods, charcoal, etc. will be used.

c. The relationship between air velocity and burning rate and temperature will be studied.

d. Possible extinction at high air jet velocity will be studied.

e. New modeling of velocity versus temperature/burning rate will be established and will be verified by predicting and measuring those.

Appendix A. Script for Pixels Analysis

Matlab code 1 (Drag area and export mean intensity)

```
clear all
close all

format shortG

% Reads in image, sets to 16-bit values
RGB = imread('800.tiff');
RGB2 = im2uint16(RGB);

% Selects pixels to analyze
imshow('800.tiff');
rect = getrect;
startx = round(rect(1) - 0.5);
starty = round(rect(2) - 0.5);
width  = round(rect(3));
height = round(rect(4));

x = width;
y = height;
tot = x*y;

% Empty matrices for storage of RGB values
R = zeros(x, y);
G = zeros(x, y);
B = zeros(x, y);

a = zeros(1, tot);
b = zeros(1, tot);
ctr = 1;

% Creates matrix of indexes for call to impixel
for i=startx:(startx+x-1)
    for j=starty:(starty+y-1)

        a(ctr) = i;
        b(ctr) = j;

        ctr = ctr+1;
    end
end

% Gets pixel values of image using indexes a,b
pixels = impixel(RGB2,a,b);

% Stores red, green, and blue in separate vectors
red = pixels(:,1);
green = pixels(:,2);
```

```
blue = pixels(:,3);

% Sorted red, green, and blue
sortedred = sort(red);
sortedgreen = sort(green);
sortedblue = sort(blue);

ctr = 1;

% Reassembles matrix of R,G,B values
for c=1:x
    for d=1:y

        R(c,d) = red(ctr);
        G(c,d) = green(ctr);
        B(c,d) = blue(ctr);

        ctr = ctr+1;
    end
end

% Averages
AvgRed = round(mean(red))
AvgGreen = round(mean(green))
AvgBlue = round(mean(blue))
```

Matlab code 2 (Export 200 X 200 pixels intensity)

```
clear all
close all

RGB = imread('_DSC1485.tiff');
RGB2 = im2uint16(RGB);


x = 200;
y = 200;
tot = x*y;

R = zeros(x, y);
G = zeros(x, y);
B = zeros(x, y);

a = zeros(1, tot);
b = zeros(1, tot);
ctr = 1;
startx = 2688;
starty = 1752;

for i=startx:(startx+x-1)
    for j=starty:(starty+y-1)
```

```
        a(ctr) = i;
        b(ctr) = j;

        ctr = ctr+1;
    end
end

pixels = impixel(RGB2,a,b);

red = pixels(:,1);
green = pixels(:,2);
blue = pixels(:,3);

sortedred = sort(red);
sortedgreen = sort(green);
sortedblue = sort(blue);

ctr = 1;

for c=1:x
    for d=1:y

        R(c,d) = red(ctr);
        G(c,d) = green(ctr);
        B(c,d) = blue(ctr);

        ctr = ctr+1;
    end
end

AvgRed = mean(red)
AvgGreen = mean(green)
AvgBlue = mean(blue)
```

Matlab code 3 (Temperatures from G/R ratio)

```
clear all
close all

format shortG

% reads in excel
excelred = xlsread('RGB (ratio).xlsx','Red');
excelgreen = xlsread('RGB (ratio).xlsx','Green');

% dimension (X,Y)
x = length(excelred);
y = size(excelred,1);

% creates empty matrices
gr = zeros(y, x);
Tgr = zeros(y, x);
```

```
red = excelred - 48.4;
green = excelgreen -7.3;

for i = 1:x
    for j = 1:y

        % constraint to disregard pixels with small red and green
          signals
        if(green(j,i)<100)
        green (j,i) = 0;
        end

        if(red(j,i)<200)
        red (j,i) = 0;
        end

        % log10 of green/red ratio
        gr(j,i)=log10(green(j,i)/red(j,i));

        if(isnan(gr(j,i)) == 1 || isinf(gr(j,i)) == 1)
            gr(j,i) = 0;
        end

        % Make 0 outside of the temperature range of 500 - 1300
        degree C
        if (-2.466>gr(j, i)|| gr(j, i)>-0.816)
        gr(j, i) = 0;
        end

        gri = gr(j, i);

        % Use color ratios to solve for temperature
        Tr_gr = 292.25846742827*gri^3+1733.7511309046*gri^2
        +3614.49035899075*gri+3253.19866773618;
        T_gr = Tr_gr;

        % record temperature in new matrices
        Tgr(j, i) = T_gr;

        % Replace NAN values and 3253.19866773618 (constant values
        from above equation) with 0
        if(Tgr(j,i) == 3253.19866773618)
        Tgr(j,i) = 0;
        end
    end
end

% write temperatures out to new excel file
filename = 'RGB (temp).xlsx';
xlswrite(filename, Tgr, 'Temp Green_Red');
```

Appendix B. Isothermal Regions of Embers

B.1 Test 1 (smoldering ember with fan activation)

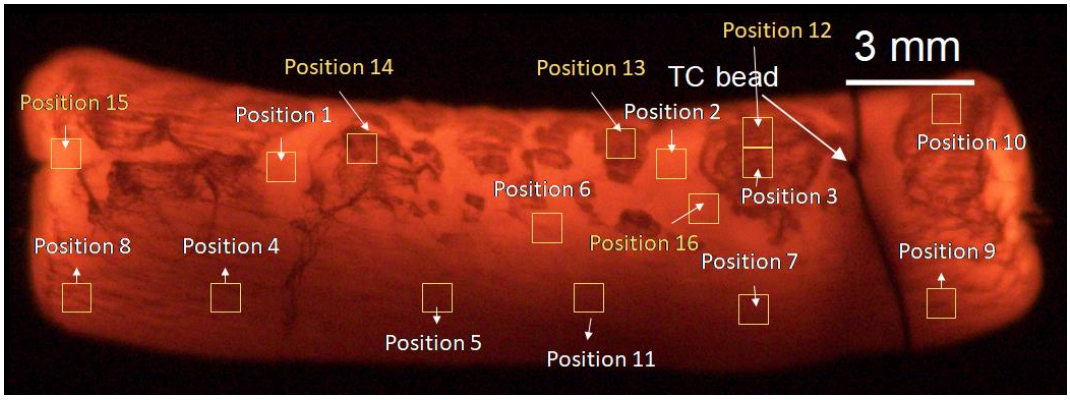

Figure B-1 Indication of isothermal regions of ember from color image (1200 × 432 pixels) of a glowing ember at 50 s. The exposure was 1.3 ms at f/2.8.

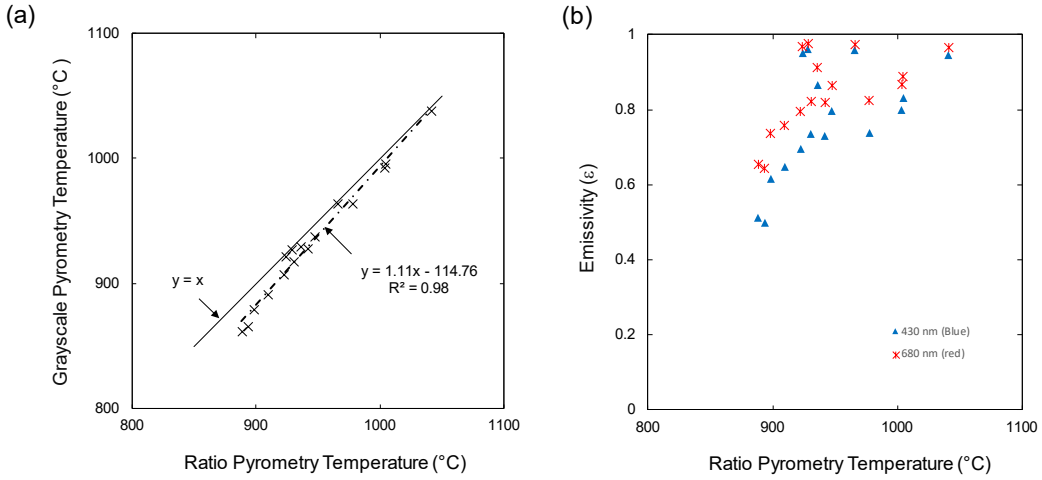

Figure B-2 (a) Grayscale pyrometry temperature and (b) visible emissivity plotted with respect to ratio pyrometry temperature for smoldering embers in Fig. B-1.

B.2 Test 2 (smoldering ember before and after fan activation)

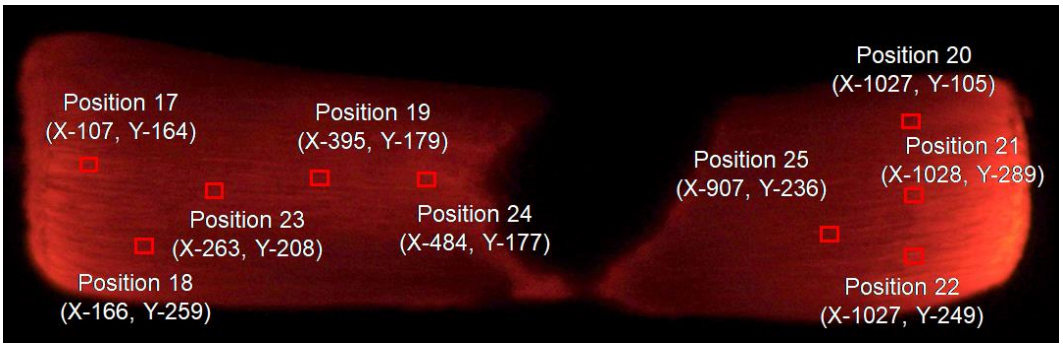

Figure B-3 Indication of isothermal regions of an ember from a color image (1188 × 372 pixels) of a glowing ember. The exposure was 1/30 s at f/2.4. Captured before the fan was activated.

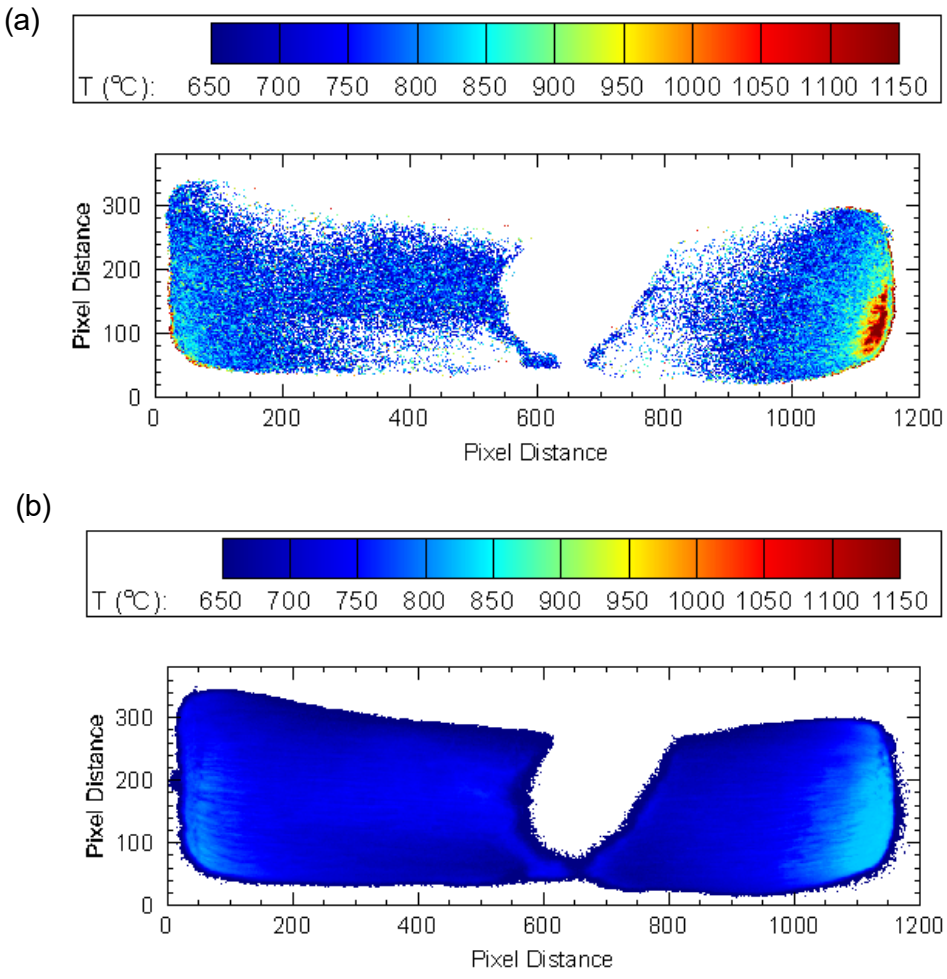

Figure B-4 (a) Non-smoothed ratio pyrometry results for red/green pyrometry; and (b) intensity pyrometry results from color image in Figure B-2.

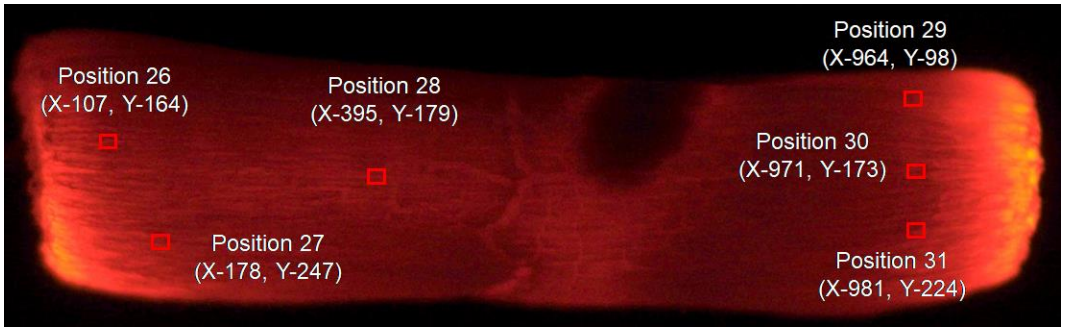

Figure B-5 Indication of isothermal regions of an ember from a color image (1140 × 348 pixels) of a glowing ember. The exposure was 1/15 s at f/2.4. Captured before the fan was activated.

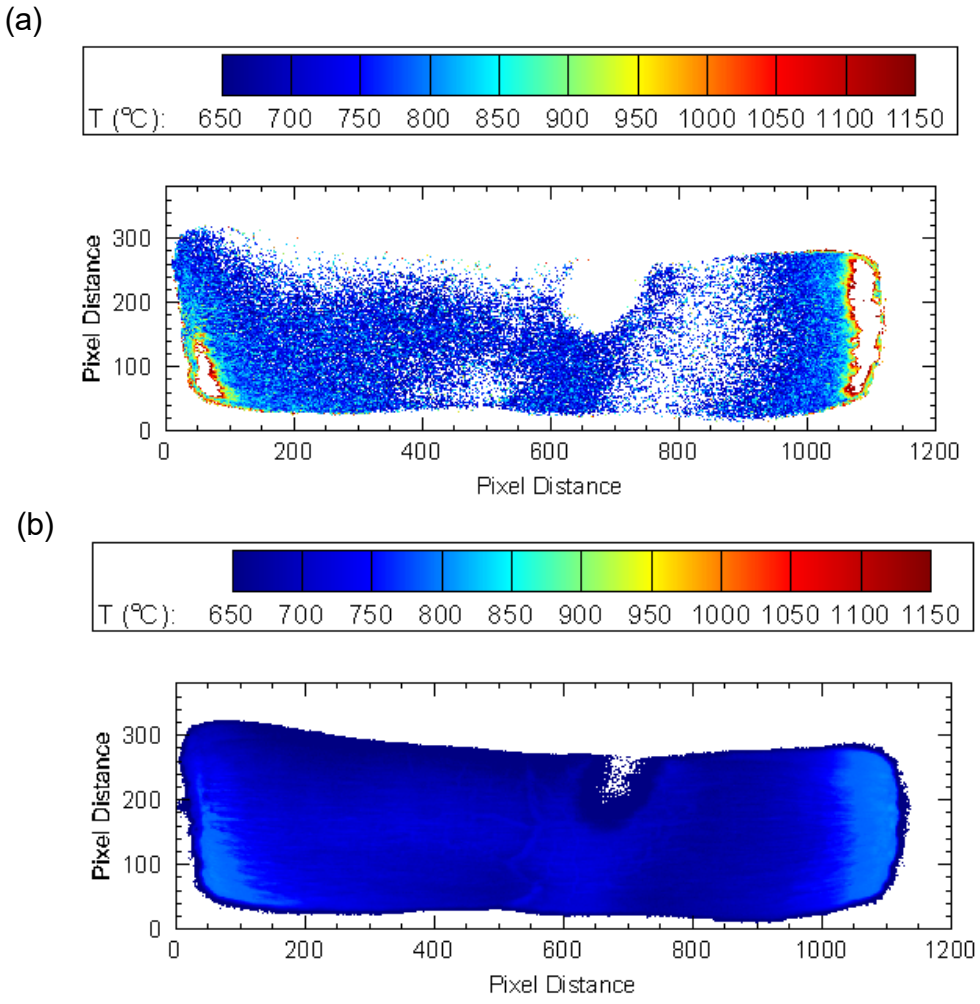

Figure B-6 (a) Non-smoothed ratio pyrometry results for red/green pyrometry; and (b) intensity pyrometry results from color image in Figure B-5.

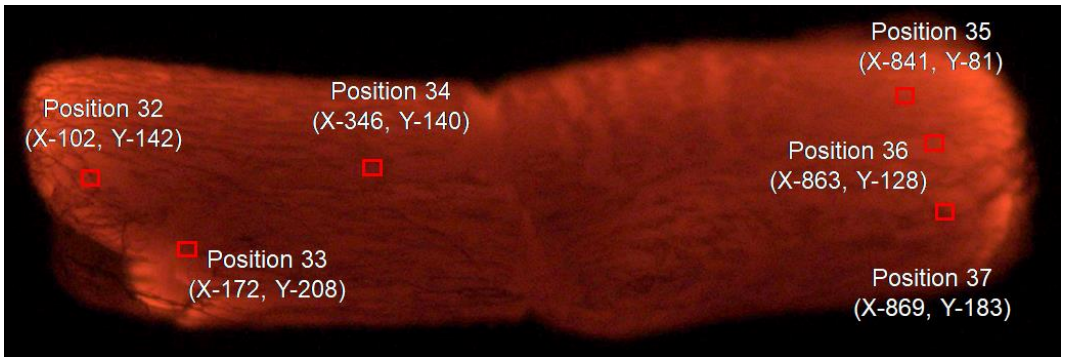

Figure B-7 Indication of isothermal regions of an ember from a color image (996 × 324 pixels) of a glowing ember. The exposure was 1/640 s at f/2.4. Captured after the fan was activated.

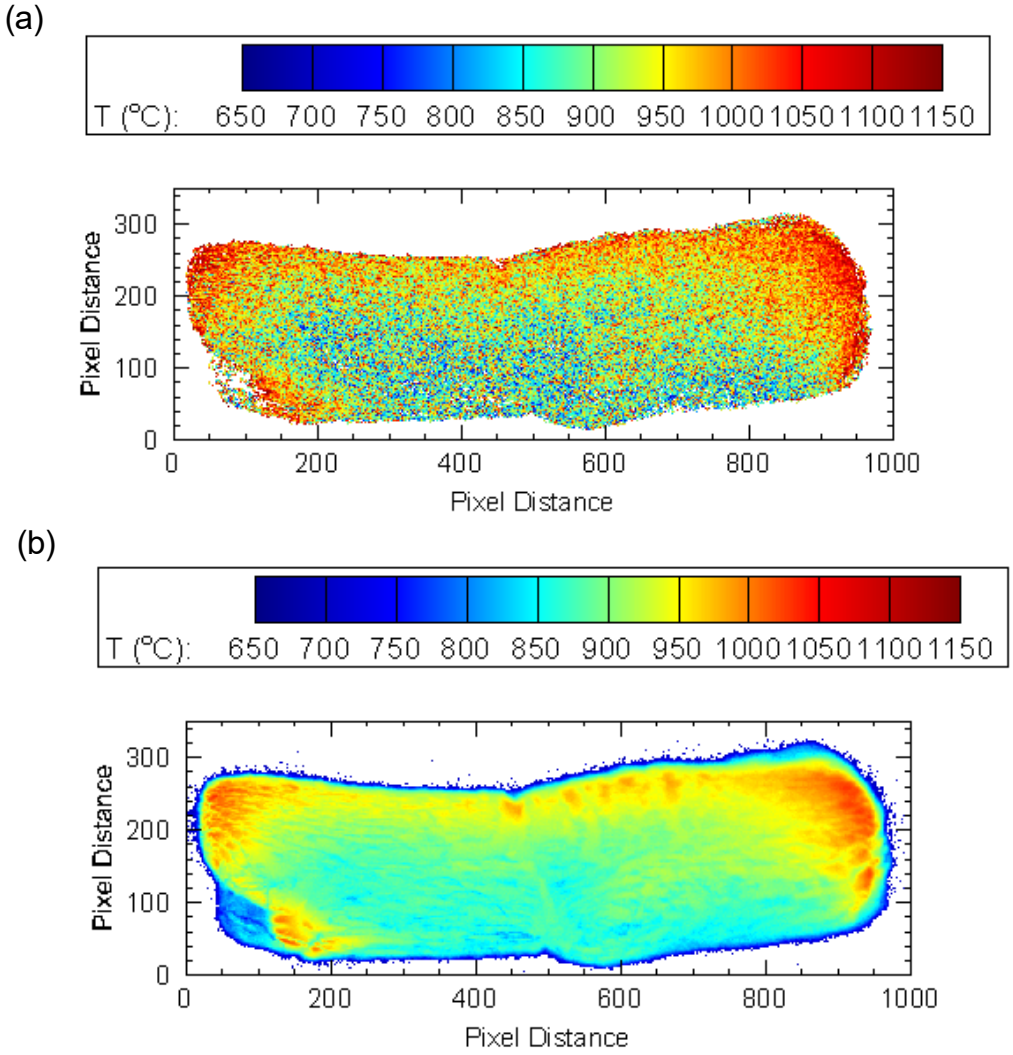

Figure B-8 (a) Non-smoothed ratio pyrometry results for red/green pyrometry; and (b) intensity pyrometry results from a color image in Figure B-7.

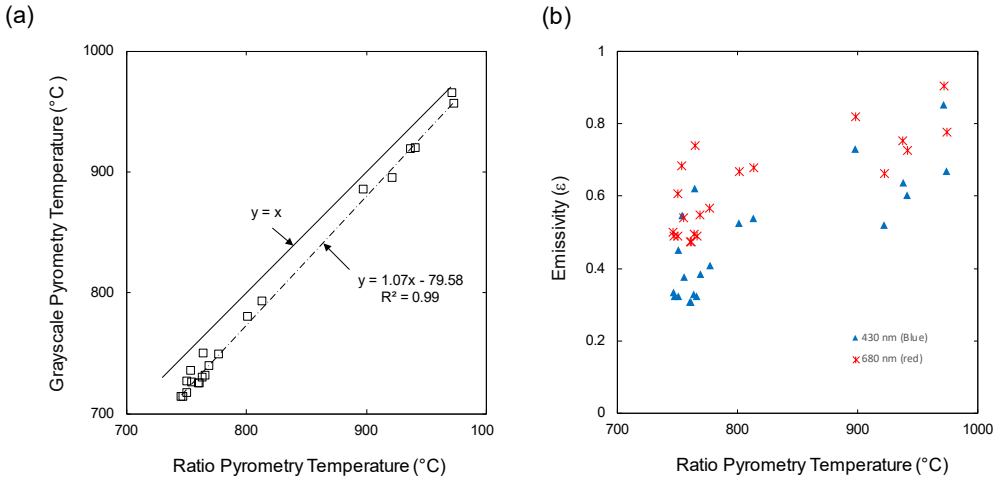

Figure B-9 (a) Grayscale pyrometry temperature and (b) visible emissivity plotted with respect to ratio pyrometry temperature for smoldering embers in Fig. B-3, Fig. B-5, and B-7.

B.3 Test 3 (smoldering ember before and after fan activation)

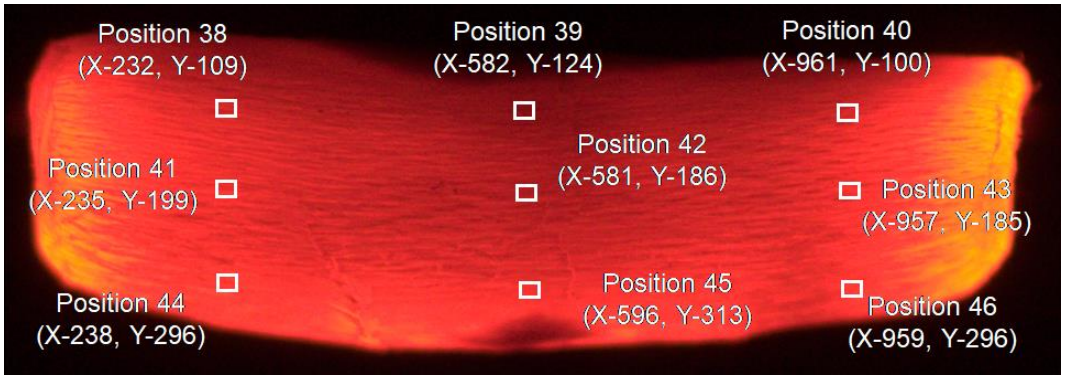

Figure B-10 Indication of isothermal regions of an ember from a color image (1200 × 420 pixels) of a glowing ember. The exposure was 1/6 s at f/2.5. Captured before the fan was activated.

(a)

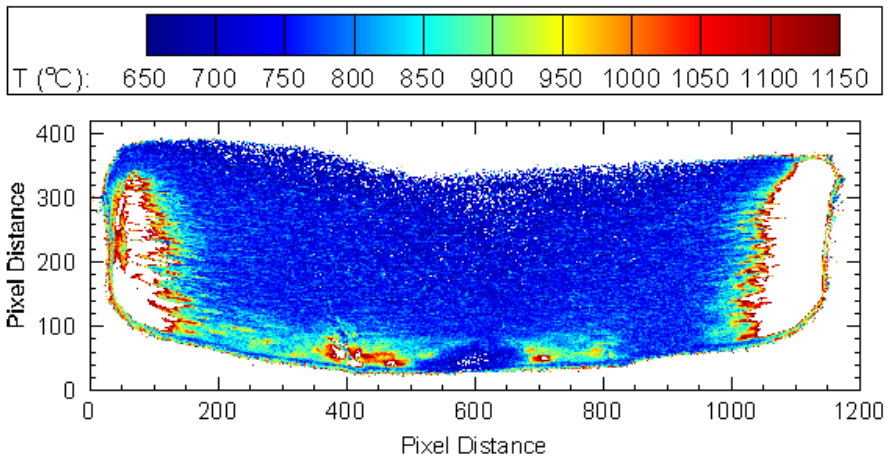

(b)

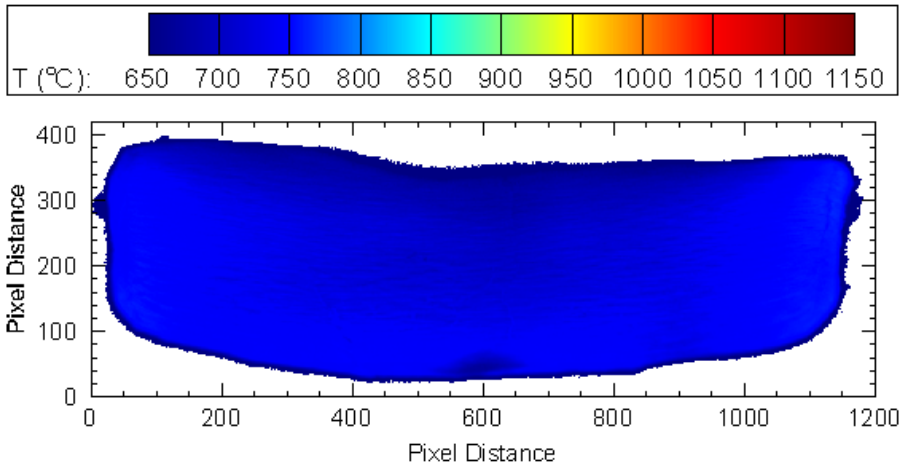

Figure B-11 (a) Non-smoothed ratio pyrometry results for red/green pyrometry; and (b) intensity pyrometry results from a color image in Figure B-10.

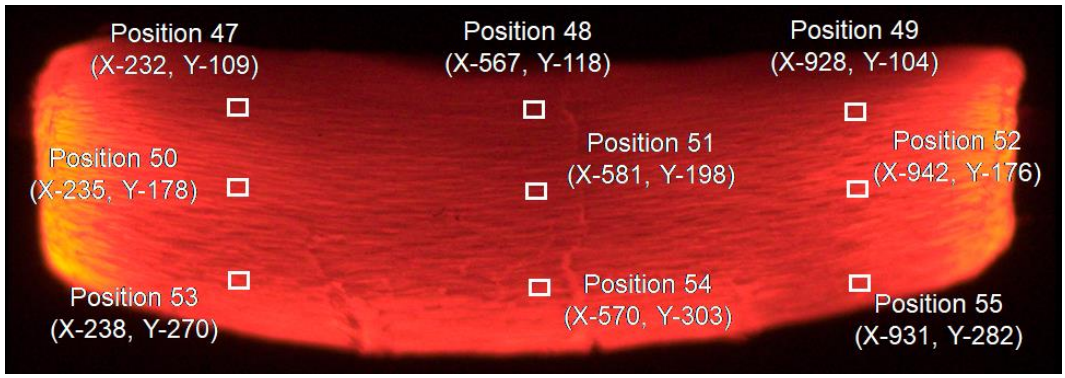

Figure B-12 Indication of isothermal regions of an ember from a color image (1164 × 408 pixels) of a glowing ember. The exposure was 1/10 s at f/2.5. Captured before the fan was activated.

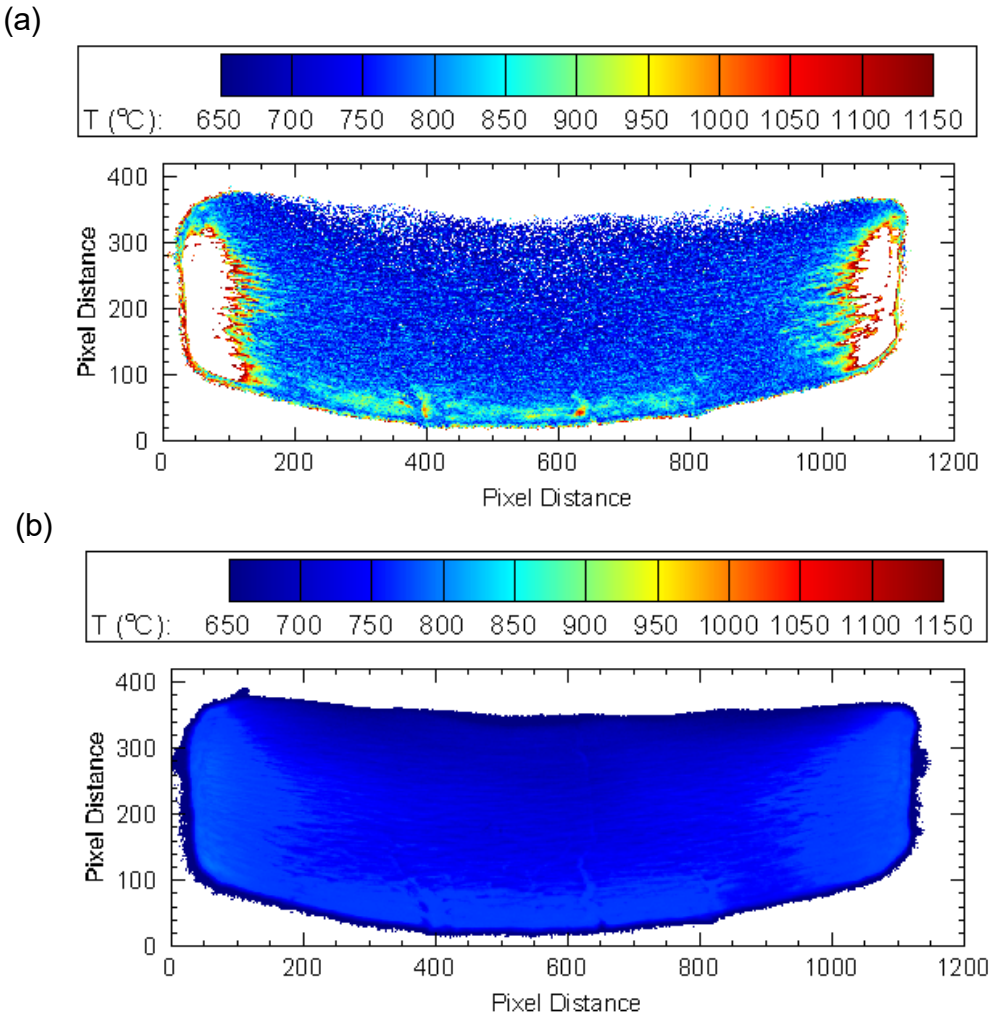

Figure B-13(a) Non-smoothed ratio pyrometry results for red/green pyrometry; and (b) intensity pyrometry results from a color image in Figure B-12.

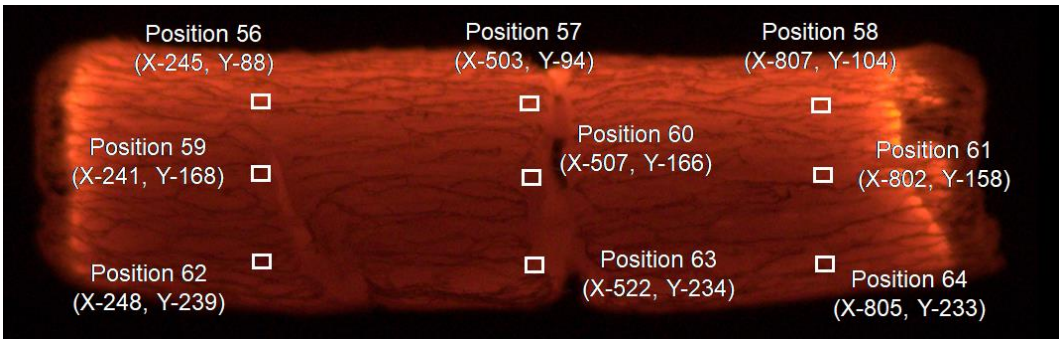

Figure B-14 Indication of isothermal regions of an ember from a color image (1044 × 336 pixels) of a glowing ember. The exposure was 1/640 s at f/2.5. Captured after the fan was activated.

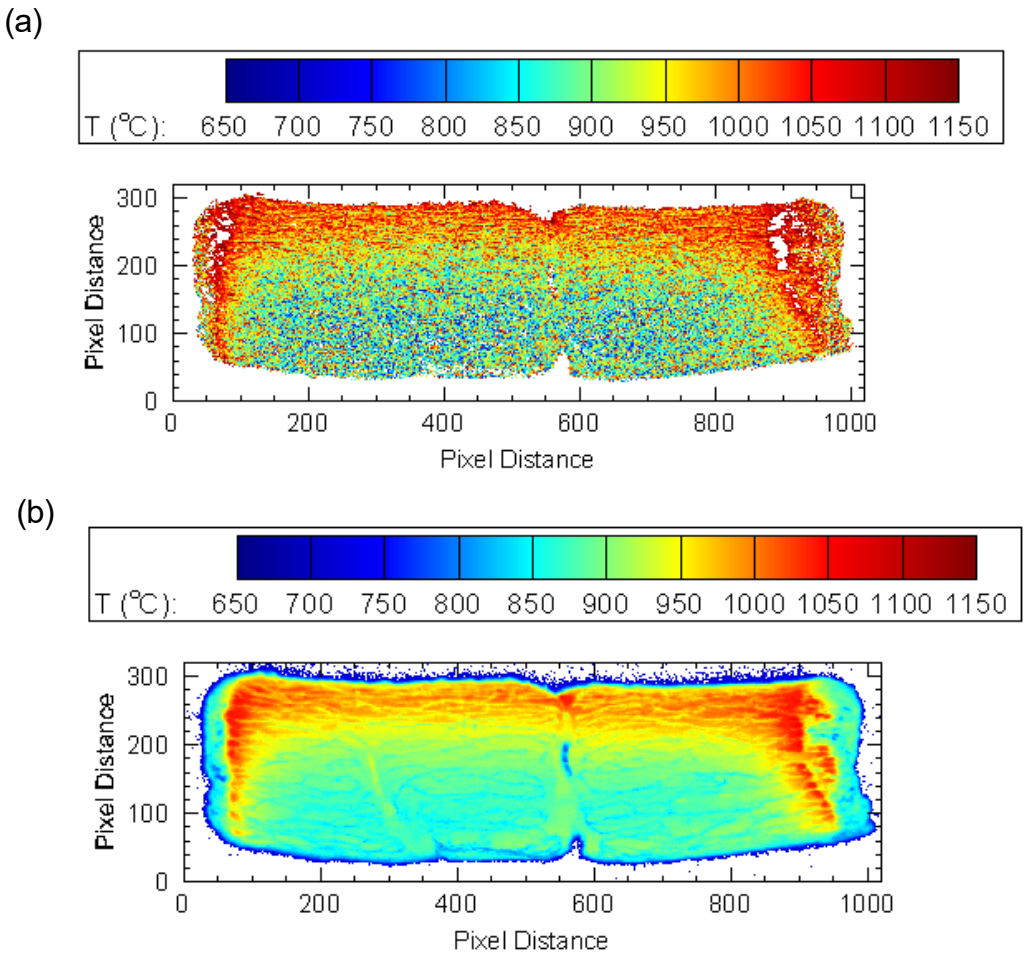

Figure B-15 (a) Non-smoothed ratio pyrometry results for red/green pyrometry; and (b) intensity pyrometry results from a color image in Figure C-14.

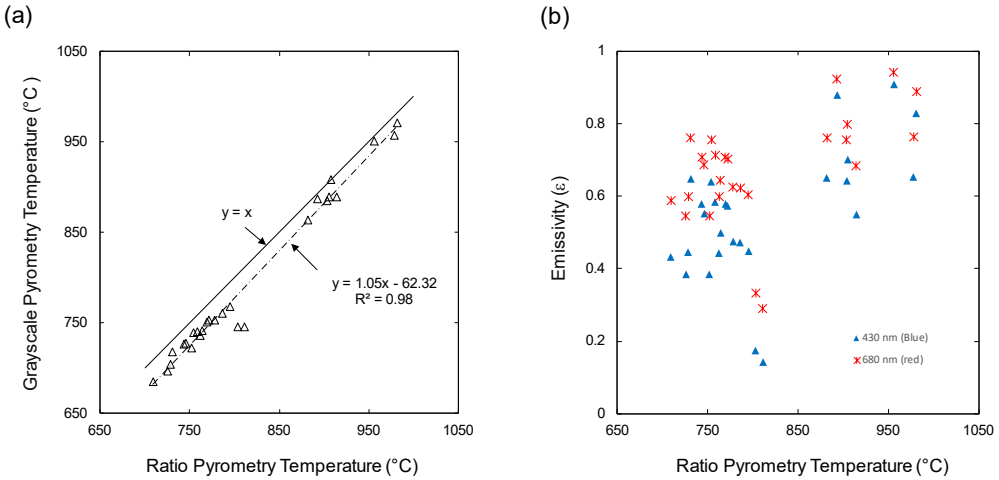

Figure B-16 (a) Grayscale pyrometry temperature and (b) visible emissivity plotted with respect to ratio pyrometry temperature for smoldering embers in Fig. C-10, Fig. C-12, and C-14.

B.4 Test 4 (smoldering ember with 7 m/s velocity of air supply)

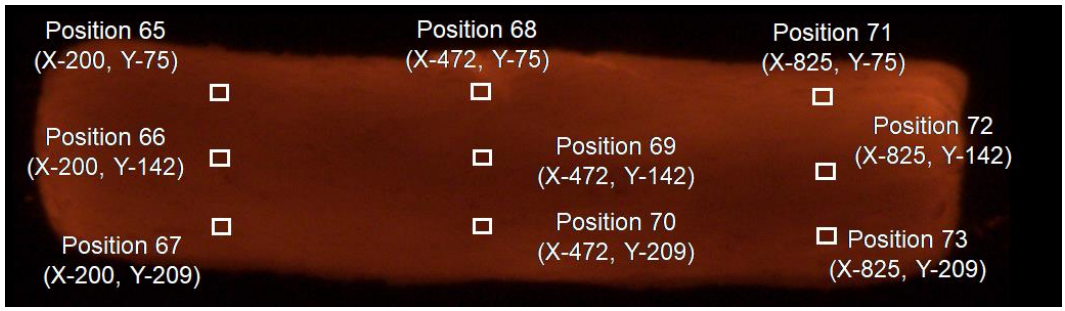

Figure B-17 Indication of isothermal regions of an ember from a color image (1056 × 312 pixels) of a glowing ember at 50 s. The exposure was 1/640 ms at f/10. The velocity of the air supply was 7.0 m/s.

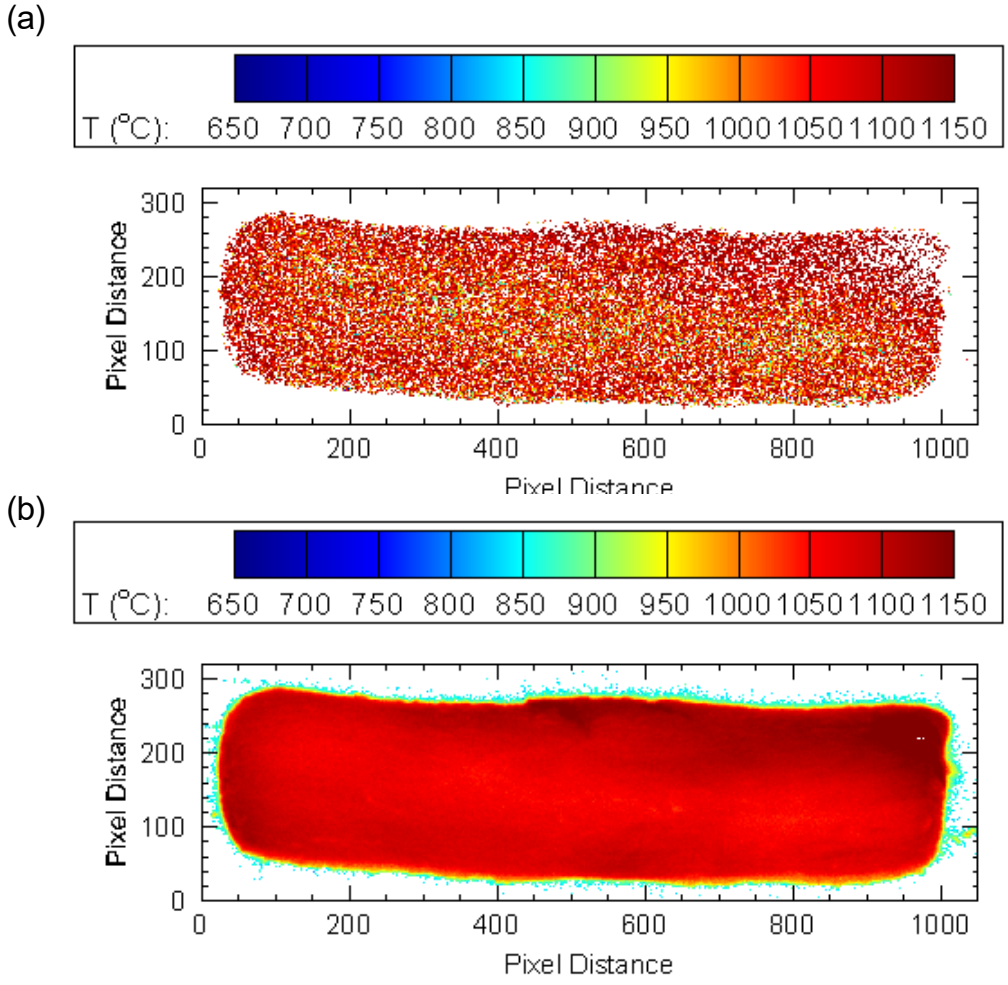

Figure B-18 (a) Non-smoothed ratio pyrometry results for red/green pyrometry; and (b) intensity pyrometry results from a color image in Figure B-17.

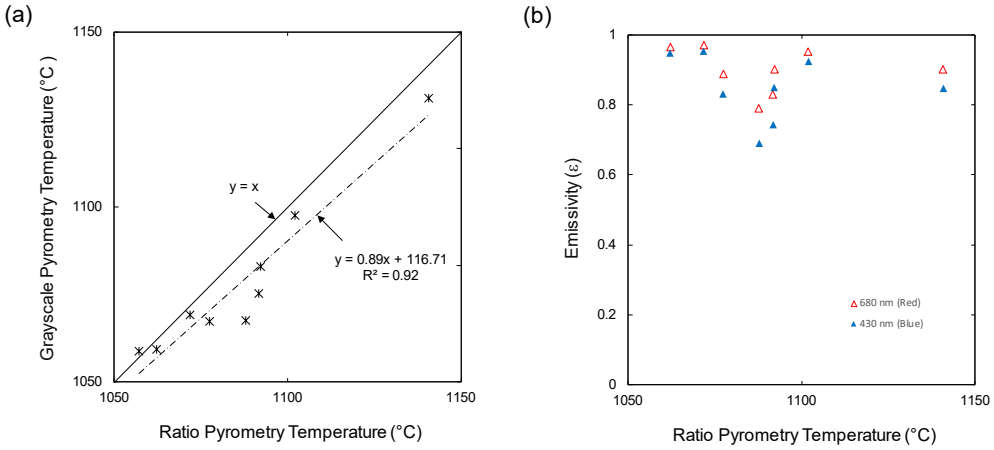

Figure B-19 (a) Grayscale pyrometry temperature and (b) visible emissivity plotted with respect to ratio pyrometry temperature for smoldering embers in Fig. C-17.

Appendix C. Incense Pyrometry With Air Supply

C.1 Test 1 (Air supply velocity : 3.7 m/s))

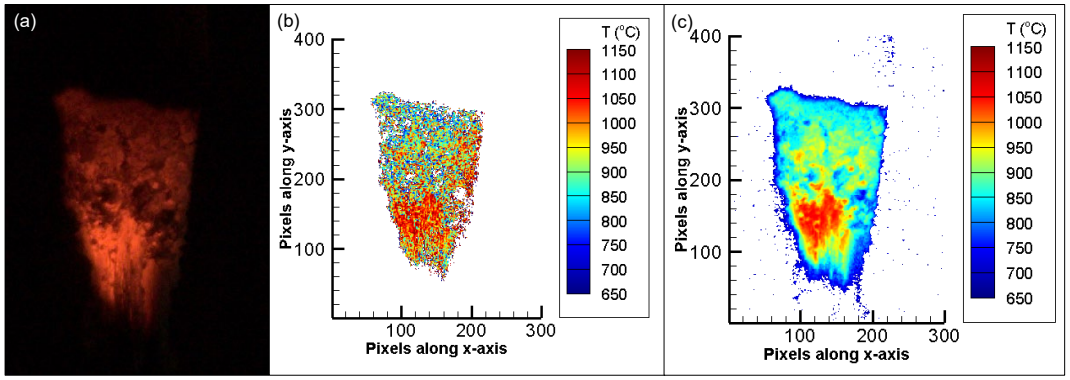

Figure C-1 (a) Color image (400 × 300 pixels) of a smoldering incense, which was exposed to 3.7 m/s air velocity. For this image ISO = 200, f = 2.5, and t = 1.3 ms. Figure (b) is the resulting color contour plot of ratio pyrometry temperatures. Figure (c) is the resulting color contour plot of grayscale pyrometry temperatures.

C.2 Test 2 (Air supply velocity : 7.2 m/s))

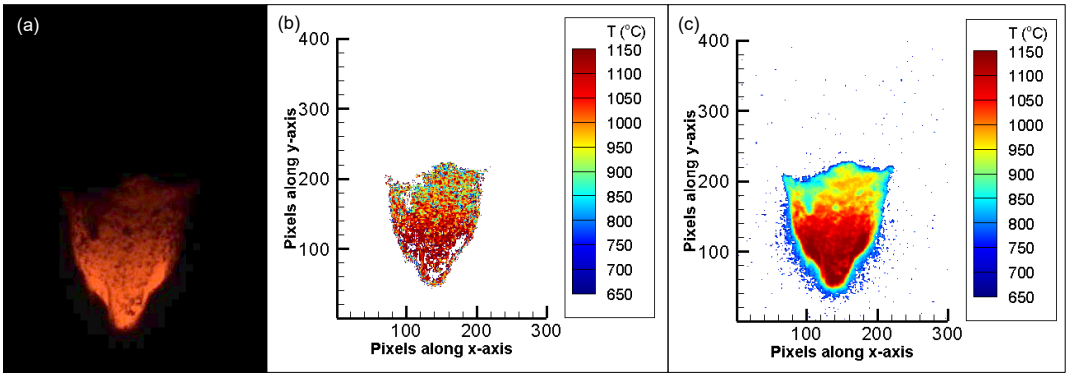

Figure C-2 (a) Color image (400 × 300 pixels) of a smoldering incense, which was exposed to 7.2 m/s air velocity. For this image ISO = 200, f = 4, and t = 1 ms. Figure (b) is the resulting color contour plot of ratio pyrometry temperatures. Figure (c) is the resulting color contour plot of grayscale pyrometry temperatures.

C.3 Test 3 (Air supply velocity : 10 m/s))

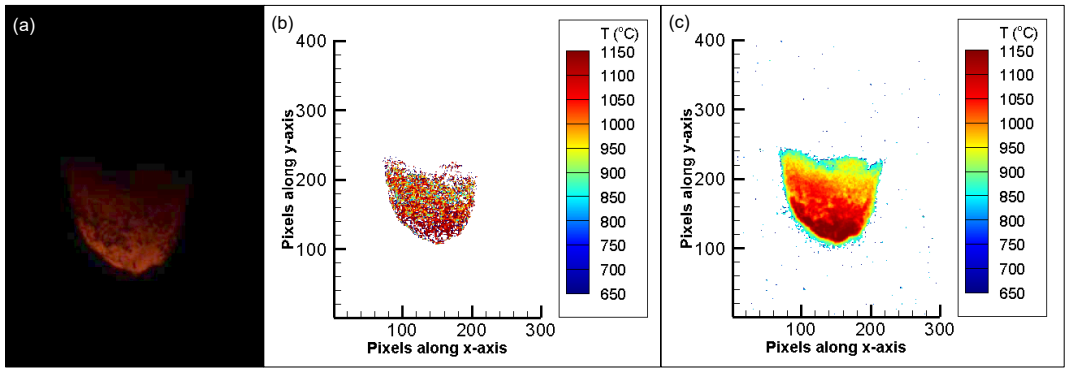

Figure C-3 (a) Color image (400 × 300 pixels) of a smoldering incense, which was exposed to 10 m/s air velocity. For this image ISO = 200, f = 8, and t = 1 ms. Figure (b) is the resulting color contour plot of ratio pyrometry temperatures. Figure (c) is the resulting color contour plot of grayscale pyrometry temperatures.

C.4 Test 4 (Air supply velocity : 13.8 m/s))

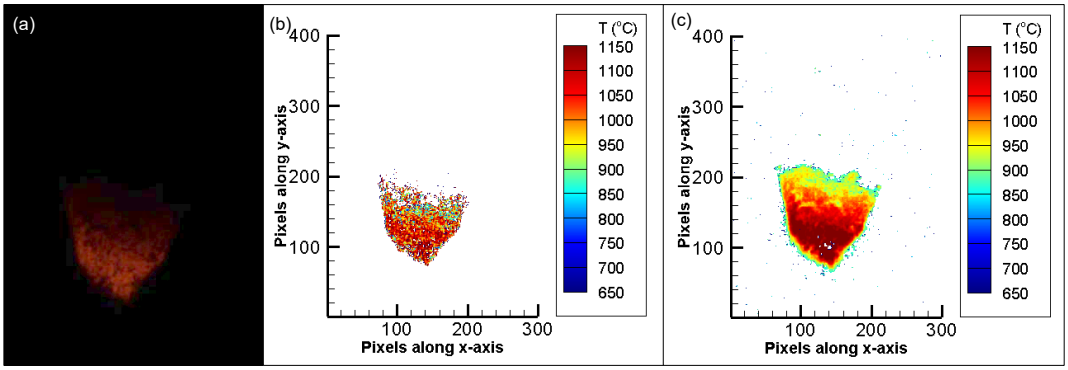

Figure C-4 (a) Color image (400 × 300 pixels) of a smoldering incense, which was exposed to 13.8 m/s air velocity. For this image ISO = 200, f = 9, and t = 2.5 ms. Figure (b) is the resulting color contour plot of ratio pyrometry temperatures. Figure (c) is the resulting color contour plot of grayscale pyrometry temperatures.

C.5 Test 5 (Air supply velocity : 15.8 m/s))

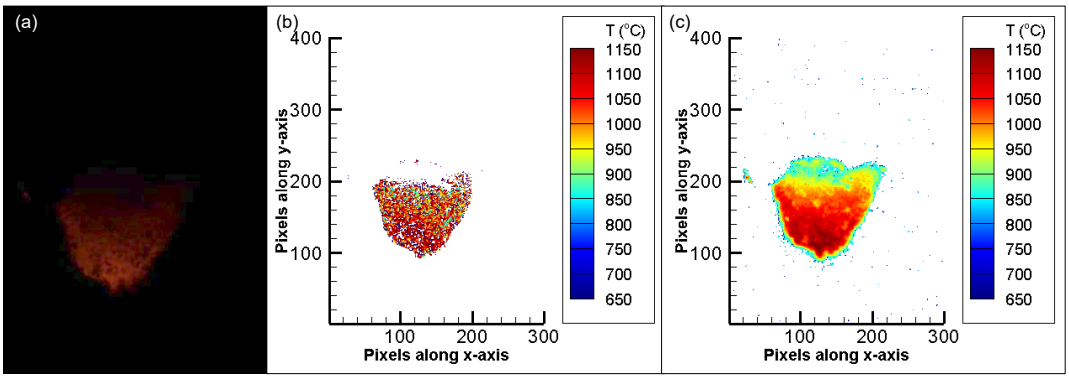

Figure C-5 (a) Color image (400 × 300 pixels) of a smoldering incense, which was exposed to 15.8 m/s air velocity. For this image ISO = 200, f = 9, and t = 1.3 ms. Figure (b) is the resulting color contour plot of ratio pyrometry temperatures. Figure (c) is the resulting color contour plot of grayscale pyrometry temperatures.

C.6 Test 6 (Air supply velocity : 19.2 m/s))

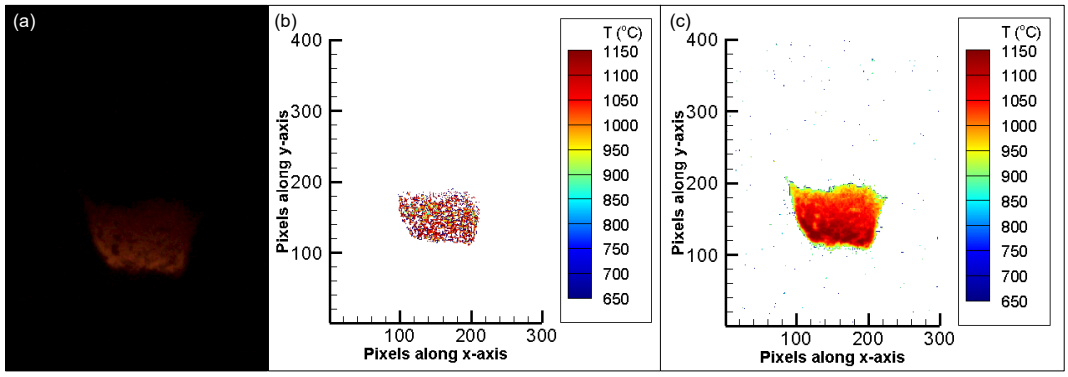

Figure C-6 (a) Color image (400 × 300 pixels) of a smoldering incense, which was exposed to 19.2 m/s air velocity. For this image ISO = 200, f = 9, and t = 0.5 ms. Figure (b) is the resulting color contour plot of ratio pyrometry temperatures. Figure (c) is the resulting color contour plot of grayscale pyrometry temperatures.

C.7 Test 1 (Air supply velocity : 22.5 m/s))

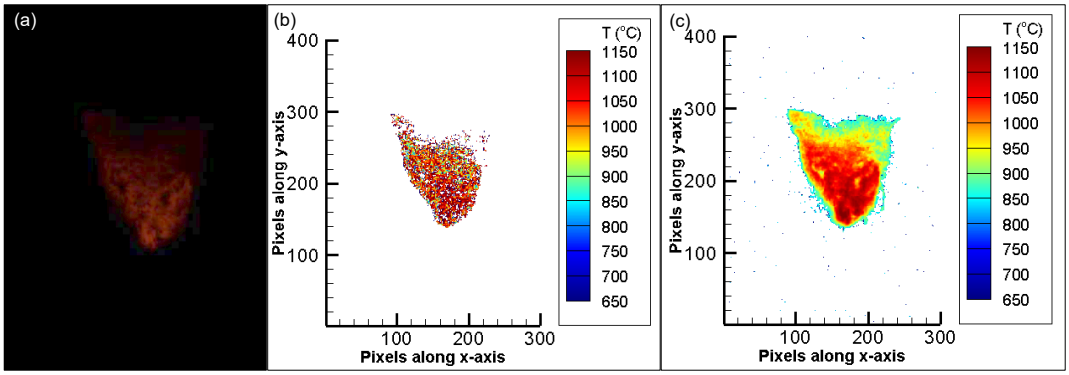

Figure C-7 (a) Color image (400 × 300 pixels) of a smoldering incense, which was exposed to 22.5 m/s air velocity. For this image ISO = 200, f = 9, and t = 1.3 ms. Figure (b) is the resulting color contour plot of ratio pyrometry temperatures. Figure (c) is the resulting color contour plot of grayscale pyrometry temperatures.

List of Contribution During Ph. D

Peer-Reviewed Articles

- **D.K. Kim**, P.B. Sunderland*, "Viability of Various Ignition Sources to Ignite A2L Refrigerant", Science and Technology for the Built Environment (Preparation).
- **D.K. Kim**, P.B. Sunderland*, "Effects of Velocity on Ember Temperatures", Fire Safety Journal (Preparation).
- **D.K. Kim**, P.B. Sunderland*, "Fire ember pyrometry using a color camera", Fire Safety Journal, Oct. 22, 2018 (Submitted)
- **D.K. Kim**, A.E. Klieger, P.Q. Lomax, C.G. McCoy, J. Reymann, P.B. Sunderland*, An improved test method for refrigerant flammability limits in a 12 L vessel, Sci. Technol. Built Environ., 24 (2018) 861 – 866.

Conference Papers

- **D.K. Kim**, P.B. Sunderland*, "Fire Ember Pyrometry Using a Color Camera", 11th US National Combustion Meeting, CA, March, 27, 2019.
- **D.K. Kim**, P.B. Sunderland*, "Viability of Various Ignition sources to ignite A2L Refrigerant Leaks", Purdue Conferences, July. 9, 2018.
- **D.K. Kim**, A.E. Klieger, P.Q. Lomax, C.G. McCoy, J. Reymann, P.B. Sunderland*, "Improving Refrigerant Flammability Limit Test Methods Based on ASTM E681", Purdue Conferences, July. 9, 2018.
- **D.K. Kim**, A.E. Klieger, P.Q. Lomax, C.G. McCoy, J. Reymann, P.B. Sunderland*, "An Improved Test Method for Refrigerant Flammability Limits in a 12 L Vessel", Eastern States Section of The Combustion Institute, Pennsylvania, Mar. 4, 2018.
- **D.K. Kim**, P.B. Sunderland*, "Investigation of Energy Produced by Potential Ignition Sources in Residential Application", AHRI Final Reports No. 8017, 75 pages, Nov. 3, 2017.
- **D. Kim**, P. Sunderland, "Recommended Revision to ASTM E681 and ASHRAE 34", March 29, 2017
    - Revisions are recommended below to these documents:
    - ANSI/ASHRAE Standard 34-2013, Designation and Safety Classification of Refrigerants.
    - ASTM E681 − 09, Standard Test Method for Concentration Limits of Flammability of Chemicals (Vapors and Gases).

Oral Presentation

- Presentation for the 11th US National Combustion Meeting, "Fire Ember Pyrometry Using a Color Camera", Caltech, Pasadena, CA, Mar. 27. 2019
- Presentation for the National Institute of Standards and Technology (NIST) Wildland-Urban Interface (WUI) Fire day, "Fire Ember Pyrometry", University of Maryland, College Park, MD, Jan. 11, 2019.

- Presentation for the National Institute of Standards and Technology (NIST) Disaster Resilience Symposium, “Measurement Fire Ember Temperature and Emissivity with a Color Camera”, Gaithersburg, MD, Aug. 14, 2018.
- Presentation for Technical Meeting of the Eastern States Section of the Combustion Institute, “An Improved Test Method for Refrigerant Flammability Limits in a 12 L Vessel”, Penn state, State College, PA, Mar. 6. 2018

Bibliography

[1] Grishin. A.M., A.I. Filkov, E.L. Loboda, V.V. Reyno, A.V. Kozlov, V.T. Kuznetsov, D.P. Kasymov, S.M. Andreyuk, A.I. Ivanov and N.D. Stolyarchuck. 2014. A field experiment on grass fire effects on wooden consturctions and peat layer ignition. Int. J. Wildland Fire 23:445 – 449.

[2] Cohen. J.D. 2000. Preventing disaster: home ignitability in the wildland urban interface. J. For. 98:15 – 21.

[3] Sharifian. A., and J. Hashempour. 2016. A novel ember shower simulator for assessing performance of low porosity screens at high wind speeds against firebrand attacks. J. Fire Sci. 34(4):335 – 355.

[4] Mell. W.E., S.L. Manzello., A. Maranghides, D. Butry., and R.G. Rehm. 2010. The wildland-urban interface fire problem – current approaches and research needs. Int. J. Wildland Fire 19(2):238 – 251.

[5] Caton. S.E., R.S.P. Hakes., M.J. Gollner, D.J. Gorham, and A. Fernande. 2016. Review of Pathways for Building Fire Spread in the Wildland Urban Interface Part 1: Exposure Conditions. Fire Technol. 53(2):429 – 473.

[6] Pellegrino. J.L., N.P. Bryner., and E.L. Johnsson. 2013. Wildland-Urban Interface Fire Research Needs: Workshop Summary Report. NIST Special Publication 1150.

[7] Cheng. H., L. Ke-zhen., S. Li-fu, H. Xia-fang, and Z. Si-yu. 2018. The Diagnostic Methods for Resurgences of Smoldering Fire in the Forests by Infrared Thermal Imaging. Spectrosc. Spectr. Anal. 38(1):326 – 332.

[8] Rein. G. 2013. Smouldering Fires and Natural Fuels. Chapter 2 in: Fire Phenomena in the Earth System – An Interdisciplinary Approach to Fire Science, pp. 15 - 34. Wiley and Sons.

[9] Ganteaume. A., M. Guijarro., M. Jappiot., C. Hernando., C. Lampin-Maillet., Pedro Perez-Gorostiaga., and J. A. Vega. 2011. Laboratory characterization of firebrands involved in spot fires. Ann. For. Sci. 68:531 – 541.

[10] Suzuki. S., E. Johnsson., A. Maranghides., and S.L. Manzello. 2016. Ignition of Wood Fencing Assemblies Exposed to Continuous Wind-Driven Firebrand Showers. Fire Technol. 52(4):1051 – 1067.

[11] Manzello. S.L., J.R. Shields., T.G. Cleary., A. Maranghides., W.E. Mell., J.C. Yang., Y. Hayashi, D. Nii., and T. Kurita. 2008. On the development and characterization of a firebrand generator. Fire Saf. J. 43(4):258 – 268.

[12] Zhou. K., S. Suzuki., and S.L. Manzello. Experimental Study of Firebrand Transport. Fire Technol. 51(4):785 – 799.

[13] Suzuki. S., A. Brown., S.L. Manzello., and J. Suzuki. 2014. Firebrands generated from a full-scale structure burning under well-controlled laboratory conditions. Fire Saf. J. 63:43 – 51.

[14] Tohidi. A., N. Kaye., and W. Bridges. 2015. Statistical description of firebrand size and shape distribution from coniferous trees use in Metropolis Monte Carlo simulations of firebrand flight distance. Fire Saf. J. 77:21 – 35.

[15] Tarifa. C.S., P. P Del Notario., and F.G. Moreno. 1965. On the Flight Paths and Lifetimes of Burning Particles of Wood. Symposium (International) on Combustion 10(1):1021 – 1037.

[16] Oliveira. L.A., A.G. Lopes., B.R. Baliga., M. Almeida., and D.X. Viegas. 2014. Numerical prediction of size, mass, temperature and trajectory of cylindrical wind-driven firebrands. Int. J. Wildland Fire 23(5):698 – 708.
[17] Anthenien. R.A., S.D. Tse., and A.C. Fernandez-Pello. 2006. On the trajectories of embers initially elevated or lofted by small scale ground fire plumes in high winds. Fire Saf. J. 41(2006):349 – 363.
[18] Tse. S.D., and A.C. Fernandez-Pello. 1998. On the Flight Paths of Metal Particles and Embers Generated by Power Lines in High Winds–a Potential Source of Wildland Fires. Fire Saf. J. 30(4):333 – 356.
[19] A. Ganteaume, C. Lampin-Maillet, M. Guijarro, C. Hernando, M. Jappiot, T. Fonturbel, P. Perez-Gorostiaga, and J.A. Vega. 2009. Spot fires: fuel bed flammability and capability of firebrands to ignite fuel beds. Int. J. Wildland Fire 18:951 – 969.
[20] Kuznetsov. V T., A I . Filkov, Yu N. Isaev., V O Guk. 2014. Ignition of wood subjected to the decreasing radiant energy flux. IOP Conference Series: Materials Science and Engineering 81, p. 012071.
[21] Manzello. S.L., S. Park., and T.G. Cleary. 2009. Investigation on the ability of glowing firebrands deposited within crevice to ignite common building materials. Fire Saf. J. 44 (6):894 – 900.
[22] Manzello. S.L., T.G. Cleary., J.R. Shields., and J.C. Yang. 2006. Ignition of mulch and grasses by firebrands in wildland-urban interface fires. Int. J. Wildland Fire 15(3):427 – 431.
[23] Suuberg, E.M., I. Milosavljevic., and W.D. Lilly. 1994. Behavior of charring materials in simulated fire environments. Technical Report NIST GCR 94-645, NIST Internal Report.
[24] Manzello. S.L., S. Park., S. Suzuki., J.R. Shields., and Y. Hayashi. 2011. Experimental investigation of structure vulnerabilities to firebrand showers. Fire Saf. J. 46(8):568 – 578.
[25] Urbas. J., W.J. Parker., and G.E. Luebbers. 2004. Surface temperature measurements on burning materials using an infrared pyrometer: accounting for emissivity and reflection of external radiation. Fire Mater. 28(1):33 – 53.
[26] Fateev. V., M. Agafontsev., S. Volkov., and A. Filkov. 2017. Determination of smoldering time and thermal characteristics of firebrands under laboratory conditions. Fire Saf. J. 91:791 – 799.
[27] Hakes. R.S.P., H. Salehizadeh, M.J. Weston-Dawkes, and M.J. Gollner. 2019. Thermal characterization of firebrand piles. Fire Saf. J. 104:34 – 42.
[28] Lu. H., L.Ip., A. Mackrory., L. Werrett., J. Scott., D. Tree., and L. Baxter. 2009. Particle Surface Temperature Measurements with Multicolor Band Pyrometry. AICHE J. 55(1):243 – 255.
[29] Urban. J.L., A.C. Fernandez-Pello., M. Vicariotto., and D. Dunn-Rankin. 2019. Temperature Measurement of Glowing Embers with Color Pyrometry. Fire Technol. 1 – 14.
[30] Araujo. A. 2017. Multi-spectral pyrometry – a review. 2017. Meas. Sci. Technol. 28(8), 15pp.

[31] Guo. H., J.A. Castillo., and P.B. Sunderland. 2013. Digital camera measurements of soot temperature and soot volume fraction in axisymmetric flames. Appl. Optics 52(33):8040 – 8047.
[32] Urban. D.L., Z.-G. Yuan, P.B. Sunderland., G.T. Linteris., J.E. Voss., K.-C. Lin., Z. Dai., K. Sun., and G.M. Faeth. 2014. Structure and Soot Properties of Nonbuoyant Ethylene/Air Laminar Jet Diffusion Flames. AIAA J. 36(8):1346 – 1360.
[33] Diez. F.J., C. Aalburg, P.B. Sunderland., D.L. Urban., Z.-G. Yuan., and G.M. Faeth. 2014. Soot properties of laminar jet diffusion flames in microgravity. Combust. Flame 156(8):1514 – 1524.
[34] Jakob. M., P. Lehnen., P. Adomeit., and S. Pischinger. 2014. Development and application of a stereoscopic 3-color high-speed ratio-pyrometry. Combust. Flame 161(11):2825 – 2841.
[35] Giassi. D., B. Lui., and M.B. Long. 2015. Use of high dynamic range imaging for quantitative combustion diagnositcs. Appl. Optics 54(14):4580 – 4588.
[36] Macek. A., and C. Bulik. 1984. Direct Measurement of Char-Particle Temperatures In Fluidized-Bed Combustors. Symposium (International) on Combustion 20 (1):1223 – 1230.
[37] Toth. P., T. Draper., and A.B. Palotas., T.A Ring., and E.G. Eddings. 2015. Three-dimensional combined pyrometric sizing and velocimetry of combusting coal particles. 2: Pyrometry. Appl. Optics 54(15):4916 – 4926.
[38] Khatami. R., and Y.Y. Levendis. 2011. On the deduction of single coal particle combustion temperature from three- color optical pyrometry. Fire Technol. 158 (9):1822 – 1836.
[39] Salinero. J., A. Gomez-Barea., D. Fuentes-Cano., and B. Leckner. 2017. The effect of using thermocouple on the char particle combustion in a fluidized bed reactor. Fuel 207(1):615 – 624.
[40] Salinero. J., A. Gomez-Barea., D. Fuentes-Cano., and B. Leckner. 2018. Measurement and theoretical prediction of char temperature oscillation during fluidized bed combustion. Combust. Flame 192:190 – 204.
[41] Zander. F. 2016. Surface Temperature Measurements in Hypersonic Testing Using Digital Single-Lens Reflex Cameras. J. Thermophys. Heat Transf. 30(4):919 – 925.
[42] Deep. S., Y. Krishna., and G. Jagadeesh. 2017. Temperature characterization of a radiating gas layer using digital-single-lens-reflex-camera-based two-color ratio pyrometry. Appl. Optics 56(30):8492 – 8500.
[43] Raj. V.C., and S.V. Prabhu. 2013. Measurement of surface temperature and emissivity of different materials by two-colour pyrometry, Rev. Sci. Instrum. 84.
[44] Liu. Y., J.L. Urban., C. Xu., and C. Fernandez-Pello. 2019. Temperature and Motion Tracking of Metal Spark Sprays. Fire Technol. 1 – 27.
[45] Kuhn. P.B., B. Ma., B.C. Connelly., M.D. Smooke., and M.B. Long. 2011. Soot and thin-filament pyrometry using a color digital camera. Proc. Combustion. Inst. 33(1):743 – 750.
[46] Mauer. C. 2009. Measurement of the spectral response of digital cameras with a set of interference filters. Thesis, Univ. of Applied Sciences Cologne, Dept. of Media- and Phototechnology.

[47] Ombrello. T., D.L. Blunck., and M. Resor. 2016. Quantified infrared imaging of ignition and combustion in a supersonic. Exp. Fluids 57:140.
[48] Coffin. D. 2018. Decoding raw digital photos in Linux, https://www.cybercom.net/~dcoffin/dcraw/.
[49] D. De Sousa. Meneses, P. Melin., L. del Campo., L. Cosson., and P. Echegut. 2015. Apparatus for measuring the emittance of materials from far infrared to visible wavelengths in extreme conditions of temperature. Infrared Phys. Technol. 69:96 – 101.
[50] www.1stvision.com/machine-vision-solutions/2018/06/ccd-vs-cmos-industrial-cameras-excel-in-allied-vision-industrial-camera.html
[51] Xu. Y., Li. S., Yuan. Y., and Yao. Q. 2017. Measurement on the Surface Temperature of Dispersed Chars in a Flat-Flame Burner Using Modified RGB Pyrometry. Energy Fuels 31(3):2228 – 2235.
[52] Jacob. R.J. 2018. Enhancing the Combustion Characteristics of Energetic Nanocomposites Through Controlled Microstructures, Ph.D. Dissertation, Univ. of Maryland, Dept. of Mechanical Engineering.
[53] ASTM. 2016. ASTM D4442-16, Standard Test Methods for Direct Moisture Content Measurement of Wood and Wood-Based Materials. West Conshohocken, PA: American Society of Testing and Materials.
[54] Gabitto. J., and C. Tsouris. 2018. Drag coefficient and settling velocity for particles of cylindrical shape. Powder Technol. 183:314 – 322.
[55] Tu. W., J. Lin, and Y. Wu. 2011. An Analysis of Extinction Coefficients of Particles and Water Moisture in the Stack after Flue Gas Desulfurization at a Coal-Fired Power Plant. J. Air Waste Manage. Assoc. 61:815 – 825.
[56] Misra. M.K., K.W. Ragland, and A.J. Baker. 1993. Wood Ash Composition as a Function of Furnace Temperature, Biomass Bioenerg. 4:103 – 116.
[57] http://www.bu.edu/gk12/kai/Lesson%204/E_Back.pdf
[58] http://web.mit.edu/8.01t/www/materials/modules/chapter24.pdf
[59] http://hyperphysics.phy-astr.gsu.edu/hbase/mi2.html#irod
[60] https://en.wikipedia.org/wiki/Optical_spectrometer
[61] Zhang. T., Q. Guo., X. Song., Z. Zhou., and G. Yu. 2013. The chemiluminescence and structure properties of normal/inverse diffusion flames. J. Spectrosc. P. 304717.
[62] Hu. C., Y. Gong., Q. Guo., L. He., and G. Yu. 2018. Investigations of CH* chemiluminescence and blackbody radiation in opposed impinging coal- water slurry flames based on an entrained-flow gasifier. Fuel 211:688 – 696.
[63] Yan. W., Y. Ya., F. Du., H. Shao., and P. Zhao. 2017. Spectrometer-Based Line-of-Sight Temperature Measurements during Alkali-Pulverized Coal Combustion in a Power Station Boiler. Energies. 10(9):1375.
[64] Trichard. F., S. Moncayo., D. Devismes., F. Pelascini., J. Maurelli., A. Feugier., C. Sasseville., F. Surma., and V. Motto-Ros. 2017. Evaluation of a compact VUV spectrometer for elemental imaging by laser-induced breakdown spectroscopy: application to mine core characterization, J. Anal. At. Spectrom. 32:1527 – 1534.
[65] https://oceanoptics.com/glossary/#dark-spectrum
[66] Schult. D.A., B.J. Matkowsky., V.A. Volpert, and A.C. Fernandez-Pello. 1996. Combust. Flame 104:1 – 26.

[67] Torero. J.L., A.C. Fernandez-Pello., and M. Kitano. 1993. Opposed Forced Flow Smoldering of Polyurethane foam. Combust. Sci. Technol. 91(1):95 – 117.
[68] Torero. J.L., A.C. Fernandez-Pello., and M. Kitano. 1994. Fire Safety Science-Proceedings of the fourth international symposium 4: 409 – 420.
[69] Ohlemiller. T.J., and F.E. Rogers. 1978. A survey of several factors influencing smoldering combustion in flexible and rigid polymer foams. J. Fire and Flammability 9:489 – 509.
[70] Rein. G. 2016. Smoldering combustion, Chapter 19 in: SFPE Handbook of Fire Protection Engineering, 5th Edition, pp 581 – 693.
[71] Moussa. N.A., T.Y. Toong., and C.A. Garris. 1977. Mechanism of Smoldering of Cellulosic Materials. Symposium (International) on Combustion 16(1): 1447 – 1457.
[72] Kinbara. T., H. Endo., and S. Sega. 1967. Downward Propagation of Smoldering Combustion Through Solid Materials. Eleventh Symposium on Combustion 11(1):525 – 531.
[73] Yang. T.T., C.C. Chen., J.M. Lin. 2005. Effect of Air Flow on Emission of Smoldering Incense, Rev. Environ. Contam. Toxicol. 74: 456 – 463.
[74] Palmer. K.N. 1957. Smouldering combustion in dusts and fibrous materials. Combust. Flame 1(2):129 – 154.